Measurement of the ^{94}Mo(γ,n) reaction by Coulomb dissociation and related post-processing nucleosynthesis simulations for the p-process

Dissertation

von

Kathrin Göbel

aus Hanau

ABSTRACT

The elements in the universe are mainly produced by charged-particle fusion reactions and neutron-capture reactions. About 35 proton-rich isotopes, the p-nuclei, cannot be produced via neutron-induced reactions. To date, nucleosynthesis simulations of possible production sites fail to reproduce the p-nuclei abundances observed in the solar system. In particular, the origin of the light p-nuclei ^{92}Mo, ^{94}Mo, ^{96}Ru and ^{98}Ru is little understood. The nucleosynthesis simulations rely on assumptions about the seed abundance distributions, the nuclear reaction network and the astrophysical environment. This work addressed the nuclear data input.

The key reaction ^{94}Mo(γ,n) for the production ratio of the p-nuclei ^{92}Mo and ^{94}Mo was investigated via Coulomb dissociation at the LAND/R^{3}B setup at GSI Helmholtzzentrum für Schwerionenforschung in Darmstadt, Germany. A beam of ^{94}Mo with an energy of 500 AMeV was directed onto a lead target. The neutron-dissociation reactions following the Coulomb excitation by virtual photons of the electromagnetic field of the target nucleus were investigated. All particles in the incoming and outgoing channels of the reaction were identified and their kinematics were determined in a complex analysis. The systematic uncertainties were analyzed by calculating the cross sections for all possible combinations of the data selection criteria. The integral Coulomb dissociation cross section of the reaction ^{94}Mo(γ,n) was determined to be

$$\sigma_{\text{CD}} = (571 \pm 14_{\text{stat}} \pm 46_{\text{syst}}) \text{ mb}.$$

The result was compared to the data obtained in a real photon experiment carried out at the Saclay linear accelerator. The ratio of the integral cross sections was found to be 0.63 ± 0.07, which is lower than the expected value of about 0.8.

The nucleosynthesis of the light p-nuclei ^{92}Mo, ^{94}Mo, ^{96}Ru and ^{98}Ru was investigated in post-processing nucleosynthesis simulations within the NuGrid research platform. The impact of rate uncertainties of the most important production and destruction reactions was studied for a Supernova type II model. It could be shown that the light p-nuclei are mainly produced via neutron-dissociation reactions on heavier nuclei in the isotopic chains, and that the final abundances of these p-nuclei are determined by their main destruction reactions. The nucleosynthesis of ^{92}Mo and ^{94}Mo was also studied in different environments of a Supernova type Ia model. It was concluded that the maximum temperature and the duration of the high temperature phase determine the final abundances of ^{92}Mo and ^{94}Mo.

ZUSAMMENFASSUNG

Die Elemente im Universum werden hauptsächlich durch Fusionsreaktionen geladener Atomkerne und durch Neutroneneinfangreaktionen erzeugt. Die Synthese von etwa 35 protonenreichen schweren Kernen zwischen Selen und Quecksilber, den sogenannten p-Kernen, ist bisher weitgehend unverstanden. Speziell der Ursprung der häufigsten p-Kerne ^{92}Mo, ^{94}Mo, ^{96}Ru und ^{98}Ru konnte bisher nicht zufriedenstellend erklärt werden. Simulationen zur Nukleosynthese benötigen verschiedene Eingangsparameter: die Temperatur- und Dichteprofile der stellaren Umgebung, die Anfangshäufigkeit aller Atomkerne und die Raten der Kernreaktionen im Simulationsnetzwerk. Die vorliegende Arbeit befasst sich mit Kernreaktionen, welche die Häufigkeiten der p-Kerne ^{92}Mo, ^{94}Mo, ^{96}Ru und ^{98}Ru bestimmen.

Das Verhältnis der Häufigkeiten von ^{92}Mo und ^{94}Mo wird durch die Reaktion ^{94}Mo(γ,n) bestimmt. Diese Reaktion wurde mit der Coulombaufbruchmethode am GSI Helmholtzzentrum für Schwerionenforschung in Darmstadt, Deutschland, untersucht. Ein ^{94}Mo-Strahl wurde mit einer Energie von 500 AMeV auf ein Blei-Target geschossen. Die Strahlteilchen wurden im elektromagnetischen Feld des Bleikerns angeregt, sodass sie ein Neutron emittierten. Der integrale Coulombaufbruchwirkungsquerschnitt der Reaktion ^{94}Mo(γ,n) ergab sich zu

$$\sigma_{\text{CD}} = (571 \pm 14_{\text{stat}} \pm 46_{\text{syst}}) \text{ mb}.$$

Das Ergebnis wurde mit Daten eines Photoabsorptionsexperiments verglichen, das am Linearbeschleuniger in Saclay durchgeführt wurde. Das Verhältnis der integralen Wirkungsquerschnitte wurde zu 0,63 ± 0,07 bestimmt. Dieser Wert ist kleiner als das erwartete Verhältnis von etwa 0,8.

Die Produktion der leichten p-Kerne ^{92}Mo, ^{94}Mo, ^{96}Ru und ^{98}Ru wurde in Nukleosynthesesimulationen untersucht. Die Auswirkungen von Ratenunsicherheiten der Produktions- und Destruktionsreaktionen wurden für ein Modell einer Supernova Typ II ermittelt. Es konnte gezeigt werden, dass die leichten p-Kerne hauptsächlich durch Neutronen-Dissoziationsreaktionen an schwereren Kernen in der Isotopenkette des entsprechenden Elements produziert werden und dass die Häufigkeiten der leichten p-Kerne durch ihre direkten Destruktionsreaktionen bestimmt werden. Die Synthese der p-Kerne ^{92}Mo und ^{94}Mo wurde ebenfalls in einem Supernova Typ Ia Modell untersucht. Es zeigte sich, dass die Häufigkeiten durch die Maximaltemperatur und die Dauer der Hochtemperaturphase bestimmt werden.

Contents

Contents

1 Introduction

1.1 The nucleosynthesis of the elements

Nuclear astrophysics aims at explaining the origin of the elements in our solar system. Data from solar observations and investigations of the composition of meteorites give the numbers of the atomic species as a function of atomic mass A, the solar abundance distribution (Figure 1.1) [1]. Patterns in the distribution indicate different production sites of the elements depending on their mass. Burbidge, Burbidge, Fowler and Hoyle (B^{2}FH) provided the first complete overview of the synthesis of the elements in stars in 1957 [2]. Tremendous progress in astronomical observation techniques, computational capabilities and nuclear physics experiments, allowing the measurement of more and more nuclear reactions of stable and radioactive nuclei, has allowed detailed insights into the nucleosynthesis of the elements [3]. The following sections summarize our current understanding with a focus on the production of the light "p-nuclei".

1.1.1 From hydrogen to iron

The lightest elements hydrogen, helium and small amounts of lithium and beryllium were synthesized during the Big Bang nucleosynthesis [4, 5]. Lithium, beryllium and boron are also produced later on by spallation reactions of cosmic ray particles on heavier nuclei [6].

The elements up to iron are produced by **charged-particle fusion reactions** during different stellar burning phases. Nuclear reactions generate energy in the stellar interior, which causes radiation pressure against the gravitational contraction of the star. A steady state of nuclear burning is achieved until the nuclear fuel of the current burning phase is consumed. When the radiation pressure ceases, the star contracts and the temperature in the core rises until the next burning stage is ignited and hydrostatic equilibrium is reached again. The higher the atomic number of the nuclei, the higher the Coulomb barrier for charged-particle reactions. Hence, higher core temperatures are needed for each further burning phase.
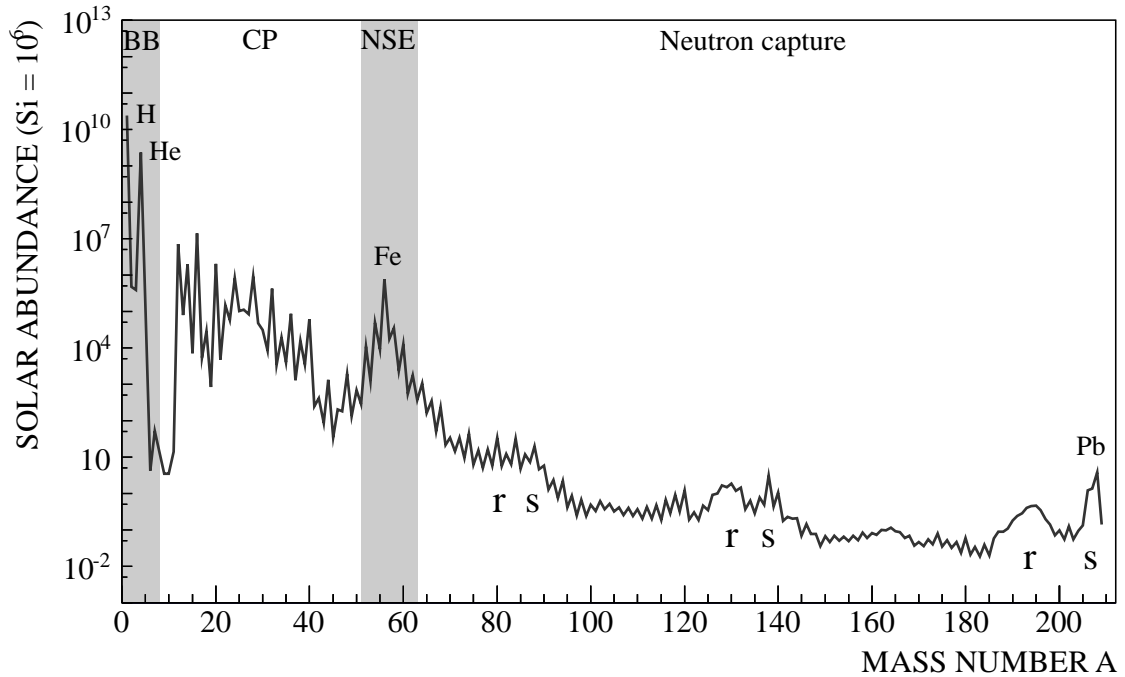
Figure 1.1.: Solar abundances distribution [1]. The sum of the abundances of the stable Si isotopes is normalized to 10^6. The lightest nuclei were produced during the Big Bang nucleo-synthesis ("BB"). Charged-particle reactions ("CP") synthesize heavier nuclei during stellar burning phases. The tightly bound nuclei in the iron region are built in the nuclear statistical equilibrium ("NSE") during the silicon burning phase. The slow ("s") and the rapid ("r") neutron-capture processes produce most of the nuclei between iron and lead and imprint a characteristic pattern on the abundance distribution.

Helium is synthesized in the proton-proton chains and the CNO cycles (if carbon is available as catalyst) during the hydrostatic hydrogen burning phase [7–9]. The resulting He core ignites and produces ^{12}C in the triple-α-process (helium burning) [10–12]. Further burning stages may take place if the mass of the star exceeds certain limits: carbon burning ($M_{star} > 4\ M_\odot$, $M_\odot$ being the solar mass), neon and oxygen burning ($M_{star} > 8\ M_\odot$), which produce the nuclei up to $A = 40$-50. The elements of the iron group are produced during the silicon burning phase. The temperature there is large enough to establish a nuclear statistical equilibrium between the nuclei and free protons and neutron [13]. The binding energy per nucleon and therefore the abundance reaches its maximum at the iron group. An iron core is produced in the star. When the silicon burning phase ceases, the core collapses and the star explodes as a Supernova.

1.1.2   From iron to lead

The nuclei from iron to lead are mainly produced by the rapid (r) and the slow (s) neutron-capture processes. The neutron captures compete with the β-decays of unstable nuclei in the reaction chain.

The **r-process** is supposed to occur in explosive scenarios with neutron densities above 10^{20} cm^{-3} and temperatures above 10^9 K. Neutrons are captured on time scales much shorter than the half-lives of β-unstable nuclei, producing nuclei up to the neutron drip line. An equilibrium between (n,γ) and (γ,n) reactions is established in the isotopic chains. Isotopes with long half-lives, especially along the neutron shell closures, act as waiting points where nuclei are accumulated. These isotopes will β-decay to the next element. When the neutron densities and temperatures rapidly decrease after the explosion, the nuclei decay towards the valley of stability causing the wide peaks in the solar abundance distribution around mass numbers $A = 80$, 130 and 195 (Figure 1.1) [2]. Several scenarios are proposed for the r-process, however, the possible astrophysical environments are still under discussion: core collapse supernova events with jets, neutron star mergers, neutrino-driven winds from proto-neutron stars, shocked surface layers of O-Ne-Mg stellar cores and winds from accretion disks of black holes [14–16].

The **s-process** takes place during stellar He and C burning phases with neutron densities between 10^8 and 10^{10} cm^{-3}. The reaction path closely follows the valley of stability since neutron capture times of typically ten years are much slower than most of the β-decay times of the involved nuclei (Figure 1.2) [17]. Nuclei with a small neutron-capture cross section, e.g. at the closed neutron shells at $N = 50$, 82 and 126, are strongly produced during the s-process. The corresponding stable nuclei with mass numbers $A = 88$, 140 and 208 show a narrow peak in the solar abundance distribution (Figure 1.1). The s-process is composed of the weak, main and strong component [18]. The main differences lie in the neutron-to-seed ratio, the temperature as well as the neutron densities. If the star's metallicity is low, i.e. only few seed nuclei in the iron region are available, each nucleus may capture many neutrons producing heavy nuclei in the lead-bismuth region. If the metallicity is high, each nucleus captures only a few neutrons producing nuclei over a wide mass range closer to the seed.

The **main component of the s-process** takes place in low-mass asymptotic giant branch (AGB) stars and produces the nuclei with mass numbers above $A \approx 90$ [18]. The low-mass AGB star (1 to 5 $M_\odot$) consists of a C/O core surrounded by alternately burning He and H shells, which are separated by a thin He-rich layer. The H envelope is fully convective. He is produced during the H shell burning, increasing the mass of the He intershell. The temperature rises and triggers He burning, which generates a quasi-explosive thermal pulse [17].
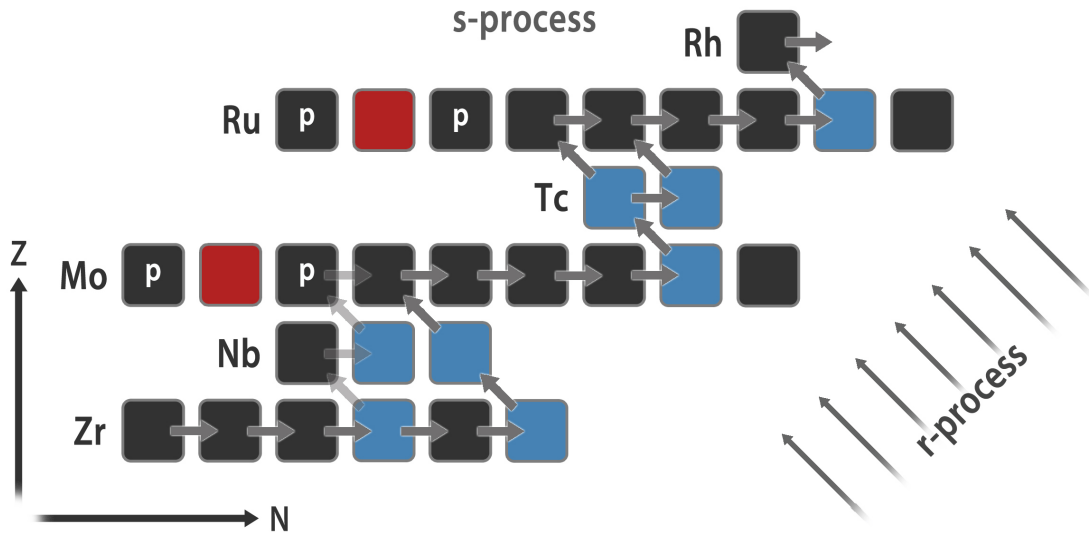
Figure 1.2.: The r- and s-process paths in the Mo-Ru region of the chart of nuclides. The r-process produces neutron-rich isotopes up to the neutron drip line at high neutron densities. The unstable isotopes decay back to the valley of stability. The neutron densities during the s-process are orders of magnitude lower than during the r-process. The neutron capture times are much slower than most of the β-decay times of the nuclei. Hence, the s-process follows the valley of stability. The p-nuclei are bypassed by the s- and r-process flows.

The intershell becomes convective, the envelope expands and the H burning is temporarily extinguished [19]. Carbon and oxygen are produced in the He burning shell until He is consumed to a certain extend. These flashes reoccur about 20 to 30 times depending on the mass of the initial star. When the C/O core reaches a mass of about 0.6 $M_\odot$, the so-called third dredge-up (TDU) after a helium flash mixes H, C, N and elements up to Fe into the He layer [17, 18]. The available protons (H) are captured by ^{12}C producing ^{13}N, which β-decays to ^{13}C. The ^{13}C pocket is formed [20]. The s-process starts when neutrons are released by the ^{13}C(α,n)^{16}O reaction. A second neutron source ^{22}Ne(α,n)^{25}Mg is activated after subsequent thermal pulses when the temperature exceeds $2.5 \cdot 10^8$K [17]. The nuclei produced in the s-process are brought up into the hydrogen envelope and to the surface of the star by convection. The material is released into the interstellar medium during strong winds blowing off the hydrogen envelope of the AGB star.

Low-mass AGB stars with low metallicities produce about 50% of the lead abundance in the **strong s-component**. Neutron-capture reactions starting at the iron seed drive the masses up to the lead-bismuth region because of a high neutron fluence in the ^{13}C pocket [17, 21].

The **weak component of the s-process** takes place in massive stars with $M_{star} > 8\ M_\odot$. The time-integrated neutron flux is lower compared to the main component producing nuclei with mass numbers $A \leqslant 90$. The reaction ^{22}Ne(α,n)^{25}Mg provides neutrons during convective He burning at temperatures of about $3 \cdot 10^8$ K and during convective shell C burning at about 10^9 K. The star explodes as a Supernova type II at the end of its evolution and enriches the interstellar medium with s-process material [17, 22–25].

1.1.3 Supernova explosions - the fate of stars

Supernova type II
Stars with masses of more than 8 $M_\odot$ undergo all stellar burning phases up to silicon burning. The produced iron core is surrounded by oxygen, carbon, helium and hydrogen rich shells and corresponding burning zones. The silicon burning ceases when the fuel is exhausted, which causes the core to contract further. Photodisintegration reactions destroy the heavy nuclei in the core due to the high temperatures. Free electrons are captured by heavy nuclei releasing neutrinos that escape the star. The star then collapses gravitationally without the opposing radiation, gas and degeneracy pressures. The inner core collapses and forms a neutron star. The pressure wave is reflected by the neutron star and passes the remaining still collapsing shells. The material in the shells is compressed and heated allowing nuclear reactions to take place. The stellar envelope is reheated by neutrino interactions and blown up into the interstellar medium. This scenario is classified as a Supernova type II if it shows hydrogen lines in its light spectrum [26].

Supernova type Ia
The standard scenario of a Supernova type Ia assumes the thermonuclear explosion of a white dwarf composed of carbon and oxygen. A possible single-degenerate model describes a binary system of a white dwarf and an evolved star. The C/O white dwarf accumulates hydrogen and helium from the companion star and becomes enriched with s-nuclei (main component) in a sequence of thermal pulse instabilities. The white dwarf explodes when it reaches the Chandrasekhar limit of about 1.4 $M_\odot$. The explosion mechanism is under debate: The burning front of carbon and oxygen travels at subsonic speed in a deflagration event, while the front becomes supersonic in a detonation event. Double-degenerate scenarios describe the merging of two white dwarfs and the following supernova explosion. It is unclear how the proposed models contribute to the observed Supernovae type Ia. However, most of the iron in the solar system is produced in SNIa. The supernovae show no hydrogen lines but strong silicon lines in their light spectra [26, 27].

1.1.4 The p-process

About 35 proton-rich isotopes heavier than iron cannot be produced by neutron-capture reactions since they are bypassed by s- and r-process paths (Figure 1.2) [2]. The origin of the p-nuclei is yet little understood and many possible production sites are under discussion. The production sites differ in three main characteristics: the evolution of the temperature, the particle densities and the seed abundance distributions [28].

The p-nuclei are typically two orders of magnitude less abundant than the r- and s-nuclei of the same element. However, the p-nuclei ^{92,94}Mo and ^{96,98}Ru show considerably higher abundances compared to the other p-nuclei and high isotopic abundances of 14.9%, 9.2%, 5.5% and 1.9%, respectively. So far, nucleosynthesis simulations of stellar production scenarios fail to reproduce the abundances of these light p-nuclei. Much effort was made to investigate the impact of the uncertainties of the seed abundance distributions, the nuclear reaction network and the astrophysical environment on the predicted production of the p-nuclei [28, 29].
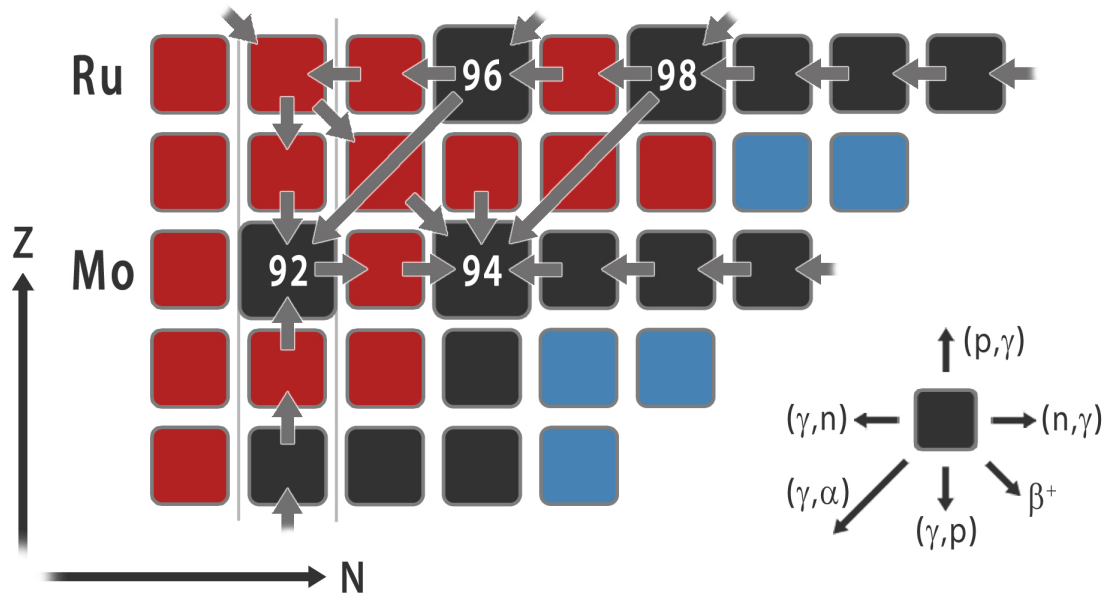

Figure 1.3.: Nucleosynthesis flow leading to the production of p-nuclei of molybdenum and ruthenium. Neutron-, proton- and α-dissociation reactions on more neutron-rich nuclei lead to the proton-rich isotopes and produce the p-nuclei directly or via β-decays of unstable nuclei in the γ-process. Radiative proton-capture reactions follow the neutron shell closure at $N = 50$ (gray lines) and lead to the p-nuclei ^{92}Mo.

The widely accepted model of the **γ-process** assumes that the p-nuclei are produced in sequences of photodisintegration reactions starting at r- and s-process nuclei as seed. The necessary temperatures are 2.0 to $3.5 \cdot 10^9$ K, which implies explosive conditions. Neutron-, proton- and α-dissociation reactions on more neutron-rich nuclei drive the masses towards the proton-rich side of the valley of stability, reaching the p-nuclei directly or via β-decays of unstable nuclei (see Figure 1.3). The explosive burning in the shock-heated Ne/O shell during a **Supernova type II** was identified as a possible production site [30–33].

However, nucleosynthesis simulations of Supernova type II models showed that the p-nuclei yields are not sufficient to explain the observed solar abundances of the p-nuclei. Overproduction factors describe how efficient a nucleosynthesis simulation reproduces the solar abundance distribution. The overproduction factor $\langle F_i \rangle$ is the ratio of the final abundance of an isotope i from the simulation and the observed solar value. Normalized by the mean overproduction F_0, $\langle F_i \rangle / F_0$ is equal to one if the simulation reproduces the isotopic abundance distribution correctly [33]. The overproduction factor of an isotope i is calculated by

$$\langle F_i \rangle = \frac{m_i}{M_{\text{tot}} X_{i\odot}}, \tag{1.1}$$

where m_i is the mass of the p-nucleus produced in the simulation, M_{tot} is the total mass of the simulated Ne/O shell, and $X_{i\odot}$ the solar mass fraction of the isotope (taken from [1]). The overproduction factors are normalized to the mean value F_0:

$$F_0 = \sum_i \frac{\langle F_i \rangle}{N_{\text{p}}}, \tag{1.2}$$

where N_{p} denotes the number of p-nuclei. Figure 1.4 shows the overproduction factors of the p-nuclei obtained within this work from a post-processing nucleosynthesis simulation using a Supernova type II model. The data points differ from one by up to two orders of magnitude.

The possible influence of the seed distribution on the simulation of a Supernova type II model was shown, e.g. by Pignatari et al., who investigated the nucleosynthesis in massive stars for different s-process yields due to uncertainties in the rate of the ^{12}C+^{12}C reaction. If the rate is increased, more s-process nuclei around strontium and heavier elements are synthesized. Hence, the light p-nuclei with mass numbers of 74 to 96 can be produced efficiently by neutron-dissociation reactions in the γ-process. However, the amount of mass ejected during the Supernova type II explosion and, consequently, the contribution to the solar p-nuclei abundances is still uncertain [34].

Supernovae type Ia were suggested as a possible additional production site to solve the problem of the underproduction of many p-nuclei [35]. Recent nucleosynthesis simulations showed that these supernovae might contribute to more than half of the p-nuclei abundances in the solar system. Suitable conditions for the γ-process are provided in the outermost
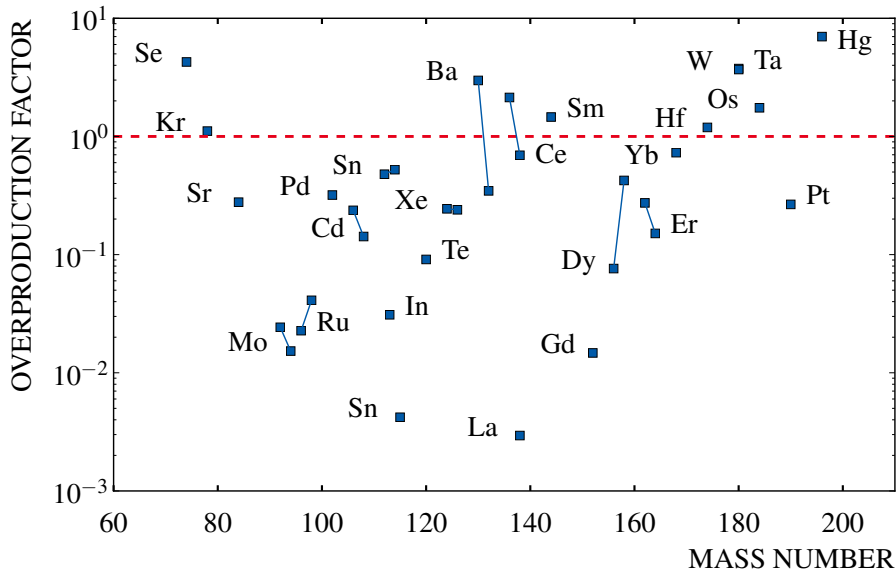
Figure 1.4.: Overproduction factors of the p-nuclei obtained within this work from a post-processing nucleosynthesis simulation using a Supernova type II model. Solid lines connect different isotopes of the same element. If the simulation reproduced the solar abundances of the p-nuclei, the overproduction factors would equal one. However, deviations of up to two orders of magnitude are present.

layers of Supernova type Ia models, while heavy nuclei are completely disintegrated down to the iron-nickel group in the inner regions with temperatures above $7 \cdot 10^9$ K [36, 37]. In addition, radiative proton-capture reactions may efficiently produce the light p-nuclei. The necessary protons originate from carbon burning [35]. The corresponding reaction paths may follow the isotopes at the neutron shell closure $N = 50$ and reach the light p-nuclei ^{92}Mo (Figure 1.3).

More speculative production scenarios for the p-nuclei, especially the light p-nuclei, describe extreme astrophysical environments in the universe. The p-nuclei may be synthesized in the rapid-proton-capture (rp) process in X-ray bursts or accretion disks around low mass black holes [38]. Strong neutrino fluxes in proton-rich ejecta of Supernovae create neutrons that are captured by neutron-deficient nuclei. The reaction flow of the νp-process may reach up to the light p-nuclei [39]. The ν-process contributes to the production of ^{138}La and ^{180}Ta. When the core of a massive star collapses and forms a neutron star, the high neutrino flux causes disintegration reactions on nuclei in the overlying shells. The available free protons and neutrons can in turn be captured by other nuclei. Hence, the ν-process may alter the abundance distribution and produce many rare isotopes [40].

1.2 Cross section and astrophysical rate

The probability of a nuclear reaction is described by the cross section σ:

$$\sigma = \frac{\frac{N_{\text{reaction}}}{t}}{\frac{N_{\text{projectile}}}{t} \cdot \frac{N_{\text{target}}}{A_{\text{target}}}}, \tag{1.3}$$

where $N_{\text{projectile}}/t$ is number of particles per time in the incoming channel, N_{reaction}/t is the number of reacted particles per time in the outgoing channel and $N_{\text{target}}/A_{\text{target}}$ is the number of target nuclei per area. A cross section is given in units of barn (1 b = 10^{-24} cm^2). The cross section depends on the center-of-mass energy E_{cm} of the involved particles. The rate $r_{XY}(E_{\text{cm}})$ of a reaction between two particles X and Y defines the number of reactions per volume and time for a given center-of-mass energy E_{cm}:

$$r_{XY}(E_{\text{cm}}) = N_X N_Y \cdot v(E_{\text{cm}}) \cdot \sigma(E_{\text{cm}}). \tag{1.4}$$

The variables N_X and N_Y denote the particle densities and $v(E_{\text{cm}})$ describes the relative velocity of the particles. The energy of the particles follows a distribution function $\phi(E)$, and $\phi(E)dE$ gives the probability of a particle having an energy in the interval $(E, E + \mathrm{d}E)$. The probability distribution integrated over all energy intervals is equal to one:

$$\int_0^\infty \phi(E)\mathrm{d}E = 1. \tag{1.5}$$

The total reaction rate for a stellar environment with a temperature T can be written as

$$r_{XY}(k_B T) = N_X N_Y \int_0^\infty \sigma(E) v(E) \phi(k_B T, E)\mathrm{d}E \tag{1.6}$$

where k_B denotes the Boltzmann constant. The Maxwell-Boltzmann distribution ϕ_{MB} has to be applied if two particles with mass are interacting:

$$\phi_{\text{MB}}(k_B T, E)\mathrm{d}E = \frac{2n}{(\pi k_B T)^{\frac{3}{2}}} \sqrt{E} \cdot \exp\left(-\frac{E}{k_B T}\right) \mathrm{d}E, \tag{1.7}$$

where n is the number of particles per volume and energy interval $(E, E + \mathrm{d}E)$. If a photon is involved in the reaction, the Planck spectral distribution ϕ_{Planck} has to be applied:

$$\phi_{\text{Planck}}(k_B T, E)\mathrm{d}E = \frac{1}{\pi^2(\hbar c)^3} \cdot \frac{E^2}{\exp(E/k_B T) - 1}\mathrm{d}E. \tag{1.8}$$

In this case, $v(E) = c$, and the total number of photons N_γ per unit volume is given by

$$N_\gamma = \frac{8\pi^4}{13c^3 h^3}(k_\mathrm{B}T)^3.$$

(1.9)

Detailed derivations can be found in the standard literature for nuclear astrophysics [41].

The equations derived describe ground state interactions of the nuclei. However, nuclei are thermally excited in stellar environments. Thus, all cross sections for the reactions on the nucleus in the ground state and in excited states contribute to the stellar cross section [42]. The contribution of excited states has to be calculated theoretically since to date only ground state contributions can be determined experimentally. However, one solution is the measurement of excited state contributions in the outgoing channel of the reverse reaction. Photons emitted from the de-exciting product nuclei can be detected to identify the corresponding excited state. The calculation of cross sections for forward and reverse reaction are connected via the theory of detailed balance [43].

Compilations of nuclear reaction rates are stored in reaction libraries, such as the Basel reaction library [44] and the JINA Reaclib Database V1.1 [45]. The available data include rates calculated from experimentally as well as from theoretically obtained cross sections. Many theoretically predicted cross sections are calculated using the Hauser-Feshbach statistical model. The model describes the formation of a compound nucleus due to nuclear interactions. The compound nucleus exhibits a high level density. Hence, its decay into an energetically allowed reaction channel can be described statistically [46]. The reaction libraries provide stellar reaction rates r^star as a function of temperature with the parametrization:

$$r^\mathrm{star}(T_9) \propto \exp(a_0 + a_1 T_9^{-1} + a_2 T_9^{-1/3} + a_3 T_9^{1/3} + a_4 T_9 + a_5 T_9^{5/3} + a_6 \ln(T_9)),$$

(1.10)

where T_9 denotes the temperature in $10^9 \mathrm{K}$. The data from the reaction libraries are used in large-scale nucleosynthesis calculations, which require a complete reaction network.

1.3 Aim of the thesis

This work aims at contributing to the understanding of the nucleosynthesis of the light p-nuclei ^{94}Mo and ^{92}Mo. According to recent stellar model calculations, ^{94}Mo is mainly synthesized via the (γ,n) photodisintegration chain starting from the neutron-rich molybdenum isotopes (compare Figure 1.3) [37]. The determination of the cross section of the ^{94}Mo(γ,n) reaction is necessary to understand the abundance ratio of ^{94}Mo to ^{92}Mo. If the reaction ^{94}Mo(γ,n) is possible in a certain stellar environment, the photodisintegration of ^{93}Mo will follow immediately because of the lower neutron separation energy of ^{93}Mo (Table 1.1). The closed neutron shell at ^{92}Mo terminates the photo-neutron chain of the molybdenum isotopes.

Isotope	S_n (MeV)	S_{2n} (MeV)	S_p (MeV)
^{100}Mo	8.29	14.2	11.15
^{94}Mo	9.68	17.7	8.49
^{93}Mo	8.07	20.7	7.64
^{92}Mo	12.67	22.8	7.46

Table 1.1.: Neutron (S_n), two-neutron (S_{2n}) and proton (S_p) separation energies of the isotopes ^{100}Mo, ^{94}Mo, ^{93}Mo and ^{92}Mo [47].

The analysis of the photodisintegration reactions of ^{94}Mo measured by Coulomb dissociation at the LAND/R^{3}B setup at GSI Helmholtzzentrum für Schwerionenforschung in Darmstadt, Germany, is described in this thesis. The isotopes ^{92}Mo, ^{93}Mo and ^{100}Mo were also investigated within the experimental campaign (compare Figure 1.5). The Coulomb dissociation cross sections of the nuclei ^{92}Mo, ^{93}Mo and ^{100}Mo were analyzed by O. Ershova and published in her thesis [48].

The measurements aimed at validating the method of Coulomb dissociation by comparing the results with real photon experiments, which are available for the stable isotopes ^{92}Mo, ^{94}Mo and ^{100}Mo [49, 50]. The (γ,n) cross section of the unstable isotope ^{93}Mo could be determined for the first time [48, 51]. The complex analysis procedure of the Coulomb dissociation reactions of ^{94}Mo is described in Chapter 2 of this thesis. The same analysis was carried out for the isotope ^{100}Mo for comparison with the independent analysis of O. Ershova. The results for the stable molybdenum isotopes are compared with real photon experiments carried out at the Saclay linear accelerator by Beil et al. [49].

Figure 1.5.: Isotopic chain of the molybdenum isotopes. The photodisintegration reactions of the stable isotopes ^{92}Mo, ^{94}Mo and ^{100}Mo and the unstable isotope ^{93}Mo were measured by Coulomb dissociation at the LAND/R^{3}B setup.

The production of the p-nuclei in the isotopic chains of Mo and Ru was investigated in post-processing nucleosynthesis simulations within the NuGrid research platform [52]. The simulations for a Supernova type II and a Supernova type Ia model are described in Chapter 3. The simulations using a Supernova type II model aimed at identifying the relevant production and destruction rates and at determining the sensitivity of the final mass fractions to these rates. For the first time, nucleosynthesis simulations using a Supernova type Ia model were carried out with the NuGrid post-processing nucleosynthesis code. The parameters of stellar environments were adopted from simulations of Travaglio et al. [53]. After a validation of the resulting abundance distribution by a comparison with Travaglio et al., the production of the p-nuclei ^{92}Mo and ^{94}Mo is investigated in detail.

2 Coulomb dissociation of ^{94}Mo at the LAND setup

The analysis of the Coulomb dissociation of ^{94}Mo measured at the LAND setup is presented in this chapter. The isotopes ^{92}Mo, ^{93}Mo and ^{100}Mo were also investigated within the experimental campaign. The Coulomb dissociation reactions of these isotopes were analyzed by O. Ershova and published in her thesis [48]. The current analysis of the ^{94}Mo data is also carried out for the ^{100}Mo data to compare the results and validate the independent analyses.

2.1 Coulomb dissociation

Most nuclei undergoing photodissociation reactions in explosive scenarios are unstable and cannot be prepared as a sample for experiments using real photons. The study of the photodissociation reaction on unstable nuclei in inverse kinematics by Coulomb dissociation is one solution. The nucleus under investigation impinges on a high-Z target, typically a lead (Pb) target, and interacts with the time-varying, Lorentz-contracted electromagnetic field of the nucleus (Figure 2.1). The projectile can be excited by a virtual photon. Neutrons, protons or α-particles can be emitted by the nucleus if the excitation energy is higher than the particle separation energies. Hence, for example, the neutron-dissociation reaction is measured as $^{\mathrm{nat}}\mathrm{Pb}(^{A}X,^{A-1}X+\mathrm{n})^{\mathrm{nat}}\mathrm{Pb}$. In the following, $^{A}X(\gamma,\mathrm{n})^{A-1}X$ and $^{\mathrm{nat}}\mathrm{Pb}(^{A}X,^{A-1}X+\mathrm{n})^{\mathrm{nat}}\mathrm{Pb}$ will be used synonymous. The fragment and the emitted particles are kinematically focused in forward direction with energies of approximately beam energy.

The equivalence of the excitation of a nucleus by real photons and the interaction with an electromagnetic field of a highly-charged nucleus was first described by Fermi [54] and developed further by Weizsäcker [55] and Williams [56] accounting for relativistic effects. Baur, Bertulani and Rebel showed that the energy-dependent Coulomb dissociation cross
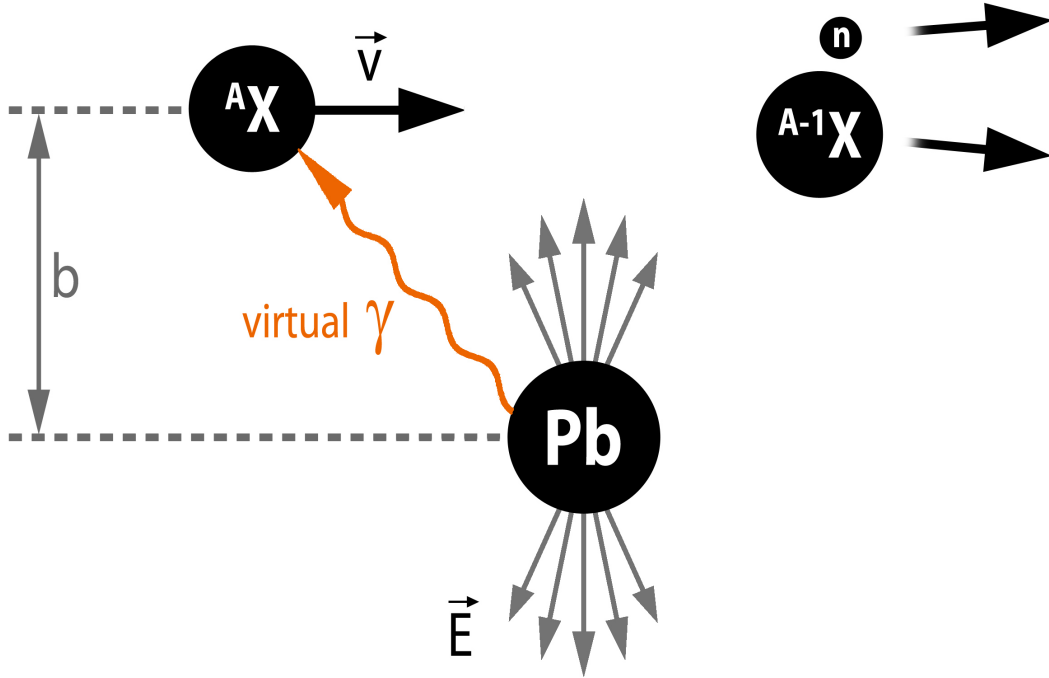
Figure 2.1.: Schematic view of the Coulomb dissociation process of a nucleus $^A X$. The example of a neutron dissociation is shown. The projectile impinges on a lead target (Pb) at an impact parameter b. The electromagnetic field E of the lead nucleus seen by the projectile is Lorentz-contracted. The projectile can be excited by the exchange of a virtual photon. If the excitation energy is higher than the neutron separation energy, a neutron can be emitted by the nucleus.

section can be expressed as the sum of the photoabsorption cross sections $\sigma_{\pi\lambda}^{\gamma}$ for all multi-polarities $\pi\lambda$ (parity and angular momentum) of the virtual photon field [57]:

$$\sigma_{\text{CD}}(E) = \int \sum_{\pi\lambda} \frac{1}{E} n_{\pi\lambda}(E) \sigma_{\pi\lambda}^{\gamma}(E) \mathrm{d}E. \tag{2.1}$$

A detailed description of the derivation can be found in the review article of Bertulani and Baur [58]. The coefficients $n_{\pi\lambda}(E)$ represent the energy-dependent number of virtual photons, which can be calculated from the kinematics of the reaction:

$$n_{\mathrm{E}1}(E) = \frac{2}{\pi} Z_T^2 e^2 \alpha \left(\frac{c}{v}\right)^2 \left(\xi K_0(\xi) K_1(\xi) - \frac{v^2\xi^2}{2c^2} \left[K_1^2(\xi) - K_0^2(\xi)\right]\right), \tag{2.2}$$

$$n_{\mathrm{E}2}(E) = \frac{2}{\pi} Z_T^2 e^2 \alpha \left(\frac{c}{v}\right)^4 \left(2\left[1 - \frac{v^2}{c^2}\right] K_1^2(\xi) + \xi \left[2 - \frac{v^2}{c^2}\right]^2 K_0(\xi) K_1(\xi)\right.$$
$$\left. - \frac{\xi^2 v^4}{2c^4} \left[K_1^2(\xi) - K_0^2(\xi)\right]\right), \tag{2.3}$$

$$n_{\mathrm{M}1}(E) = \frac{2}{\pi} Z_T^2 e^2 \alpha \left(\xi K_0(\xi) K_1(\xi) - \frac{\xi^2}{2} \left[K_1^2(\xi) - K_0^2(\xi)\right]\right), \tag{2.4}$$

$$\xi = \frac{E b_{\min}}{\hbar \gamma \beta c} \qquad \text{(adiabatic parameter)}$$

where K_i are the modified Bessel functions of order i and $\alpha = e^2/\hbar c$ is the fine-structure constant. The adiabatic parameter ξ denotes the ratio of the interaction time and the excitation time. Figure 2.2 shows the virtual photon numbers of the three main multipolarities E2, E1 and M1 for ^{94}Mo ions impinging on a $^{\mathrm{nat}}$Pb target with a beam energy of 500 AMeV. An excitation of the projectile nucleus is only feasible if the interaction time is larger than the excitation time. The maximum excitation energy transferred to the projectile can be calculated by setting $\xi = 1$:

$$E_{\max} = \frac{\hbar \gamma \beta c}{b_{\min}}. \tag{2.5}$$

The virtual photon numbers drop exponentially for $\xi > 1$. The minimal impact parameter $b_{\min}$ is derived from the parametrization for relativistic heavy-ion collisions of Benesh, Cook and Vary [59]:

$$b_{\min} = 1.34 \,\mathrm{fm} \cdot \left[A_{\mathrm{Pb}}^{\frac{1}{3}} + A_{\mathrm{projectile}}^{\frac{1}{3}} - 0.75 \cdot \left(A_{\mathrm{Pb}}^{-\frac{1}{3}} + A_{\mathrm{projectile}}^{-\frac{1}{3}}\right)\right]. \tag{2.6}$$

Using Equations (2.5) and (2.6), the maximum excitation energies for the nuclei ^{100}Mo, ^{94}Mo and ^{92}Mo impinging on a Pb target are 16.7 MeV (beam energy 500 AMeV), 16.9 MeV (beam energy 497.95 AMeV) and 17.3 MeV (beam energy 518.7 AMeV), respectively. The reaction channel ^{94}Mo(γ,2n) is not expected to be visible in the data because the two-neutron separation energy of 17.7 MeV for the nucleus ^{94}Mo is higher than the maximum excitation energy (Table 1.1).

Besides the Coulomb dissociation measurement with a lead target, two additional measurements were carried out to determine the fractions of nuclear interactions in the target and interactions with the setup: measurements with a carbon target ("C target") and without target ("no target"). The background subtraction is described in Section 2.3.4.
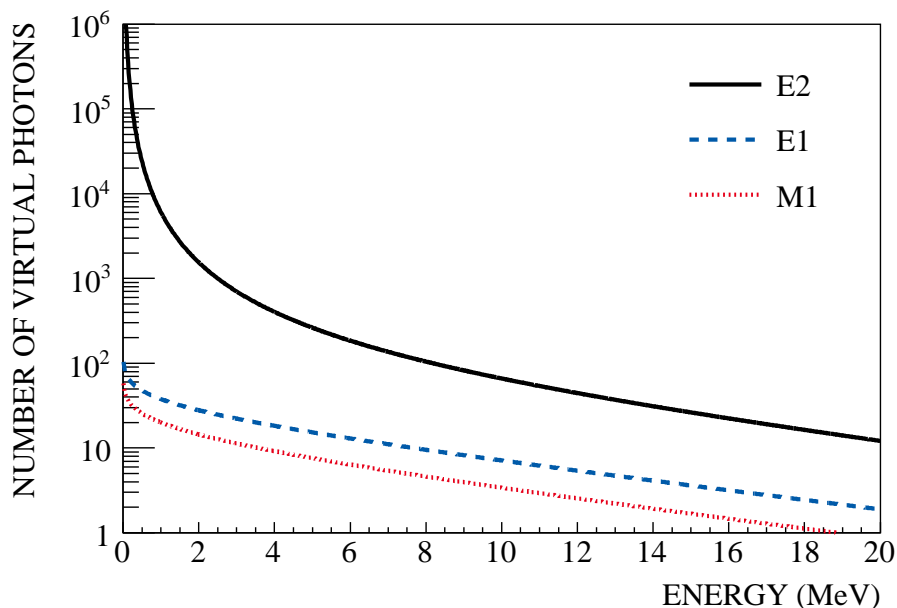
Figure 2.2.: Virtual photon numbers as a function of the excitation energy for the three main multipolarities E2, E1 and M1 for ^{94}Mo ions impinging on a ^{nat}Pb target with a beam energy of 500 AMeV.

2.2   LAND setup to study Coulomb dissociation

Coulomb dissociation reactions can be studied at the LAND setup. The setup allows the identification and kinematic reconstruction of the reactions. To determine the integral Coulomb dissociation cross section of the reaction $^AX(\gamma,\text{n})^{A-1}X$, the incoming ions ^AX have to be identified at first. Their charge number, mass number (in the case of a beam with different ion species) and interaction times are measured. Dissociated neutrons are identified and their kinematics from position and time measurements are recorded. To identify the element X after the reaction, again, the charge number is determined. The charged fragment ^{A-1}X is deflected by a magnet. Several detectors record the fragment's hit position to reconstruct its trajectory. The mass number A of the fragment with charge number Z can be calculated from the deflection in the magnetic field. Section 2.2.2 gives an overview of the LAND setup and the detectors used in the molybdenum experiment. The detectors and their calibration are described in Sections 2.2.3 and 2.2.4.

2.2.1 GSI accelerator facility

Figure 2.3 shows a schematic drawing of the GSI accelerator complex and the experimental area where the LAND setup is located (Cave C). The ions are accelerated up to an energy of 11.4 AMeV by the UNIversal Linear ACcelerator (UNILAC). The ions are then injected into the SchwerIonenSynchroton SIS18 (German for heavy ion synchrotron). The SIS18 accelerates protons to up to 4.5 GeV and uranium ions to up to 1 AGeV. Primary beams of ^{94}Mo and ^{100}Mo were accelerated to energies of 500 AMeV and 497.95 AMeV during the molybdenum experiment. They were guided to the LAND setup in Cave C via the FRagment Separator (FRS) [60–62].
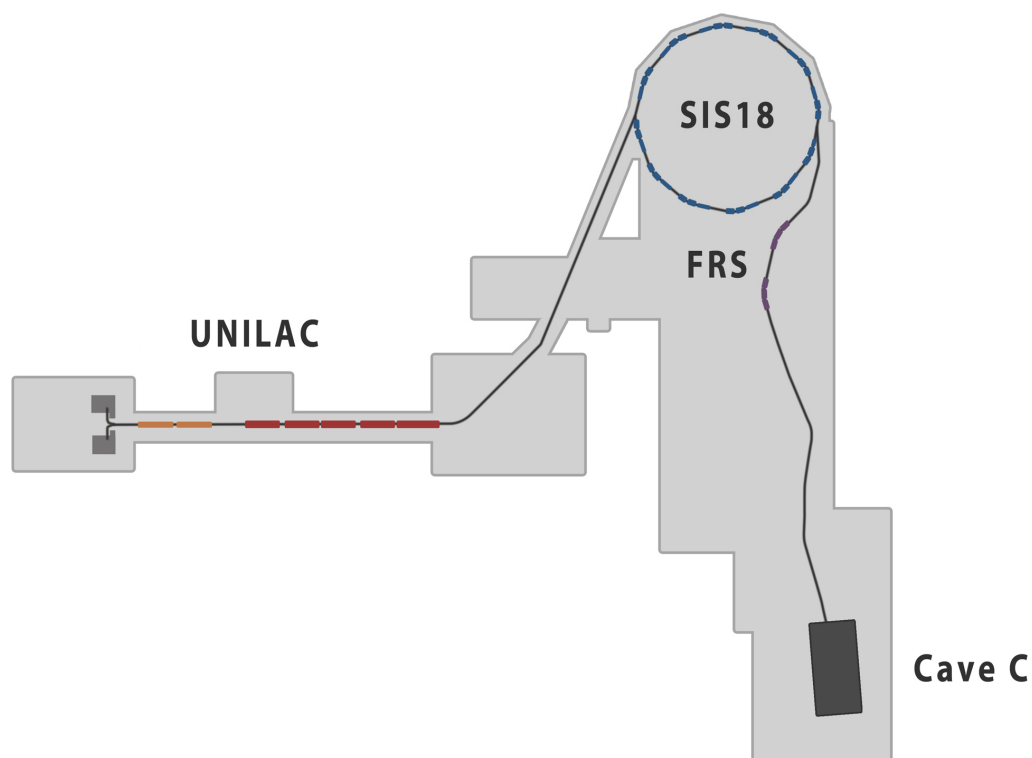
Figure 2.3.: Accelerator facility at GSI Helmholtzzentrum für Schwerionenforschung, Darmstadt, Germany. The ions from the source were pre-accelerated by the UNILAC (UNIversal Linear ACcelerator). After injection, the ions were accelerated to about 500 AMeV in the SIS18 (SchwerIonenSynchroton, German for heavy ion synchrotron). The beam was then directed to Cave C via the FRS (FRagment Separator).

2.2.2   LAND experimental setup

Figure 2.4 shows the LAND experimental setup for the molybdenum experiment. The primary beam from SIS18 entered the experimental area Cave C. Beam spills with intensities of up to $5 \cdot 10^4$ were delivered. The POS scintillation detector recorded the time of each ion passing the detector. Two PSP detectors (Position Sensitive Pin diode) in front of the target measured the position of the ion to reconstruct the position on the target, as well as the energy loss in the detector to identify the ion's charge. The ROLU detector (Rechts Oben Links Unten, German for right top left bottom) restricted the beam. It consists of four plastic scintillators acting as a veto. The ROLU scintillators create a rectangular beam window with variable size (2.0x2.0 cm^2 during the molybdenum experiment). If an ion hits the detector, the event is not recorded [63].

The beam hit the target located at the entrance of the CsI gamma detector. The CsI detector measures gamma-rays emitted by the excited reaction fragment [64, 65]. It was not working correctly in the experiment, which was extensively investigated in the theses of O. Ershova and A. Movsesyan [48, 66]. The detector was therefore not used in the analysis presented here.

After the target, the fragment passed the PSP3 detector, which again provided a position and energy loss measurement. The charged reaction fragment was deflected by the magnetic field of ALADIN (A Large Acceptance DIpole magNet). The fragment arm was located at 13.3° with respect to the incoming beam. Three large-area scintillating fibre detectors GFI detected the horizontal deflection of the fragment. The ions travelled through a large vacuum chamber and a vacuum pipe (not shown in Figure 2.4) up to the second GFI detector. The TFW (Time-of-Flight Wall) at the end of the fragment arm again measured the position, time and energy loss of the ions.

Dissociated neutrons from the reactions are not affected by the magnetic field and hit LAND (Large Area Neutron Detector). A plastic-scintillator Veto wall was installed in front of LAND. It detects charged particles from background events, which also generate a signal in LAND, and therefore helps to identify neutrons.

The following sections briefly describe the detectors used for the analysis of the Coulomb dissociation reaction of ^{94}Mo and their calibration.
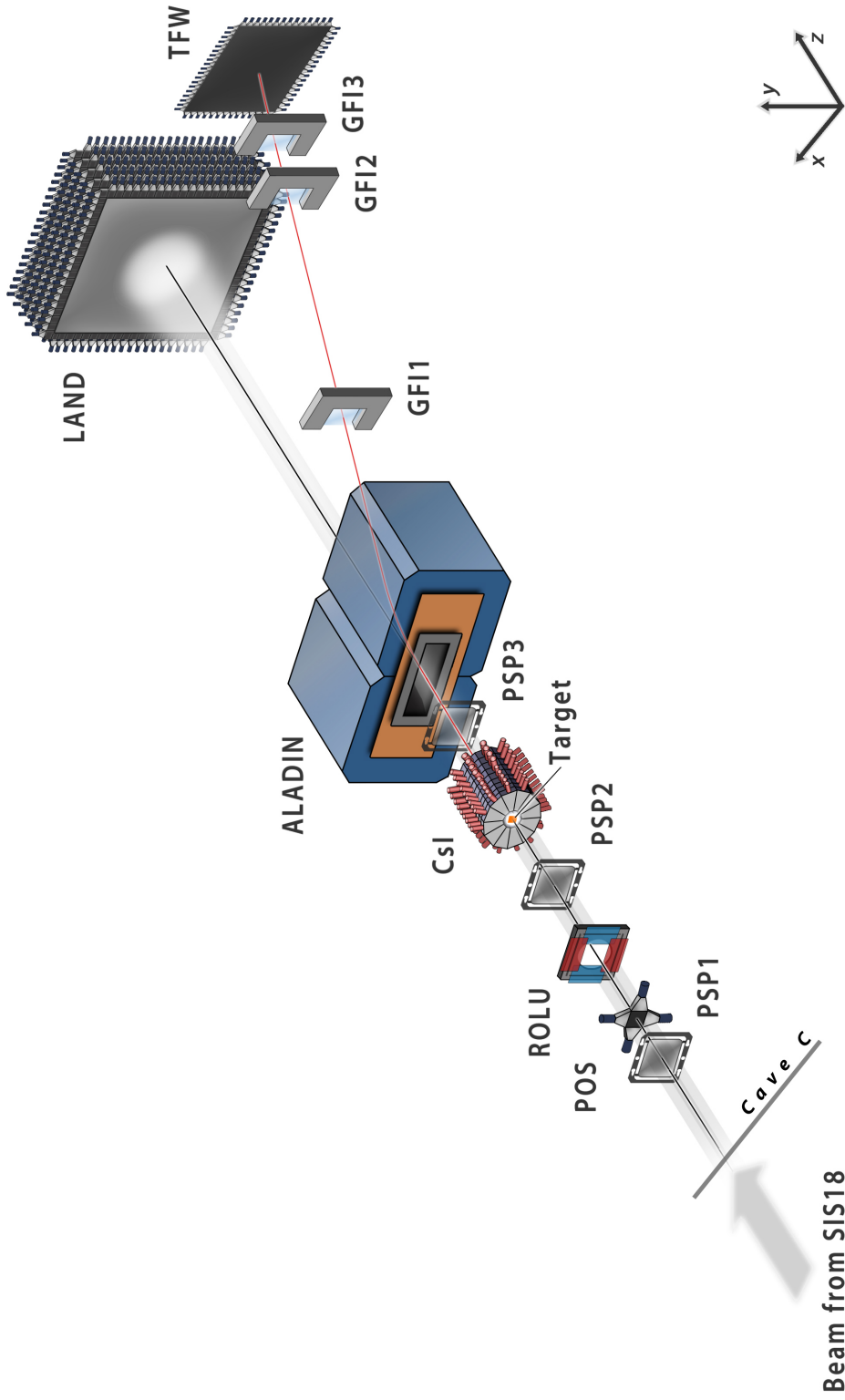
Figure 2.4.: LAND experimental setup for the molybdenum experiment (not to scale). The ions passed through the POS, PSP1, ROLU and PSP2 detectors in front of the target, which recorded time, position and energy loss. The target was positioned at the entrance of the CsI gamma detector. The ions passed the PSP3 detector behind the target. They were deflected in the magnetic field of ALADIN. The position, time and energy loss of the ions were measured by the GFI detectors and the TFW. Neutrons from dissociation reactions hit LAND unaffected by ALADIN. (Image created by Mario Weigand.)

2.2.3   Detectors of LAND setup

PSP - Position Sensitive Pin diode

The Position Sensitive silicon Pin diode has an active area of 4.5x4.5 cm^2 and a thickness of 300 μm. The PSP measures position and energy loss of an ion passing the detector. The hit position is reconstructed via four charge measurements, one on each corner of the detector. The charge collected by each anode depends linearly on the distance to the hit position since the deposited charge is shared additively. Another single read-out channel measures the total deposited charge on the cathode side. The charge of the ion is calculated from the energy loss via the Bethe formula [48, 67].

Two PSP detectors were located at distances of about 220 cm and 70 cm in front of the target. Their position measurements were used to determine the position of the incoming ion on the target. PSP3 was placed about 70 cm behind the target and measured one track point of the fragment's trajectory.

POS - POSition detector

The POS detector is a thin quadratic plastic scintillator with a size of 5.5x5.5 cm^2 and a thickness of 200 μm. The scintillation light is detected by four photomultipliers. The mean value of the time signals provided by the photomultipliers gives the reference time for all detectors in the experiment. A time resolution of $\sigma_{POS} \approx 25$ ps can be reached [48, 68, 69]. The POS detector was originally used for position measurements. However, it was only used for time measurements during the molybdenum experiment since the PSP detectors provided more accurate position measurements.

LAND - Large Area Neutron Detector

The Large Area Neutron Detector measures the hit position and time of flight of neutrons with energies in the range of 100 to 1000 MeV. It consists of 200 paddles with a size of 200x10x10 cm^3 each. Each paddle is made of eleven iron sheets (5 mm thick, outer sheets 2.5 mm thick) and ten sheets of 5 mm thick scintillator. The iron sheets serve as passive converters where neutron interactions produce charged particles, which in turn create signals in the scintillators. The stacks of iron and scintillation material are encased by 1 mm iron. Twenty paddles are assembled in each of the ten detector planes. Consecutive planes are orientated perpendicular to each other to improve the position resolution of LAND by

providing position measurements in vertical and horizontal directions. The resulting depth of the detector is 1 m [70].

The scintillation light is collected by light guides and directed to photomultipliers on both ends of a paddle. The hit position inside the paddle is calculated from the time difference between the signals on both ends. The time of flight of the neutron is obtained from the mean time.

GFI - Large-area scintillation fiber detector

The large-area scintillation fiber detector GFI measures the horizontal position (x-position) of the fragment trajectory behind ALADIN. A GFI detector consists of 475 scintillation fibers with a cross section of 1x1 mm^2 and covers an active area of 50x50 cm^2. The fibers are cladded to avoid cross talk between neighbouring fibers. One end of each fiber is coupled to a position-sensitive photomultiplier (PSPM). The anode of the PSPM consists of a rectangular grid of 18x16 wires. Scintillation light from a fiber is guided to the PSPM and induces a signal in a few anode wires. The position of the light spot is determined from the position on the grid and the fiber hit by an ion is identified. The position resolution is thus determined by the width of the fiber of 1 mm [71, 72].

TFW - Time-of-Flight Wall

The Time-of-Flight Wall (TFW) is used for position and energy-loss measurements at the end of the fragment arm in the analysis presented here. It consists of 18 vertically (x-paddles) and 14 horizontally (y-paddles) aligned plastic scintillator paddles, which are arranged in two detector planes. Each paddle is 10.5 cm wide and 0.5 cm thick. The x-paddles are 147 cm long, the y-paddles are 189 cm long. The paddles are read out by photomultiplier tubes at both ends.

2.2.4 Detector calibration

The detectors of the LAND setup provide time and charge or amplitude measurements. These data have to be converted into a user-specified format and calibrated. The program *land02*, which was developed by H. Johansson and R. Plag, processes the data for further analysis. Several other programs are used to obtain the calibration parameters, which are necessary for the data processing with *land02* [67, 73].

The detector calibration is a three-step process: (1) Measured times are converted from channels to ns and offsets induced by the electronics are subtracted from measured energy values. (2) All channels of the detectors are synchronized internally to provide time (ns), energy (MeV) and position (cm) data. (3) The detectors are synchronized relative to each other. Detailed descriptions of the calibration process and the corresponding data levels are given in the theses of S. Paschalis [74], D. Rossi [68] and O. Ershova [48]. Here, the steps for data processing and calibration are discussed only briefly. Several members of the LAND collaboration had already analyzed data of the experiment. Hence, most of the calibration parameters required for the analysis presented here were already available. Specific adjustments for the ^{94}Mo data are presented in the following. The calibration parameters for the POS detector were provided by Olga Ershova [48]. Special effort was put into the calibration of the TFW.

QDC pedestals and TDC gain calibration

A QDC converts charge signals to digital values. A signal from a detector charges the QDCs capacitor, on which a voltage can be measured. To ensure linear and time-constant operation, a bias voltage is set on the integrator circuit. This non-zero voltage is detected as a "pedestal" when detector signals are absent. The pedestals are determined by the *clock* routine provided within the *land02* framework and subtracted from the physical data [73].

A TDC translates time information from channel numbers to time units. The TDC gain calibration parameters map recorded channels and detected times. A time calibrator creates signal pairs with certain intervals. One signal serves as a *tcal* trigger, the other signal is sent to the TDCs. A linear fit of the TDC gain as a function of time determines the channel-to-time conversion parameters [73, 74].

PSP and GFI calibration

The position calibration of the PSP and GFI detectors makes use of masks, which produce a geometric signal pattern on the detectors. The procedure is described in detail by S. Paschalis [74] and K. Mahata et al. [72].

Active pixel masks are inserted in front of each PSP detector during PSP calibration runs. The Pixel detector consists of 21x21 scintillating square pixels, which are arranged in a grid. When an ion hits the Pixel detector, it triggers the PSP detector readout. The pattern of measured positions by the PSP reflects the pattern of the pixel mask. The position calibration aims at removing distortions in the geometric pattern due to non-linearities of the PSP detec-

tor and its readout. The calibration of the PSPs for the molybdenum experiment was carried out by A. Movsesyan [66].

The fibers of the GFI detectors are connected to a position-sensitive photomultiplier which consists of a rectangular wire grid. In a GFI calibration run, the ion beam is swept over the detectors, illuminating all fibers. The resulting position signal pattern can be calibrated according to the procedure described for the PSP detectors. O. Ershova calibrated the GFI detectors for the molybdenum experiment [48].

TFW calibration

The calibration of the TFW was carried out for the paddles hit by the beam spot. Figure 2.5 illustrates the paddles which recorded data for the different target runs. Five x-paddles (vertical) and four y-paddles (horizontal) were hit in the Pb target runs, three x-paddles and two y-paddles in the C and no target runs, depending on the scattering in the target material.

The QDC pedestals and TDC gain calibration were carried out using the programs *clock* and *tcal*. The raw data could be translated into measured times t_1 and t_2, as well as energies E_1 and E_2 by the photomultipliers with these calibration parameters. Figure 2.6 shows a scintillating paddle which is hit by an ion with an energy E_0 at time t_0. Time and energy signals are detected on both sides. The time of the hit can be calculated from the times measured by the photomultipliers [48, 67]:

$$t_1 = t_0 + \frac{\frac{L}{2} + x}{v}, \ t_2 = t_0 + \frac{\frac{L}{2} - x}{v}, \tag{2.7}$$

where L is the length of the scintillating paddle and v is the effective speed of light in the scintillating material. It follows

$$t_0 = \frac{t_1 + t_2}{2} - \frac{L}{2v}. \tag{2.8}$$

The energy loss of the ion can be calculated from the measured energies E_1 and E_2 assuming an exponential light attenuation λ in the paddle.

$$E_1 = E_0 \exp\left(-\frac{\frac{L}{2} + x}{\lambda}\right), E_1 = E_0 \exp\left(-\frac{\frac{L}{2} - x}{\lambda}\right), \tag{2.9}$$

$$E_0 = \sqrt{E_1 E_2} \exp\left(\frac{L}{2\lambda}\right). \tag{2.10}$$

The hit positions can be determined from Equations (2.7) and (2.9).

$$x = v\frac{t_1 - t_2}{2}, \tag{2.11}$$
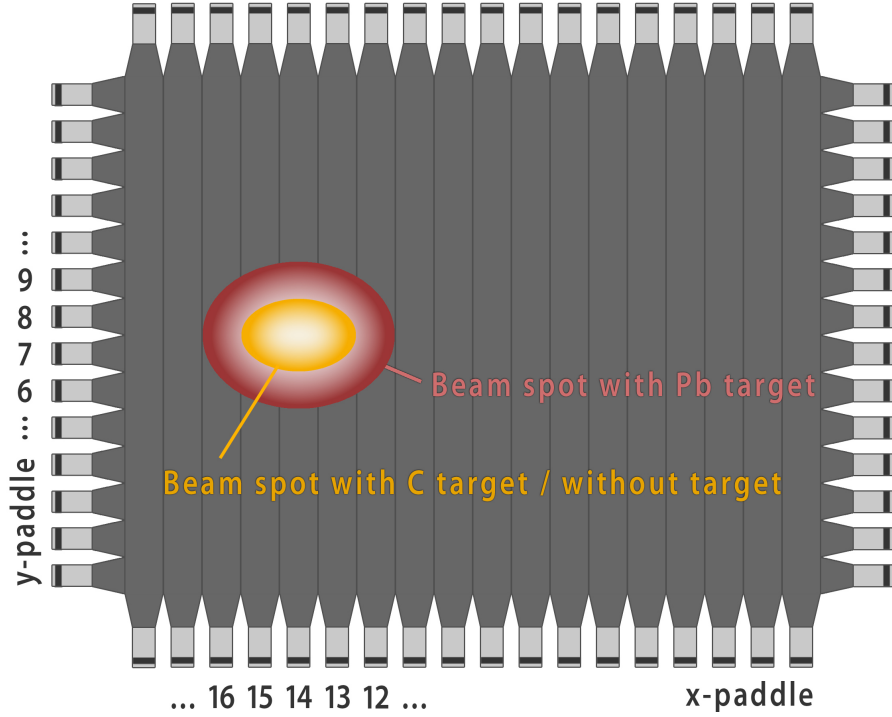
Figure 2.5.: Schematic drawing of the TFW. It consists of 18 vertically (*x*-paddles) and 14 horizontally (*y*-paddles) aligned plastic scintillator paddles. Each paddle is read out with two photomultipliers. Time and energy information are stored independently. The ellipses show the size and position of the beam spots on the paddles for the different targets.

$$x = \frac{\lambda}{2} \cdot \ln \frac{E_2}{E_1}. \tag{2.12}$$

In the next calibration step, the two photomultipliers of each paddle are synchronized. The parameter t_{diff} is introduced to calculate the synchronized times t_1^{s} and t_2^{s} from the measured times t_1 and t_2 [48]:

$$t_1^{\text{s}} = t_1 + t_{\text{diff}}, \tag{2.13}$$

$$t_2^{\text{s}} = t_2 - t_{\text{diff}}. \tag{2.14}$$

The hit position in the paddle can be written as

$$x = v \frac{t_1^{\text{s}} - t_2^{\text{s}}}{2} = v \left(\frac{t_1 - t_2}{2} + t_{\text{diff}} \right), \tag{2.15}$$

applying the condition that the light arrives at the photomultipliers at the same time when the paddle is hit at position $x = 0$. The parameters v and t_{diff} are determined by a linear fit of
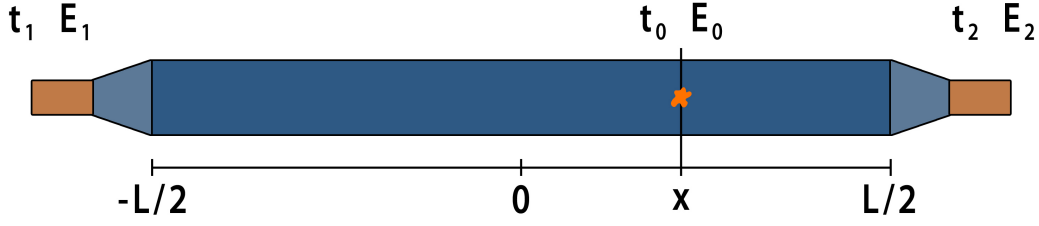
Figure 2.6.: Reconstruction of time t_0 and energy E_0 measured by a scintillating paddle with length L hit by an ion at position x. Time and energy are measured at both ends, allowing to calculate t_0 and E_0.

the dependence of x and t_1 - t_2 using known positions from crossing x- and y-paddles hit by the same ion and measured times from the photomultipliers.

The energy synchronisation of the photomultipliers of a paddle is treated according to the time synchronisation, resulting in the synchronized energies [68]

$$E_1^s = E_1 \cdot E_{\text{diff}}, \tag{2.16}$$

$$E_2^s = E_2 \cdot \frac{1}{E_{\text{diff}}}. \tag{2.17}$$

The times and energies of all TFW paddles are synchronised in the final calibration step. For each event, the times and energies measured with crossing paddles have to be equal. The calibration parameters t_{sync} and E_{sync} are introduced, and the final equations for the measured times and energies of the photomultipliers of each paddle can be written as [48]:

$$t_1^s = t_1 + t_{\text{diff}} + t_{\text{sync}}, \tag{2.18}$$

$$t_2^s = t_2 - t_{\text{diff}} + t_{\text{sync}}, \tag{2.19}$$

$$E_1^s = E_1 \cdot E_{\text{diff}} \cdot E_{\text{sync}}, \tag{2.20}$$

$$E_2^s = E_2 \cdot \frac{1}{E_{\text{diff}}} \cdot E_{\text{sync}}. \tag{2.21}$$

The calibration parameters in Equations (2.18) to (2.21) were generated with the program *phase1*. The resulting reconstructed energy loss (according to Equation (2.10), without the constant factor) is shown in Figure 2.7 (left panel) for a subset of the Pb target data for ^{94}Mo. The automatic synchronisation of the paddles was not satisfactory, therefore, manual

gain corrections were performed. The resulting distributions are shown in Figure 2.7 (right panel).

The energy resolution differs strongly for the TFW paddles. O. Ershova discussed possible reasons for insufficient synchronization and resolution in her thesis [48]. Further investigations are shown in Section 2.2.5.
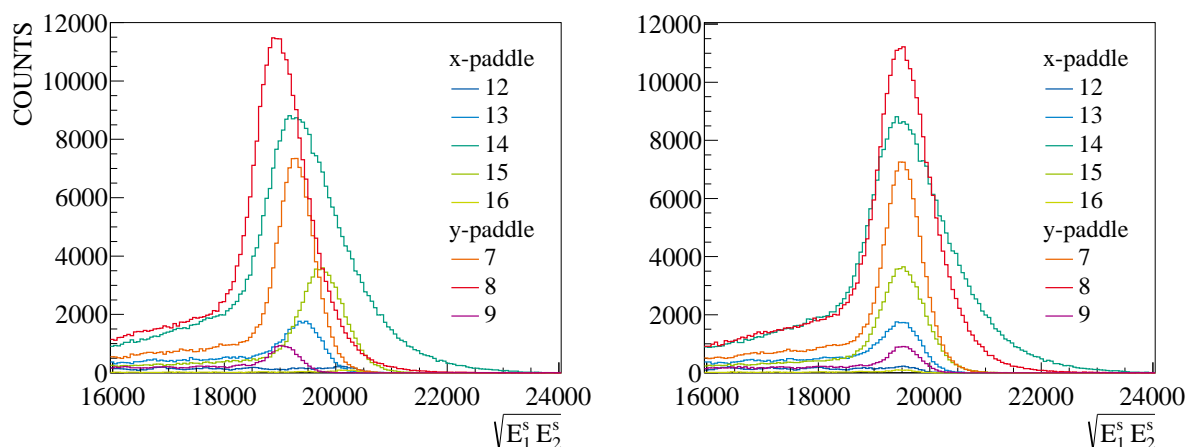
Figure 2.7.: Gain correction for the TFW. Left panel: The parameters t_{sync} and E_{sync} from the automatic calibration routine *phase1* were applied. Right panel: An additional manual gain correction was applied. A subset of the Pb target data for ^{94}Mo is shown.

LAND calibration

LAND is calibrated in the same manner as the TFW. The LAND calibration parameters were taken from O. Ershova [48]. The global time offset for LAND had to be determined for the ^{94}Mo data.

The POS detector defines the start time for all detectors as well as the time of interaction in the target. The time of flight of neutrons and fragments is determined by the time between the interaction in the target and the signals detected by LAND and the TFW, respectively. Absolute times obtained from the detectors are influenced by the electronic readout. Hence, the time differences between two detectors are adjusted by the time offset parameters.

The kinematics of the reaction was investigated to determine the offset parameter. It is expected that the difference between the mean neutron velocities and the mean fragment velocities equals zero in the laboratory system. The recoil of the target nucleus can be neglected. The LAND time offset parameter was chosen accordingly for each target setting.

LAND efficiency and acceptance

The knowledge of the LAND neutron detection efficiency is essential for the analysis of neutron-dissociation reactions. The data processing by *land02* reconstructs neutron hits from the showers induced in LAND and discriminates events caused by γ-rays emitted in the target, scattered ions and cosmic particles. The shower algorithm misinterprets neutrons with a certain probability depending on the kinetic energy of the neutrons. In addition, 25% of the LAND paddles were not working properly during the molybdenum experiment due to broken photomultipliers or high threshold settings for the readout electronics.

The LAND efficiency and acceptance was simulated by D. Rossi, taking into account the neutron detection efficiencies, inactive paddles, effective thresholds and the geometrical acceptance of the detector. A detailed description of the simulation process is given in the thesis of D. Rossi [68]. Figure 2.8 shows the resulting LAND efficiency and acceptance for one-neutron-dissociation reactions on ^{94}Mo as a function of the neutron kinetic energy in the rest frame of the incoming ion for the ^{94}Mo beam setting. One-neutron events can be reconstructed with up to 80% efficiency at low kinetic energies.
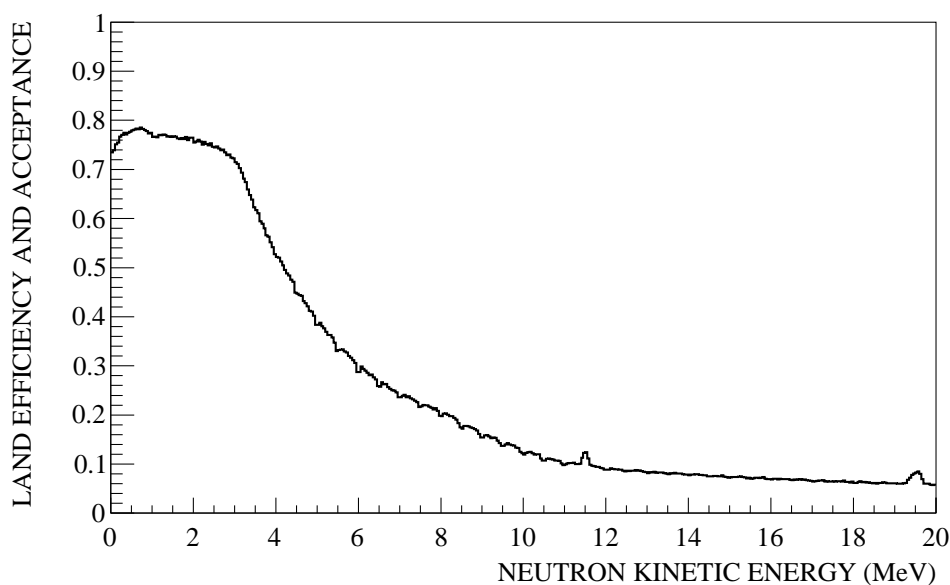
Figure 2.8.: Total LAND efficiency and acceptance for one-neutron-dissociation reactions on ^{94}Mo as a function of the neutron kinetic energy in the projectile rest frame. Data provided by D. Rossi.

The efficiency and acceptance correction introduces a systematic uncertainty of 8% on the Coulomb dissociation cross section of one-neutron separation channels. It originates from discrepancies in the experimental and simulated LAND data due to the resulting neutron hit distributions and energy spectra [48, 68].

2.2.5 TFW charge resolution

Figure 2.9 shows the fragment charge measured by the TFW and the PSP3. The TFW detects charge signals with a large spread around the expected value of $Z = 42$. This spread causes a bad resolution of the charge measurement with the TFW.
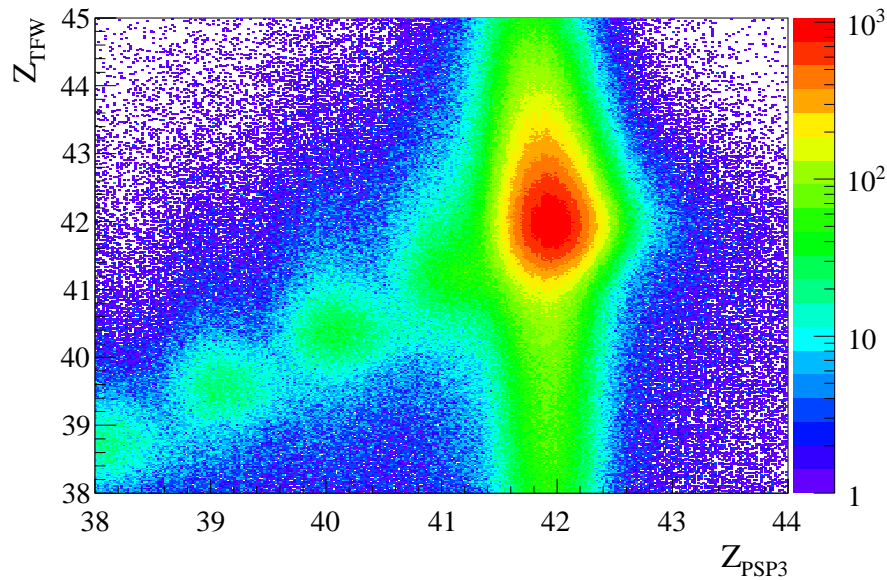
Figure 2.9.: Fragment charge measured by TFW and PSP3. The charge measured with the TFW shows a distribution with a large width at the expected value $Z = 42$. Thus, the fragments with a charge number of $Z = 41$ cannot be clearly separated from the distribution at $Z = 42$.

O. Ershova describes possible reasons for the bad resolution of TFW paddles in her thesis [48]. It is suggested that high rates on the paddles reduce the resolution. Paddle 14 is in the center of the beam spots (Figure 2.5), and was therefore hit by most of the ions. The charge distribution measured with paddle 14 shows the widest spread (Figure 2.7).

Figure 2.10 shows the fragment charge measured with the TFW as a function of event number for a subset of the Pb target data and the ^{94}Mo beam. The beam spills are reflected in the

data. The lengths of the spills are equal, but the spill intensities vary. The higher the spill intensity, the more events are recorded during the spill. The fragment charge measured with the TFW varies during a beam spill. It first increases in charge number, then decreases again, mirroring the spill intensity profile. When the spill intensity is high, the rate on the TFW paddles is high, which results in a large charge detected with the TFW.
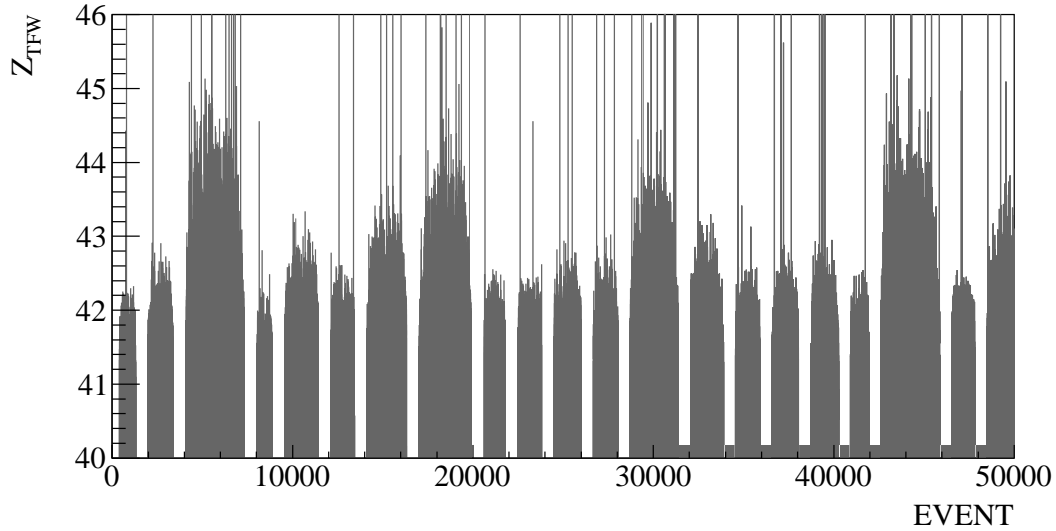
Figure 2.10.: Fragment charge measured by the TFW as a function of event number. The lengths of the spills are equal, but their intensity varies. A subset of 50,000 events of the Pb target data for ^{94}Mo is shown.

Figure 2.11 shows the fragment charge measured with the TFW as a function of number of events N_{E} in the corresponding beam spill. The numbers vary from several hundred events to 5,000 events. The charge distributions are plotted for several intervals of the number of events per spill in Figure 2.12. The mean value and the width of the distribution of the TFW charge increase with the number of events per spill. The mean value of the total distribution matches the charge number $Z = 42$ of molybdenum with the previously determined calibration parameters. The mean charge of the data requiring a number of events per spill of less than 1,000 or between 2,000 and 3,000 are shifted by about $\Delta Z = 0.3$ (charge units).

The total charge distribution is not symmetric. It cannot be fitted with Gaussian distributions to obtain selection criteria on the fragment charge for the data analysis. Also, different charge numbers cannot be resolved. Two approaches are possible to correct for the shift of the mean value of the charge distribution: The calibration parameters could be determined depending on the number of events per spill, or the mean values of the charge distribution as a function of the number of events per spill could be fitted with a linear function and shifted
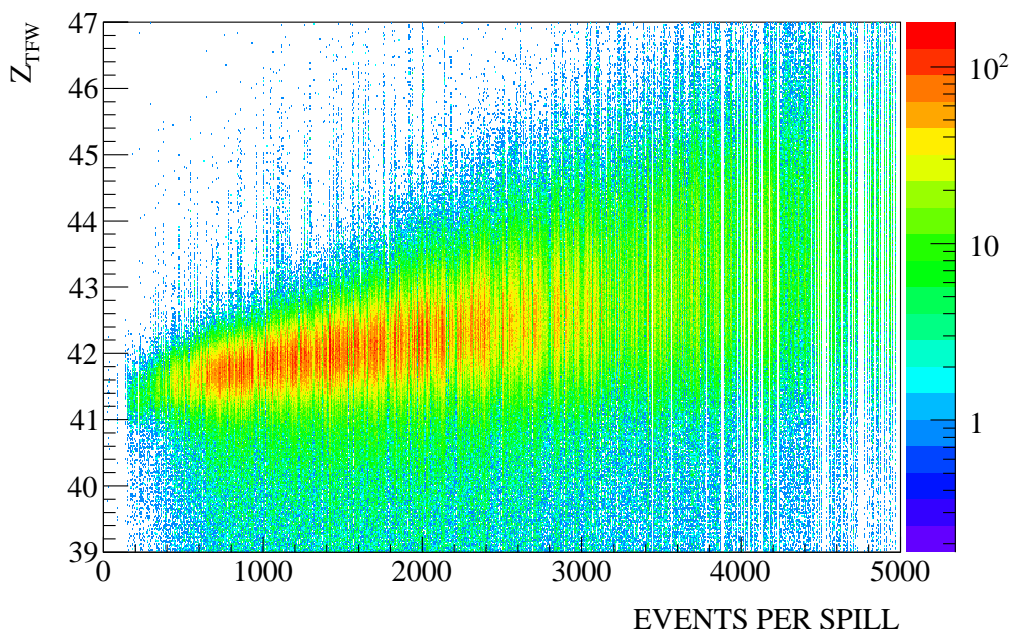
Figure 2.11.: Fragment charge measured by TFW as a function of the number of events per beam spill. With increasing number of events per spill the mean value of the charge distribution is shifted to higher charge numbers and the distribution becomes broader.

to the expected value. However, both approaches do not address the problem of decreasing resolution with increasing number of events per spill.

A possible solution is to apply intensity limits on the data. However, the limits have to be chosen such that sufficient data statistics for the analysis is guaranteed. It can be assumed that the preceding spill does not affect the gain in the current spill since the beam spills are several seconds apart. This holds true for the ^{94}Mo beam experiment under investigation in this work according to Figure 2.10. A symmetric charge distribution is obtained by selecting data with a number of events per spill between 1,000 and 2,000 in the case of the ^{94}Mo beam (Figure 2.12). Figure 2.13 shows the resulting charge distributions for the neutron-dissociation events. While the peak at $Z = 42$ of the Pb target distribution can be fitted with a Gaussian function to obtain the charge selection criterion, the same peak is indistinguishable from events with lower Z for the C and No target distributions. Therefore, the TFW is not used for selecting the fragment charge in the analysis presented here.

Future experiments should check the intensities on single paddles carefully and distribute the ion hits equally between the paddles illuminated by the beam spot.
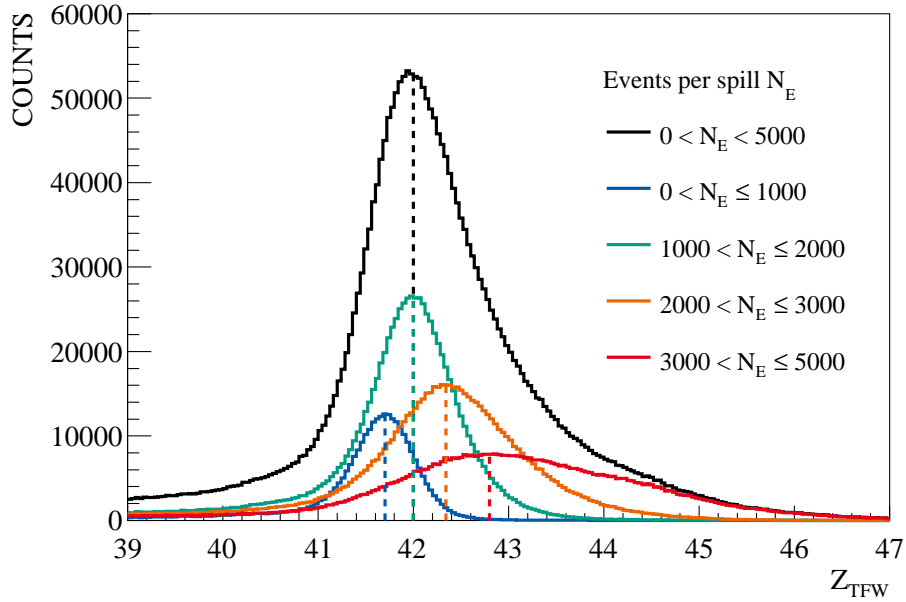
Figure 2.12.: Fragment charge measured by TFW for different beam spill intensities. The black curve represents the total distribution. Spill intensity limits were set on the data for the other distributions.
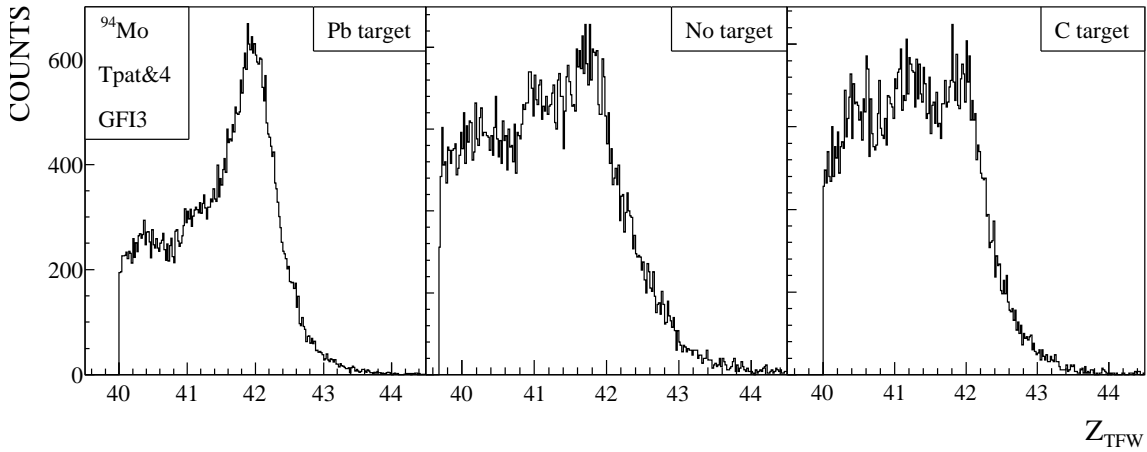
Figure 2.13.: Fragment charge Z reconstructed by the TFW for the measurement with Pb and C target and without target for neutron-dissociation events. The data with numbers of events per spill between 1,000 and 2,000 are chosen. Note that the C and No target distributions are scaled with a factor of two.

2.3   Data analysis

Several steps are needed to extract the cross section from the data of the complex experimental setup. Coulomb dissociation reactions have to be identified, and the background from nuclear reactions and reactions with the experimental setup has to be subtracted.

Table 2.1 lists the data used for the analysis of the Coulomb dissociation reactions of ^{94}Mo and ^{100}Mo. The numbers represent all available data in the case of ^{94}Mo. A subset of the total amount is chosen in the case of ^{100}Mo.

Beam	Beam energy (AMeV)	Target	Thickness (mg cm^{-3})	Number of tracked events	
				Tpat&1	*Tpat*&4
^{94}Mo	500.00	Pb	519	2,783,814	666,787
^{94}Mo	500.00	C	187	1,456,905	398,768
^{94}Mo	500.00	No		1,415,415	266,082
^{100}Mo	497.95	Pb	519	571,618	217,489
^{100}Mo	497.95	C	187	304,822	106,469
^{100}Mo	497.95	No		191,566	70,890

Table 2.1.: Data used for the analysis of the Coulomb dissociation reactions of ^{94}Mo and ^{100}Mo. The beam energies and target properties are listed. The numbers of tracked events for each target with minimum bias trigger (*Tpat*&1) and with neutron trigger (*Tpat*&4) are shown (compare Table 2.2).

2.3.1   Selection of the reaction channel

Identical conditions for pile-up rejection, trigger conditions and fragment and neutron multiplicities were applied for all targets. The ions were tracked through the setup. Conditions were set on the data to identify the Coulomb Dissociaton reactions ^{94}Mo(γ,n)^{93}Mo and ^{100}Mo(γ,n)^{99}Mo, respectively. A primary beam entered the experimental area in both cases. The incoming ion was identified by means of its charge. The reaction fragment was characterized by its charge and mass. Dissociated neutrons were detected by LAND.

2.3.1.1 General conditions on the data

Pile-up rejection

Conditions on the variables *Tnext* and *Tprev* were set in order to suppress pile-up events. The variable *Tnext* contains the time span between the current event and the next time signal of the POS detector. If the time is larger than 10,000 ns, an overflow value is recorded. All events with a POS trigger within the next 10,000 ns were rejected in the analysis (Figure 2.14, left panel).

The variable *Tprev* records the time span between the POS start signal of the current event and the next stop signal. The start signal itself is delayed by about 5,000 ns and serves as the stop signal.

$$t_{\text{prev}} = t_{\text{start}} - t_{\text{stop}}$$
$$t_{\text{stop}} = t_{\text{start}} + t_{\text{delay}}$$

A sharp peak at *Tprev* ≈ 5,680 can be seen in the spectrum (Figure 2.14, right panel). If an ion triggered a signal shortly before the current event, the corresponding delayed start signal stops the current measurement. Thus, the measured time stored in *Tprev* is smaller than the expected value. Only those events with *Tprev* around the expected value were chosen for the analysis.
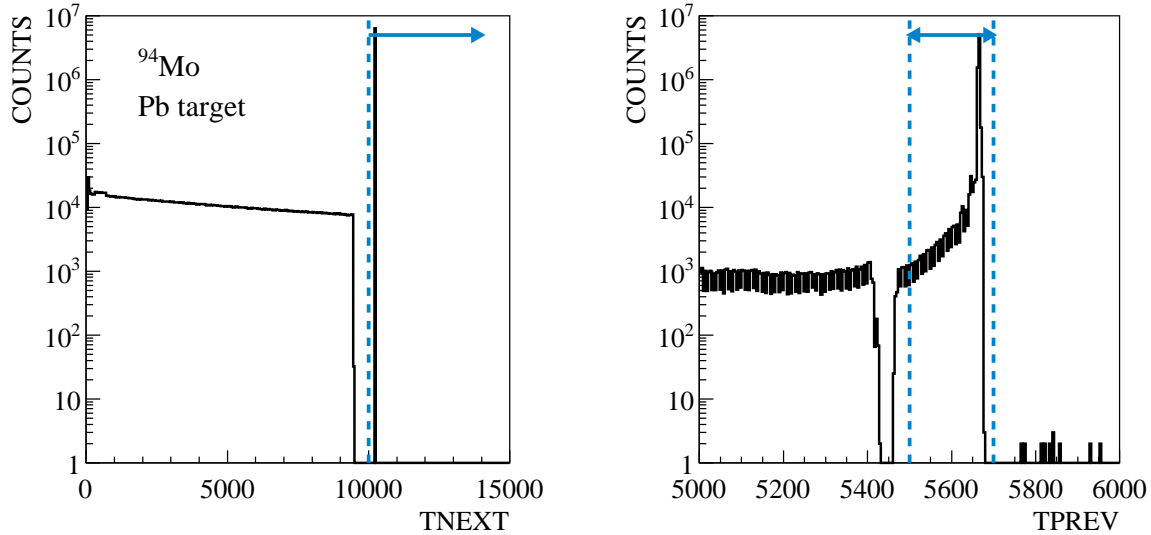
Figure 2.14.: Conditions on the variables *Tnext* and *Tprev* to reject pile-up events for the ^{94}Mo beam on the Pb target.

Trigger conditions

The trigger system decides on whether an event is recorded or discarded depending on the information obtained with the detectors of the setup. The trigger stored in the event data describes the characteristics of the event. The physics trigger settings available in the molybdenum experiment are described in detail in O. Ershova's thesis [48]. Two triggers are used in the analysis presented here (Table 2.2). An incoming ion with a proper trajectory produces a time signal in the POS detector and passes the ROLU detector's window. Due to the large amount of data, the corresponding trigger bit of the variable *Tpat* (*Tpat*&1) is only set for every 32nd minimum bias event (downscale factor 32). If LAND detects one or more particles, the neutron trigger is set (*Tpat*&4).

Tpat	Trigger name	Downscale factor	Description
1	Minimum Bias	32	POS & !ROLU & Spill-on: any incoming ion arriving in the Cave with a proper trajectory
4	Neutron trigger	1	Particle(s) detected by LAND

Table 2.2.: Trigger conditions used in the analysis [48].

Fragment and neutron multiplicities

One fragment is expected in the outgoing channel of unreacted ions, nuclear interactions and neutron-dissociation reactions. Scattered ions in the experimental setup, cosmic particle events, etc. can cause additional signals in the TFW. These events were rejected by setting the fragment multiplicity to one. The neutron multiplicity was chosen according to the reaction channel under investigation.

2.3.1.2   Fragment tracking

The mass of the outgoing fragment has to be determined. Only those events are considered in the analysis presented here, where a fragment mass could be reconstructed.

The fragment mass is obtained by tracking the fragment's trajectory through ALADIN. The magnet bends the ions in horizontal direction. The deflection of the fragment in the magnetic field depends on the ratio of its mass to charge (A/Z). If the fragment charge and the angle of deflection in the magnetic field are known, the mass number A can be determined. The angle

of deflection is calculated by fitting the fragment trajectories upstream and downstream the magnet (Figure 2.15). Upstream the magnet, two track points are defined by the *x*-position at the target, which is provided by the PSP1 and PSP2 detectors, and the *x*-position at PSP3. Downstream the magnet, the *x*-positions of the track points are obtained by GFI1 and either GFI2 or GFI3. The mass number of the fragment is determined iteratively from a given initial value for each event.
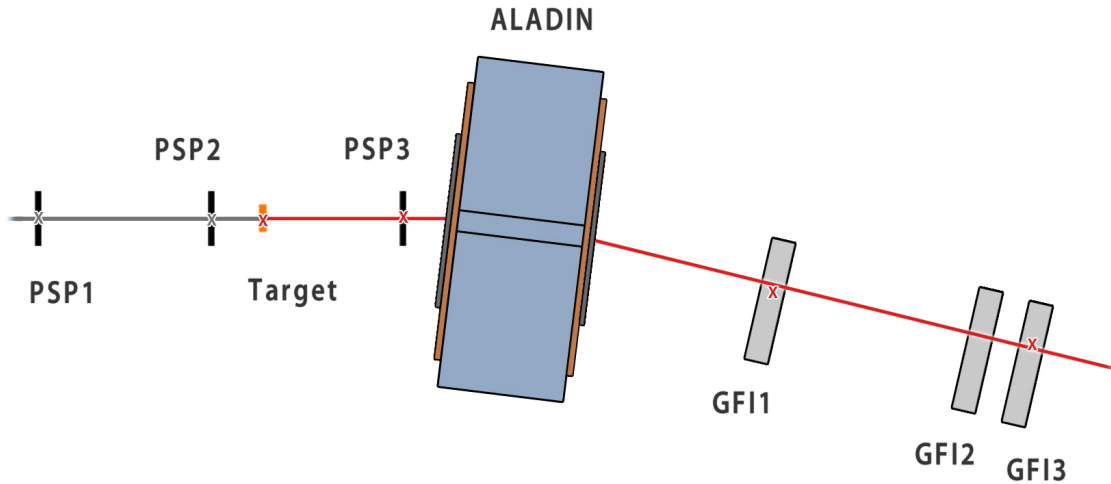
Figure 2.15.: Concept of fragment tracking: The fragment trajectory is determined by two track points in front of and two track points after ALADIN (red crosses). The position at the target is calculated with the data of the PSP1 and PSP2 detectors (gray crosses). The PSP3 detects the position in front of the magnet. GFI1, GFI2 and GFI3 measure the fragment positions behind the magnet.

The tracking algorithm *Tracker* was provided by R. Plag. The software requires input about the detector positions in the laboratory system of Cave C. The values for the molybdenum experiment are given in Table A.1 in the Appendix. Also, several input parameters and preselection criteria are needed, such as the charge and mass numbers and the velocity of the projectile, the charge number of the fragment for the reaction channel under investigation, the fragment multiplicity, the reaction trigger and the neutron multiplicity in the case of the neutron trigger setting. Table A.2 lists all parameters and conditions set on the data for tracking.

The reconstructed fragment mass may depend on the angle δ_{IT} between the trajectory of the incoming ion and the beam axis. Figure 2.16 shows the dependency of the fragment mass on δ_{IT}. The mass obtained from the tracking $M_{\text{IT},0}$ has to be corrected according to

$$M_{\text{IT}} = M_{\text{IT},0} + C_{\text{IT}} \cdot \delta_{\text{IT}}. \tag{2.22}$$

The correction factors C_{IT} were chosen such that the mass resolution is optimal. The factors obtained are listed in Table 2.3. In the following only corrected mass numbers are considered.
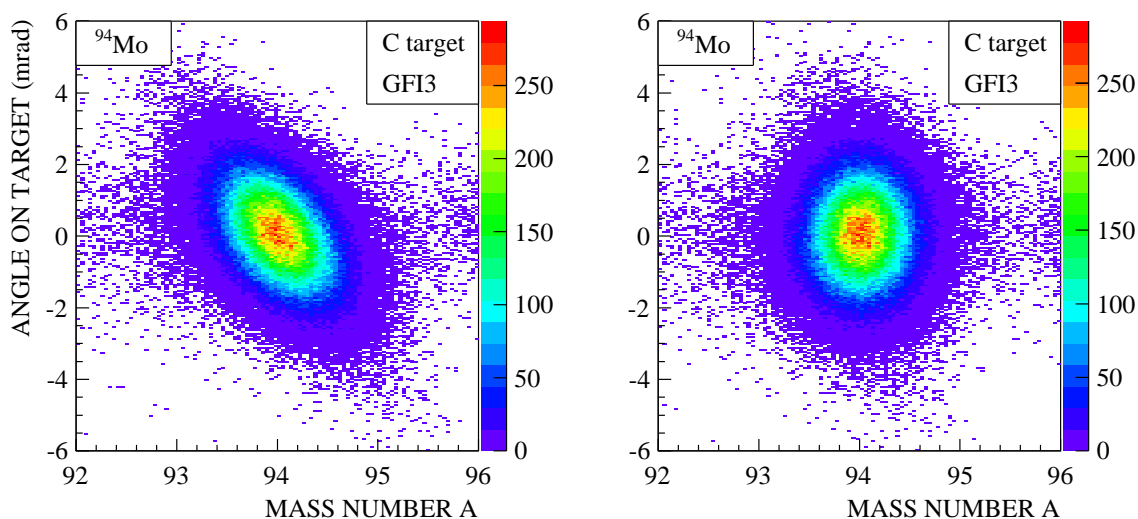
Figure 2.16.: Correction of fragment mass for the angle between the ion trajectory and the beam axis. The measurement with a carbon target data tracked with GFI3 is shown for ^{94}Mo. Left: Fragment mass spectrum without correction. Right: Fragment mass spectrum with correction according to Equation (2.22).

The resulting mass spectrum for the ^{94}Mo beam impinging on the lead target with minimum bias conditions (compare Table 2.2) is shown in Figure 2.17. The spectrum was fitted with a Gaussian function. A mass resolution of $\sigma_{M,GFI3} = 0.34$ (atomic mass units) was obtained. The results for all targets are listed in Table 2.3.

	^{94}Mo			^{100}Mo		
Target	C_{IT}	$\sigma_{M,GFI2}$	$\sigma_{M,GFI3}$	C_{IT}	$\sigma_{M,GFI2}$	$\sigma_{M,GFI3}$
Pb	-33	0.34	0.34	0	0.37	0.37
C	120	0.31	0.31	58	0.32	0.32
No	142	0.29	0.29	48	0.33	0.33

Table 2.3.: Angle correction factors C_{IT} and mass resolutions σ_M (atomic mass units) for all targets for the ^{94}Mo and ^{100}Mo data.
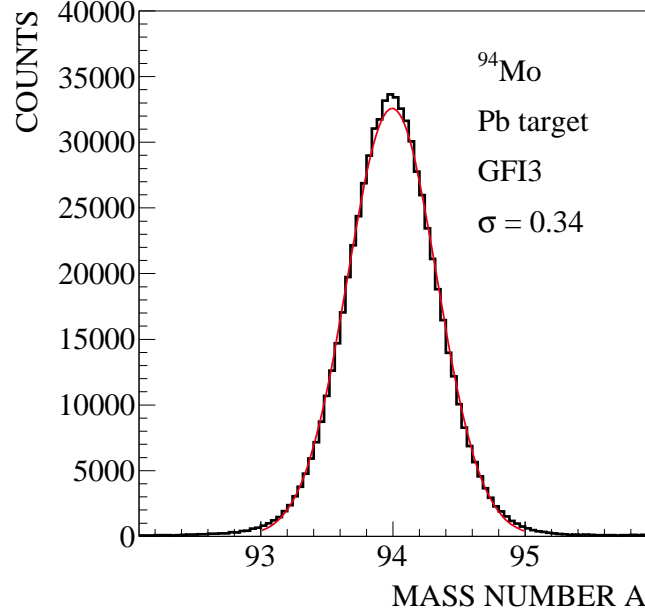
Figure 2.17.: Mass resolution of the unreacted ^{94}Mo beam on the Pb target. The distribution was fitted by a Gaussian function. A resolution of $\sigma_{M,\text{GFI3}} = 0.34$ (atomic mass units) was obtained.

2.3.1.3 Selection of the incoming channel

Primary beams of ^{94}Mo and ^{100}Mo entered the experimental area, respectively. The incoming projectile was identified by means of the charge (Z) measured with PSP1 and PSP2 to reject breakup events in the material in front of the target. The two-dimensional cut was obtained by fitting the one-dimensional distributions of PSP1 and PSP2 with Gaussian distributions (Figure 2.18). The mean values ($\bar{Z}_{\text{PSP1}}$ and $\bar{Z}_{\text{PSP2}}$) and the widths (standard deviations σ_{PSP1} and σ_{PSP2}) define an elliptical cut for the incoming ion with charge Z_0. Different multiples of the widths can be chosen by the integer value n_{In} for systematic studies of the impact of this artificially chosen selection criteria.

$$\left(\frac{\bar{Z}_{\text{PSP1}} - Z_0}{n_{\text{In}} \cdot \sigma_{Z,\text{PSP1}}}\right)^2 - \left(\frac{\bar{Z}_{\text{PSP2}} - Z_0}{n_{\text{In}} \cdot \sigma_{Z,\text{PSP2}}}\right)^2 \leq 1. \tag{2.23}$$

The resulting fit parameters for the ^{94}Mo and ^{100}Mo data are listed in Table 2.4. The uncertainties of the parameters are in the order of 10^{-3} for the width and even less for the mean values of the Gaussian fits. These uncertainties are neglected in the following.
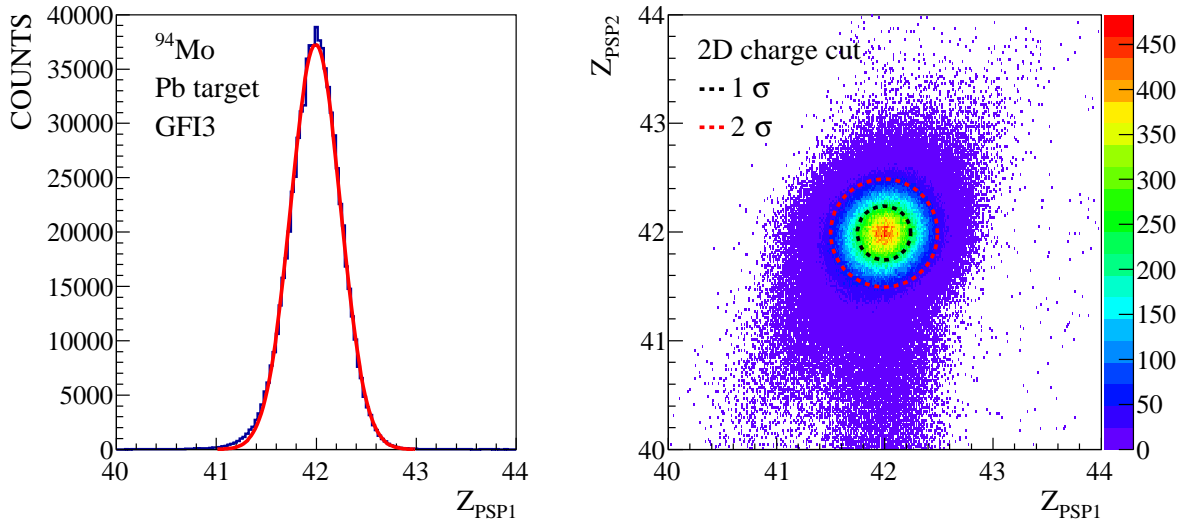
Figure 2.18.: Projectile charge Z measured with the PSP1 and PSP2. Left: One-dimensional Gaussian fit of the PSP1 charge distribution. Right: Resulting two-dimensional cut on the charge distribution.

Beam	Target	$\bar{Z}_{PSP1}$	$\sigma_{Z,PSP1}$	$\bar{Z}_{PSP2}$	$\sigma_{Z,PSP2}$
^{94}Mo	Pb	42.00	0.25	41.99	0.25
	C	42.02	0.26	42.02	0.24
	No	41.99	0.25	42.02	0.25
^{100}Mo	Pb	42.00	0.24	42.00	0.26
	C	42.99	0.24	42.99	0.25
	No	42.00	0.24	42.00	0.26

Table 2.4.: Mean values and width of the Gaussian fits of the incoming charge distributions measured with PSP1 and PSP2 for the ^{94}Mo and ^{100}Mo data.

2.3.1.4 Selection of the outgoing channel

The heavy reaction fragment was identified by means of its charge and mass in the outgoing channel. The fragment charge was selected using PSP3. The fragment mass was determined by tracking of the ions through the magnetic field, using position information provided by the PSP and GFI detectors (compare Section 2.3.1.2). Furthermore, one neutron had to be detected by LAND.

Fragment charge

The fragment charge was measured with the PSP3 behind the target. The data with minimum bias trigger as well as the data with neutron trigger (compare Table 2.2) were fitted by Gaussian functions to determine the charge cuts for the molybdenum isotopes with $Z = 42$ (Figure 2.19).
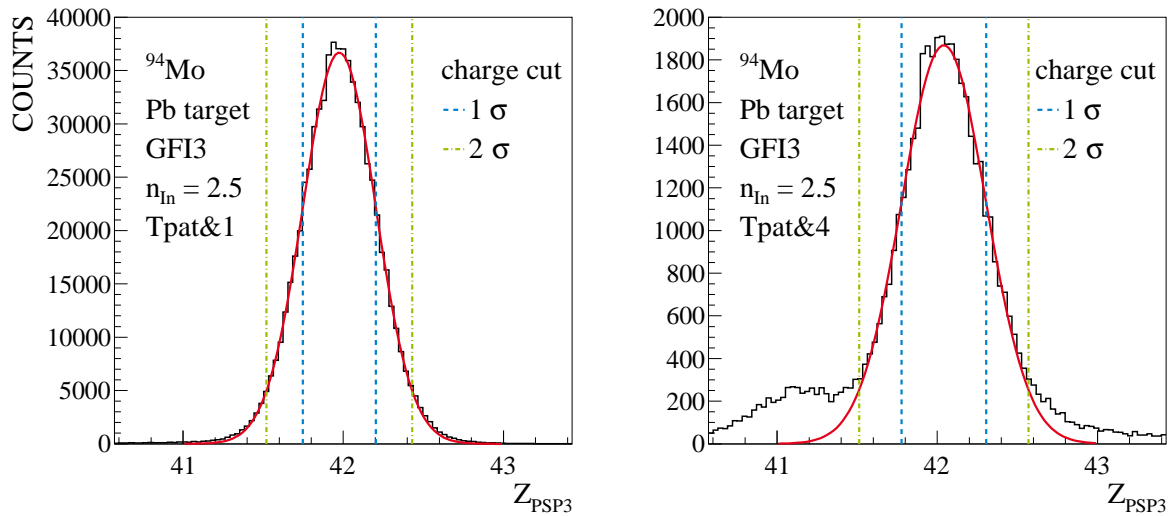
Figure 2.19.: Fragment charge Z measured by the PSP3. Left: Minimum bias data with *Tpat*&1. Right: Neutron trigger data with *Tpat*&4. The distributions were fitted with one-dimensional Gaussian functions to determine the charge cuts.

Table 2.5 shows the mean values and widths of the Gaussian fits of the fragment charge distributions measured with PSP3 for the ^{94}Mo and ^{100}Mo data. The incoming ions were selected with $n_{In} = 2.5$ according to equation 2.23. The uncertainties of the fit parameters are again in the order of 10^{-3} and are neglected in the following.

Beam	Target	$\bar{Z}_{PSP3}$ *Tpat&1*	$\sigma_{Z,PSP3}$	$\bar{Z}_{PSP3}$ *Tpat&4*	$\sigma_{Z,PSP3}$
^{94}Mo	Pb	41.98	0.23	42.04	0.26
	C	41.99	0.23	42.01	0.25
	No	42.00	0.23	42.02	0.25
^{100}Mo	Pb	42.01	0.22	42.03	0.24
	C	42.00	0.22	42.02	0.23
	No	42.00	0.22	42.02	0.23

Table 2.5.: Mean values and widths of the Gaussian fits of the fragment charge distributions measured with PSP3 for the ^{94}Mo and ^{100}Mo data with minimum bias condition (*Tpat&1*) and neutron trigger (*Tpat&4*). The incoming ions were selected with a cut width of $n_{In} = 2.5$ according to Equation (2.23).

Neutron detection

A neutron is expected to hit LAND in the outgoing channel of the Coulomb dissociation reaction ^{94}Mo(γ,n). The neutron trigger *Tpat&4* is therefore required for a good event. The hit multiplicity, the positions of the hits and the times of flight are recorded. The neutron velocity is calculated from the time of flight and the flight path to the detector.

The GFI2 and GFI3 detectors and the TFW were located close to LAND at an angle of about 13° to the beam axis (compare Figure 2.4). Scattered ions from these detectors may hit LAND. These events show a characteristic signature with hit positions at large negative x-values and small velocities. Figure 2.20 (left plot) shows the LAND hit positions for the ^{94}Mo beam on the Pb target. Events from scattered ions can be clearly seen on the left side of the distribution. The corresponding neutron velocity spectrum is displayed in Figure 2.21. It shows a main peak at about 22.6 cm ns^{-1} and a long tail to small velocities. A condition on the charge ($Z_{TFW} \geq 40$) detected by the Time-of-Flight Wall (TFW) reduces the background considerably and was therefore used in the further analysis. The main peak was fitted with a Gaussian distribution. Due to the large background at velocities smaller than 22 cm ns^{-1} only those events with velocities higher than the mean velocity were selected. Figure 2.20 (right plot) shows the resulting hit distribution, which shows a clear pattern of the neutron beam spot in LAND. Since half of the neutron events with a proper velocity are rejected by the selection criteria, the recorded events were scaled with a factor of two.
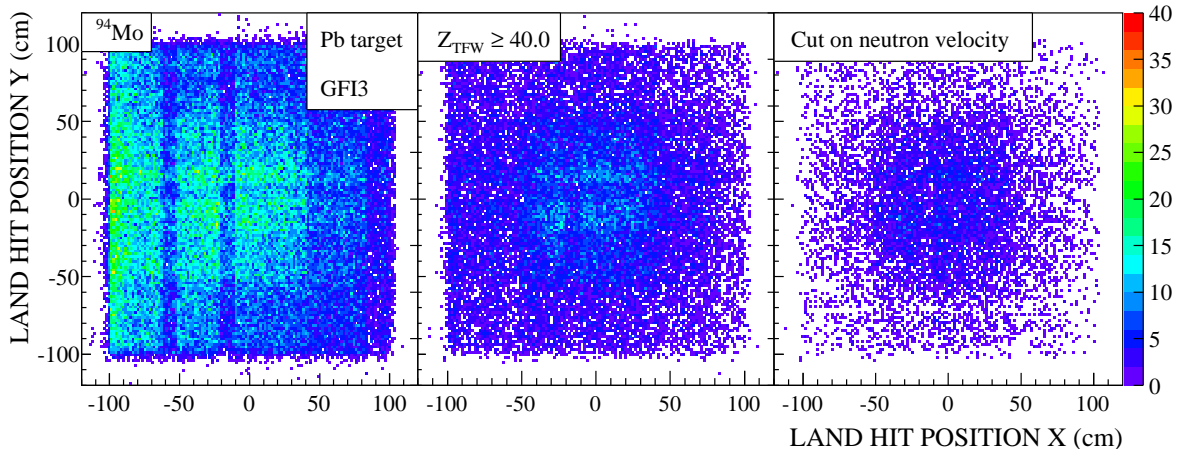
Figure 2.20.: LAND hit positions for the ^{94}Mo beam on Pb target. The incoming and outgoing charges were selected with $n_{In} = 2.5$ and $n_{Out} = 1.5$. Left: Events from scattered ions in the setup can be seen for large negative x-values. Center: The condition $Z_{TFW} \geq 40.0$ reduces the background considerably. Right: A distribution reflecting the beam spot at the center of LAND was obtained with the cut on the neutron velocity (compare Figure 2.21).
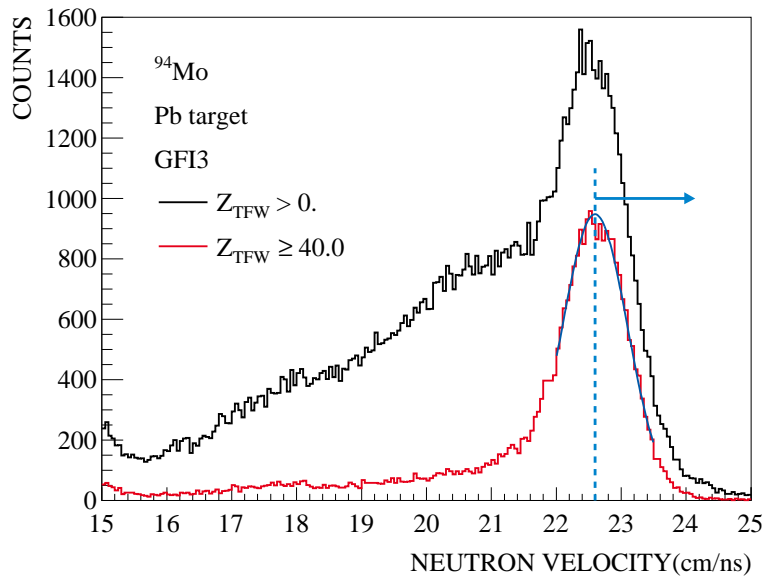
Figure 2.21.: Neutron velocity distribution for the ^{94}Mo beam on Pb target. The incoming and outgoing charges were selected with $n_{In} = 2.5$ and $n_{Out} = 1.5$ (black curve). A condition on the charge detected by the Time-of-Flight Wall (TFW) reduces the background considerably (red curve). The distribution was fitted with a Gaussian function to obtain the selection criterion for the neutron velocity.

2.3.2 LAND efficiency correction

The selected data need to be corrected for the LAND efficiency and acceptance. The kinetic energy of the neutron in the center-of-mass frame of the incoming particle was calculated and the entry in the fragment-mass spectrum was weighted with the corresponding value of the LAND efficiency and acceptance for each event (Figure 2.8). The determination of the neutron kinetic energy relies on the kinematic complete reconstruction of the event. The calculation of the energy applies the concept of invariant mass. The mass of the projectile m_{proj} is considered in the projectile rest frame in the incoming channel:

$$M_{\text{inv}}^{\text{In}} = m_{\text{Proj}}.$$

In the outgoing channel, the four-momentum vector is calculated from the energies E_i and momenta $\vec{p}_i$ of the fragment and the neutron in the laboratory reference frame:

$$M_{\text{inv}}^{\text{Out}} = \sqrt{\left(\sum_{i=1}^{N} E_i\right)^2 - \left(\sum_{i=1}^{N} \vec{p}_i\right)^2}.$$

Energy and momentum are defined as following:

$$\left(\sum_{i=1}^{N} E_i\right)^2 = \sum_i (\gamma_i m_i)^2 + \sum_{i \neq j} \gamma_i \gamma_j m_i m_j,$$

$$\left(\sum_{i=1}^{N} \vec{p}_i\right)^2 = \sum_i (\beta_i \gamma_i m_i)^2 + \sum_{i \neq j} \beta_i \beta_j \gamma_i \gamma_j m_i m_j \cos \vartheta_{ij},$$

where β is the velocity and m the rest mass of the fragment or the neutron, $\gamma = (1 - \beta^2)^{-\frac{1}{2}}$ is the Lorentz factor and ϑ_{ij} is the angle between the particles i and j. The kinetic energy of the neutron can be calculated under conservation of the invariant mass and by finally subtracting the Q value of the reaction:

$$E_{\text{kin}}^{\text{n}} = \sqrt{\sum_i m_i^2 + \sum_{i \neq j} \gamma_i \gamma_j m_i m_j (1 - \beta_i \beta_j \cos \vartheta_{ij})} - m_{\text{Proj}} - Q. \qquad (2.24)$$

The one-neutron-dissociation reaction of ^{94}Mo was analyzed in this work. The neutron kinetic energies were calculated with Equation (2.25):

$$
\begin{aligned}
E_{\mathrm{kin}}^{\mathrm{n}} = \Big[& m_{^{93}\mathrm{Mo}}^{2} + m_{\mathrm{n}}^{2} \\
& + (2 \cdot \gamma_{^{93}\mathrm{Mo}} \gamma_{\mathrm{n}} m_{^{93}\mathrm{Mo}} m_{\mathrm{n}} \cdot (1 - \beta_{^{93}\mathrm{Mo}} \beta_{\mathrm{n}} \cos \vartheta_{^{93}\mathrm{Mo,n}})) \Big]^{\frac{1}{2}} \\
& - m_{^{94}\mathrm{Mo}} - Q_{n,^{94}\mathrm{Mo}}
\end{aligned}
\tag{2.25}
$$

2.3.3   Reaction probability

The reaction probability is the ratio of the number of events in the reaction channel under investigation and the number of incoming ions. The total number of incoming ions was obtained by applying all conditions (Table A.2) on the tracked data and selecting the minimum bias reactions (compare Table 2.2) for each target.

By using the same selection criteria as for the Coulomb dissociation reactions for the incoming and the outgoing ions corrections for cut efficiencies are not necessary. (A detailed discussion of possible efficiency issues is given in Section 6.3 of O. Ershova's thesis [48].) This conclusion requires several assumptions and puts constraints on the analysis:

- The same detectors are used to measure the reacted and unreacted ions.

- The intrinsic efficiencies of the detectors and their geometrical acceptance are the same for the reacted and unreacted ions.

- The fractions of ions interacting with the experimental setup after passing the target are the same for the reacted and unreacted ions.

- The efficiency of the tracking algorithm is the same for the reacted and unreacted ions.

The molybdenum experiment fulfilled these assumptions since the size of the beam was small compared to the detectors, and the differences in mass and kinetic energy between the reacted and unreacted ions are negligible.

Figures 2.22 and 2.23 show the reaction probabilities of the ^{94}Mo and ^{100}Mo beam on the Pb and C targets and without target, respectively. The spectrum obtained from the measurement without target was scaled by a factor of 0.9 for the ^{100}Mo data. The resulting distribution shows the same peak content as the Pb target distribution at mass number $A = 100$. Events with a reconstructed mass number of the incoming ion represent events without a reaction in the target and must be reproduced by the measurement without target. Thus, the influence of the setup on the beam is determined.
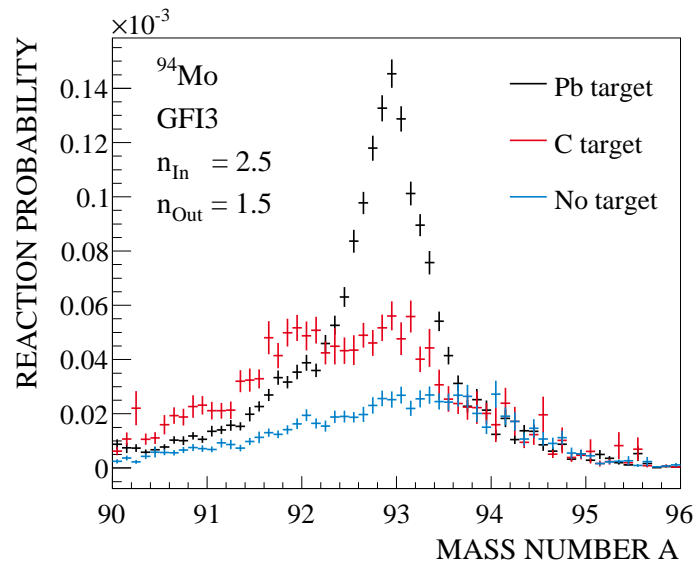
Figure 2.22.: Reaction probabilities of the ^{94}Mo beam on the Pb and C targets and without target. The reaction channel ^{94}Mo$(\gamma,$n$)^{93}$Mo was selected by the conditions described in the previous sections.
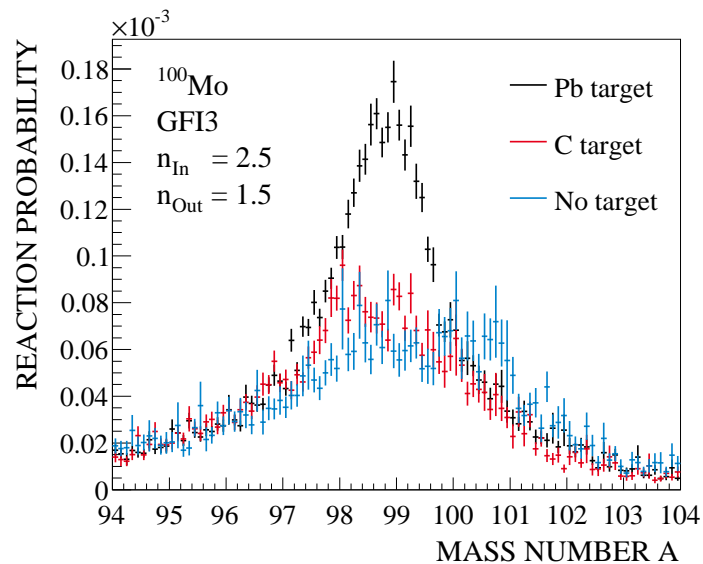
Figure 2.23.: Reaction probabilities of the ^{100}Mo beam on the Pb and C targets and without target. The reaction channel ^{100}Mo$(\gamma,$n$)^{99}$Mo was selected by the conditions described in the previous sections. The "no target" spectrum was scaled with a factor of 0.9 to reproduce the distribution of the Pb target measurement at $A = 100$ (unreacted beam).

2.3.4 Background subtraction

In addition to Coulomb excitation, the projectile may experience nuclear interactions in the target and reactions with the material outside of the target. Two additional measurements were performed in order to determine these background contributions: one without target and one with a carbon target. The induced electromagnetic excitations are much weaker compared to lead because of the lower atomic number of carbon. The Coulomb dissociation cross section scales with Z^2. The cross section of peripheral nuclear interactions is related to the size (radii) of the projectile and of the target nuclei. While the Coulomb dissociation cross section is reduced by a factor of about 200 for the carbon target compared to the lead target, the likelihood of a peripheral nuclear reaction is only reduced by a factor of about 2.5. Therefore, the interaction of the projectile with the carbon target is considered to be purely nuclear [75]. The background distributions are normalized and subtracted from the lead target distributions. The Coulomb dissociation cross section σ_{CD} is determined by

$$\sigma_{CD} = \left(\frac{M_{Pb}}{d_{Pb}N_A}\right)p_{Pb} - \left(\alpha \cdot \frac{M_C}{d_C N_A}\right)p_C - \left(\frac{M_{Pb}}{d_{Pb}N_A} - \alpha \cdot \frac{M_C}{d_C N_A}\right)p_{No}, \qquad (2.26)$$

where p is the interaction probability, M the molar mass of the target material [g mol^{-1}], d the target thickness, N_A the Avogadro number [mol^{-1}] and α the nuclear scaling factor. The indices refer to the different targets. In the analysis presented here, α was calculated according to the "black disc model" [76], in which the interacting nuclei are considered fully opaque to each other:

$$\alpha = \frac{A_P^{\frac{1}{3}} + A_{Pb}^{\frac{1}{3}}}{A_P^{\frac{1}{3}} + A_C^{\frac{1}{3}}}. \qquad (2.27)$$

Here, A_P, A_{Pb}, and A_C represent the mass numbers of the projectile, the lead and the carbon target. The model yields $\alpha = 1.53$ for the ^{94}Mo and $\alpha = 1.52$ for the ^{100}Mo projectile.

2.3.5 Calculation of the integral cross section

The integral Coulomb dissociation cross section was calculated from the fragment mass spectrum. The data were selected according to the criteria described in the previous sections. The entries in the mass spectrum were weighted with the LAND efficiency and acceptance on an event-by-event basis. The reaction probability was calculated for the measurements with Pb and C target and without target (Section 2.3.3), and the background was subtracted according to Equation (2.26).

Figure 2.24 shows the resulting mass spectrum for the Coulomb dissociation reaction of ^{94}Mo, ^{nat}Pb(^{94}Mo,^{93}Mo+n)^{nat}Pb. The integral Coulomb dissociation cross section was calculated as the integral from mass number $A = 92$ to $A = 94$, which includes a range of $3\sigma_M$ around the fragment's mass number $A = 93$ according to Table 2.3.

Figure 2.25 shows the fragment mass spectrum for the reaction ^{nat}Pb(^{100}Mo,^{99}Mo+n)^{nat}Pb. A clear peak at the expected mass number $A = 99$ can be seen, but also entries with mass number $A = 98$ are present. The spectrum was described by a fit of two Gaussian functions with the same widths for ^{99}Mo and ^{98}Mo. The cross section was calculated as the integral of the fit of ^{99}Mo.

The peak at mass number $A = 98$ results from events where two neutrons emitted by the nucleus ^{100}Mo were reconstructed as one neutron by the LAND shower algorithm. The two-neutron-separation channel is not visible in the data for ^{94}Mo in agreement with the high separation energy above the adiabatic cutoff energy (Equation (2.5)).
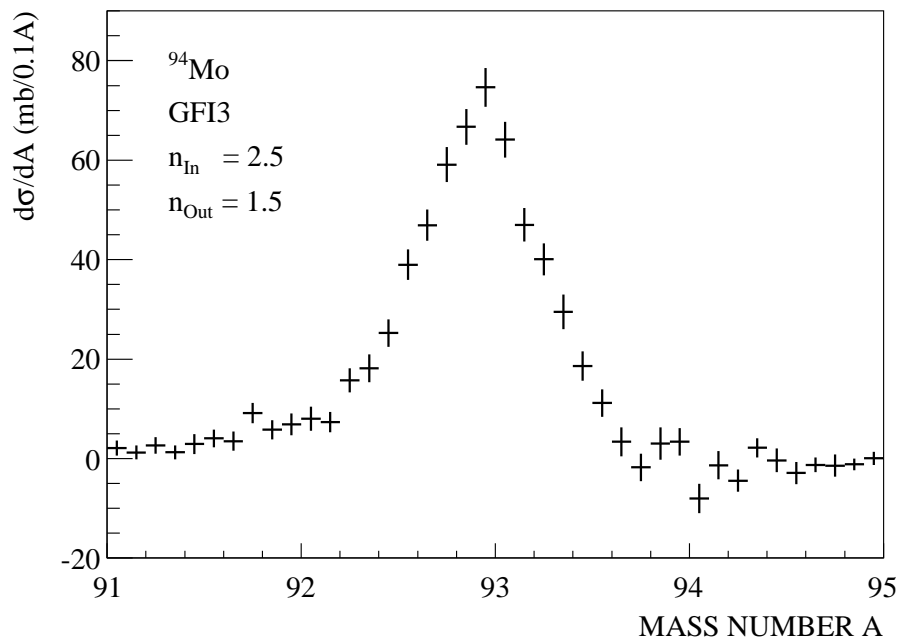
Figure 2.24.: Determination of the integral Coulomb dissociation cross section of the reaction ^{94}Mo(γ,n). The mass spectrum was integrated from mass number $A = 92$ to $A = 94$, which includes a range of $3\sigma_M$ around the fragment's mass number $A = 93$ according to Table 2.3.
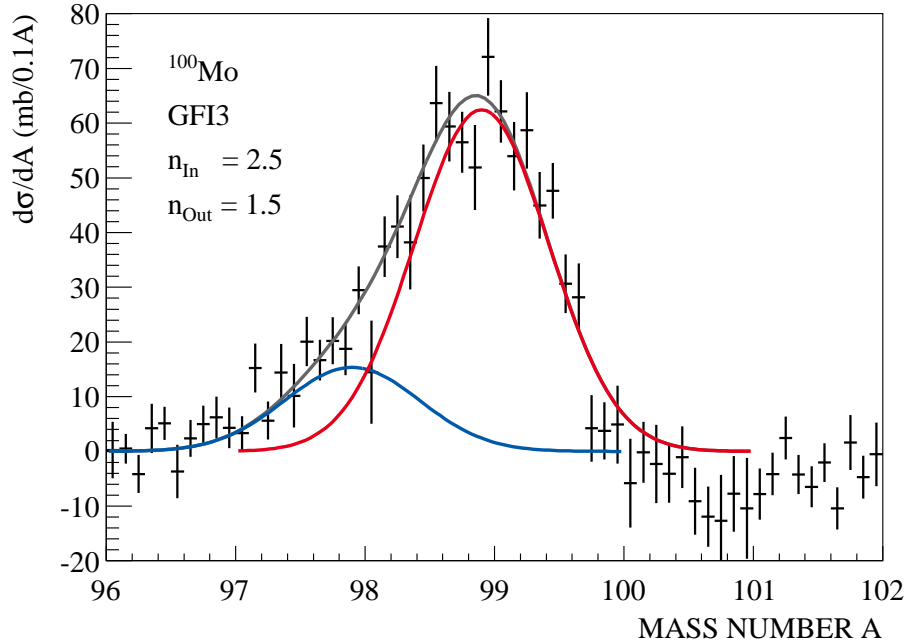
Figure 2.25.: Determination of the integral Coulomb dissociation cross section of the reaction ^{100}Mo(γ,n). The mass spectrum was fitted by the sum of two Gaussian functions with the same widths for ^{99}Mo and ^{98}Mo. The cross section was calculated as the integral over the entire mass range of the fit of ^{99}Mo.

2.3.6 Systematic uncertainties

The systematic uncertainties of the integral Coulomb dissociation cross sections stem from the reconstruction of the LAND neutron multiplicity (Section 2.2.4), the selection criteria set on the data and the choice of GFI2 or GFI3 for fragment tracking. The uncertainty was estimated by calculating the integral Coulomb dissociation cross sections for all possible combinations of the selection criteria.

Both the incoming and the outgoing charge cuts were selected to ensure high data statistics on the one hand and to maximize the signal-to-background ratio by rejecting events with lower Z from breakup events on the other hand. Optimal cut widths of $n_{In} = 2.5$ (Equation (2.23)) and $n_{Out} = 1.5$ (Figure 2.19) could be found for the incoming and outgoing charge cut. The widths were varied by ± 0.5 to estimate the systematic uncertainty.

At the same time, either the data tracked with GFI2 or with GFI3 were chosen for the analysis. The fiber detectors showed the same mass resolution (Table 2.3), hence, GFI3 was chosen, which is expected to provide data with reduced uncertainty of the trajectory's angle because of its larger distance to GFI1 (Figure 2.15).

2.4 Results

2.4.1 The case of ^{94}Mo(γ,n)

Figure 2.26 shows the integral cross sections for all combinations of selection criteria of the Coulomb dissociation reaction ^{nat}Pb(^{94}Mo,^{93}Mo+n)^{nat}Pb. The result for the incoming cut with n_{In} = 2.5 and the outgoing cut with n_{Out} = 1.5 was chosen as the integral cross section for the data set with GFI3 (compare Section 2.3.6). An integral Coulomb dissociation cross section of $(571 \pm 14_{stat})$ mb was obtained. The systematic uncertainty due to the charge cut variations was determined as a symmetrical band around the chosen value including all data points. The data points yield a systematic uncertainty of 1.4%. The small differences in the results using GFI2 or GFI3 as the last tracking detector give a systematic uncertainty of 0.4%. These uncertainties are small compared to the uncertainty of 8% resulting from the LAND shower algorithm. The results, the statistical uncertainty as well as the systematic uncertainties are summarized in Table 2.6.

2.4.2 The case of ^{100}Mo(γ,n)

The same analysis was applied on the ^{100}Mo data as on the ^{94}Mo data. Figure 2.27 shows the integral Coulomb dissociation cross sections for all combinations of selection criteria of the reaction ^{nat}Pb(^{100}Mo,^{99}Mo+n)^{nat}Pb. The results give an integral Coulomb dissociation cross section of $(815 \pm 37_{stat})$ mb. This value is in agreement with the result of $(799 \pm 17_{stat})$ mb obtained by O. Ershova [48]. Table 2.6 lists the systematic uncertainties determined in the analysis of ^{100}Mo.
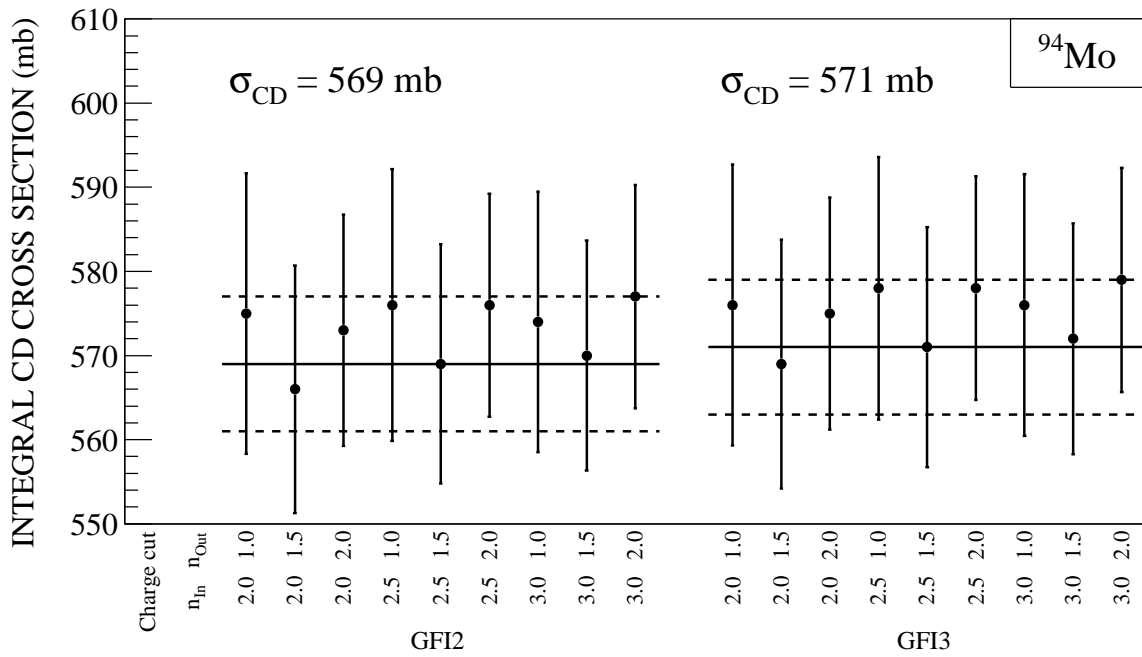
Figure 2.26.: Integral Coulomb dissociation cross section of the reaction ^{94}Mo$(\gamma,n)^{93}$Mo and determination of the systematic uncertainty due to data selection criteria. The following parameters were varied: fragment tracking with GFI2 or GFI3, charge cut on the incoming ions ^{94}Mo and charge cut on the outgoing fragments ^{93}Mo. The error bars show the statistical uncertainties. The result for the incoming cut with $n_{\mathrm{In}} = 2.5$ according to Equation (2.23) and the outgoing cut with $1.5 \cdot \sigma_{Z,\mathrm{PSP3}}$ was chosen as the integral cross section for the data sets with GFI2 and GFI3, respectively. The dashed lines define the systematic uncertainty due to the variation of the selection criteria.
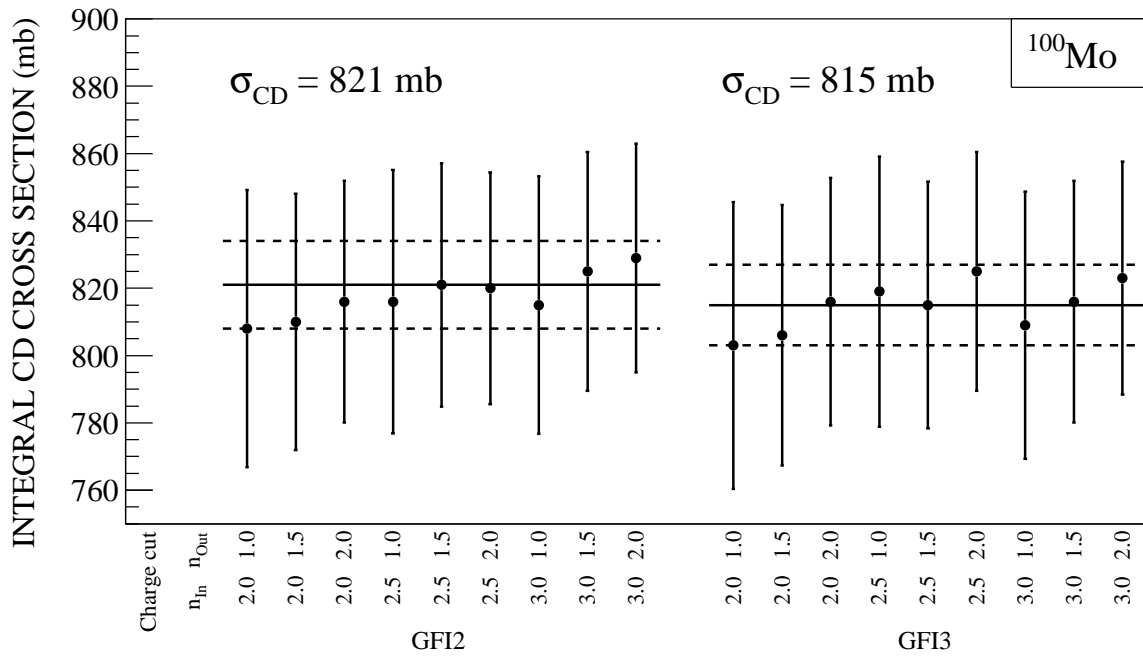
Figure 2.27.: Integral Coulomb dissociation cross section of the reaction ^{100}Mo$(\gamma,n)^{99}$Mo and determination of the systematic uncertainty due to data selection criteria. The following parameters were varied: fragment tracking with GFI2 or GFI3, charge cut on the incoming ions ^{100}Mo and charge cut on the outgoing fragments ^{99}Mo. The error bars show the statistical uncertainties. The result for the incoming cut with $n_{\text{In}} = 2.5$ according to Equation (2.23) and the outgoing cut with $1.5 \cdot \sigma_{Z,\text{PSP3}}$ was chosen as the integral cross section for the data sets with GFI2 and GFI3, respectively. The dashed lines define the systematic uncertainty due to the variation of the selection criteria.

	^{94}Mo(γ,n)	^{100}Mo(γ,n)
σ_{CD} (mb)	571	815
Δ_{stat} (%)	2.5	4.5
Δ_{syst}(LAND) (%)	8.0	8.0
Δ_{syst}(Data selection criteria) (%)	1.4	1.5
Δ_{syst}(GFI2/GFI3) (%)	0.4	0.7
Δ_{syst}(total) (%)	8.1	8.2

Table 2.6.: Integral Coulomb dissociations, statistical and systematic uncertainties of the reactions ^{94}Mo(γ,n) and ^{100}Mo(γ,n). The total systematic uncertainty is composed of the systematic uncertainties of the LAND efficiency and acceptance, the variation of the data selection criteria and the selection of GFI2 or GFI3 for the analysis using Gaussian error propagation.

2.4.3   Comparison with real photon experiments

Photoneutron cross sections of even Mo isotopes were measured by Beil et al. at the 60 MeV linear accelerator at Saclay [49]. The samples were irradiated with a "quasi-monochromatic" continuously variable photon beam with energies up to 30 MeV produced by the in-flight-annihilation of monochromatic positrons. A 500-liter tank filled with a gadolinium-loaded liquid scintillator was used for the detection of neutrons. The detector covered almost the entire solid angle and had a neutron detection efficiency of 60% [77].The inclusive photoabsorption cross section σ_{incl} of the one-neutron removal channel could be obtained by measuring the neutron multiplicity:

$$\sigma_{incl}(\gamma,n) = \sigma\left[(\gamma,n) + (\gamma,pn)\right].$$ (2.28)

The (γ,n) data measured at the LAND setup was compared to the measurements by Beil et al.

The photoabsorption data from Beil et al. [49] was converted into a Coulomb dissociation cross section according to Equation (2.1). The electric dipole and quadrupole components of the virtual photon field are the relevant multipolarities that have to be considered (Figure 2.2). The photoabsorption cross section is mainly represented by the electric dipole component. Although the real photon spectrum contains all multipolarities with the same weight, the probability of a dipole transition is much larger than the probability of a quadrupole transition. However, the electric quadrupole component becomes relevant for the Coulomb dissociation cross section [48].

The photoabsorption data can be considered to be the sum of E1 and E2 components. The E2 component was parametrized according to the systematics of giant resonances and later subtracted from the photoabsorption data to obtain the E1 component. The E2 component consists of an isoscalar (IS, protons and neutrons oscillate in phase) and an isovector part (IV, protons and neutrons oscillate against each other) [78]. Both parts were modelled by a Breit-Wigner distribution [79]

$$\sigma(E) = \frac{\sigma_\mathrm{m}}{1 + \frac{(E^2 - E_\mathrm{m}^2)^2}{E^2 \Gamma^2}}, \tag{2.29}$$

where E_m denotes the peak energy, Γ the width of the peak and σ_m the cross section at the peak energy:

$$\int_0^\infty \sigma(E)dE = \frac{\pi}{2}\sigma_\mathrm{m}\Gamma. \tag{2.30}$$

The parameters were calculated according to [78]:

$$E_\mathrm{m}^\mathrm{IS} = 64 \cdot A^{-\frac{1}{3}} \approx 14.1 \ \mathrm{MeV},$$

$$\Gamma^\mathrm{IS} = 16 \cdot A^{-\frac{1}{3}} \approx 3.5 \ \mathrm{MeV},$$

$$E_\mathrm{m}^\mathrm{IV} = 127 \cdot A^{-\frac{1}{3}} \approx 27.9 \ \mathrm{MeV}.$$

The width of the isovector component was calculated from parametrizations of the width Γ [80] and the peak energy E_x [81]

$$\Gamma = 2.3 + 14 \cdot A^{-\frac{2}{3}} + 21 \cdot A^{-\frac{1}{2}},$$

$$E_x = 31.2 \cdot A^{-\frac{1}{3}} + 20.6 \cdot A^{-\frac{1}{6}}$$

with the known peak energy E_m^IV

$$\Gamma^\mathrm{IV} = \Gamma \frac{E_\mathrm{m}^\mathrm{IV}}{E_x} \approx 8.7 \ \mathrm{MeV}.$$

The energy-weighted sum rule gives the total E2 component of the photoabsorption cross section [82]

$$S = \int \frac{\sigma_\gamma^\mathrm{E2}(E)}{E^2} dE = \frac{\pi^2}{3} \frac{e^2}{\hbar c} \frac{Z\langle r^2 \rangle}{mc^2} \frac{\mathrm{fm}^2}{\mathrm{MeV}}, \tag{2.31}$$

with $e^2/\hbar c = 1/137$, the atomic number Z, the nucleon mass m and the mean square charge radius of the nucleus $\langle r^2 \rangle$:

$$\langle r^2 \rangle = \frac{3}{5}r_0^2 A^{\frac{2}{3}}, \ r_0 = 1.2 \ \mathrm{fm}.$$

S is composed of the isoscalar and isovector parts:

$$S = S(\text{IS}) + S(\text{IV}) = S \cdot \frac{Z}{A} + S \cdot \frac{A - Z}{A}.$$

The sum rule fraction exhausted by the isoscalar component $S(\text{IS})$ is 74.7% for ^{94}Mo according to Moalem et al. [83].

The cross section at the peak energy was obtained by combining Equations (2.30) and (2.31). The E2 component of the photoabsorption cross section was calculated with Equation (2.29). The E1 component resulted from subtracting the E2 component from the total photoabsorption cross section neglecting contributions by M1. The differential Coulomb dissociation cross section was obtained by convoluting the E1 and E2 cross sections with the corresponding virtual photon spectrum (Equations (2.2) and (2.3)).

Figure 2.28 shows the resulting Coulomb dissociation cross section derived from the data of Beil et al. for the reaction ^{94}Mo(γ,n). An integral cross section of (909 ± 55) mb was obtained. The systematic uncertainties of the data measured at Saclay are about 6% [49]. The ratio between the results obtained in this work and the results by Beil et al. was calculated as 0.63 ± 0.07. The relative uncertainties of the cross sections were added quadratically to obtain the uncertainty of the ratio.
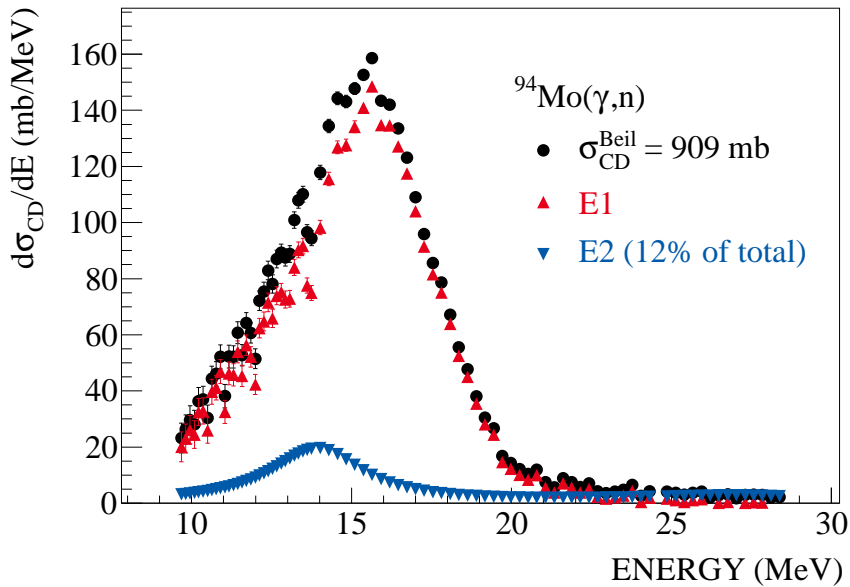
Figure 2.28.: Coulomb dissociation cross section of the reaction ^{94}Mo(γ,n) derived from the data of Beil et al. [49] by convolution with the virtual photon spectra shown in Figure 2.2.

O. Ershova analyzed the Coulomb dissociation of ^{100}Mo and ^{92}Mo in her thesis [48]. The ratio between her result and the integral value obtained from the convolution of the ^{100}Mo data from Beil et al. is $\sigma_{CD}^{Ershova}/\sigma_{CD}^{Beil} = 0.80 \pm 0.10$. To compare the results obtained for ^{92}Mo, the corresponding data from Beil et al. were converted into a Coulomb dissociation cross section as in the case of ^{94}Mo (Figure 2.29). The integral value and the ratio was calculated at (629 ± 38) mb and $\sigma_{CD}^{Ershova}/\sigma_{CD}^{Beil} = 0.59 \pm 0.08$, respectively. Table 2.7 gives an overview of the measured cross sections and the calculated ratios.

Reaction	σ_{CD}^{LAND} (mb)	σ_{CD}^{Beil} (mb)	$\sigma_{CD}^{LAND}/\sigma_{CD}^{Beil}$
^{100}Mo(γ,n)	799 ± 82^{b}	997 ± 61^{b}	0.80 ± 0.10
^{94}Mo(γ,n)	571 ± 48^{a}	909 ± 55^{a}	0.63 ± 0.07
^{92}Mo(γ,n)	369 ± 48^{b}	629 ± 38^{a}	0.59 ± 0.08

Table 2.7.: Comparison of the integral Coulomb dissociation cross sections on ^{100}Mo, ^{94}Mo and ^{92}Mo measured at the LAND setup and analyzed in this work[a] and by O. Ershova[b] [48] to the results published by Beil et al. [49].
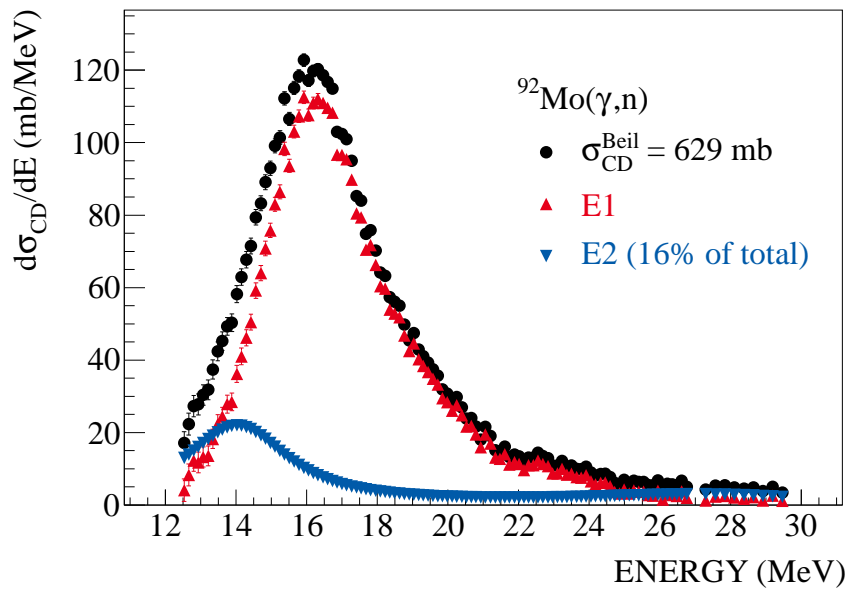
Figure 2.29.: Coulomb dissociation cross section of the reaction ^{92}Mo(γ,n) derived from the data of Beil et al. [49].

Remeasurements of photoabsorption cross sections previously determined at the facility in Saclay showed discrepancies. Berman et al. therefore proposed normalization factors of 0.8 to 0.88 for photoabsorption cross sections measured at Saclay in the mass range of $A = 85$-93 [84]. It was speculated that the differences might stem from wrong estimations of the photon flux or the neutron detection efficiency in the Saclay data. Other measurements confirmed the proposed normalization factors and, e.g., found a ratio of 0.89 ± 0.09 for the reaction ^{100}Mo$(\gamma,$n$)$ [85].

The ratios calculated for the proton-rich isotopes ^{94}Mo and ^{92}Mo are lower than the expected ratios of 0.80 to 0.89 by Berman et al. [84] and Erhard et al. [85]. The data of the molybdenum isotopes show a systematically increasing ratio with increasing neutron numbers of the nuclei with about 0.6 for the p-isotopes ^{92}Mo and ^{94}Mo to 0.8 for the neutron-rich isotope ^{100}Mo (Table 2.7). The deviations will be investigated in the future.

The possible contribution of the $(\gamma,$pn$)$ reaction channel should be studied (compare Equation 2.28). Compared to the neutron-rich isotope ^{100}Mo, a significant contribution to the photodissociation reactions on the proton-rich isotopes ^{94}Mo and ^{92}Mo is possible.

Another question to be addressed is the virtual photon field at higher energies. Depending on the model assumptions, the number of virtual photons may differ significantly in particular around the cut-off energy. Hence, the integral cross section retrieved from the data from Beil et al. could change considerably. The impact of differences in the virtual photon numbers increases with higher neutron separation energies, being critical especially for the proton-rich isotopes, as observed for ^{92}Mo and ^{94}Mo.

Furthermore, the energy dependence of the cross section will be investigated more closely in the future. Due to the limitations of the γ-detection during the molybdenum experiment, only the neutron energy in the center of mass could be determined. A detailed model of the decay of the excited nucleus could allow for an energy-dependent comparison with data based on real photons. If the deviation from the real-photon data is the same for all γ-energies, it could be concluded that the detection efficiency is not well understood. If, however, the deviation depends on the γ-energy, the virtual photon theory might need improvements.

3 Post-processing nucleosynthesis simulations for the p-process

Post-processing nucleosynthesis simulations for the p-process were carried out for a Supernova type II (SNII) and a Supernova type Ia (SNIa) model. The simulations using a Supernova type II model aimed at identifying the relevant production and destruction reactions for the p-nuclei of molybdenum and ruthenium and at determining the sensitivity of the final mass fractions to the rates of these reactions. The stellar environments for the simulations using a Supernova type Ia model were taken from simulations of Travaglio et al. [53, 86]. First, the final abundances obtained are compared to the results of Travaglio et al. Second, possible reasons for the different final mass fractions of ^{92}Mo and ^{94}Mo obtained in these stellar environments are investigated.

3.1 Post-processing nucleosynthesis simulations within the NuGrid project

3.1.1 PPN simulation framework

Post-processing nucleosynthesis (PPN) studies for the p-process were carried out within the Nucleosynthesis Grid (NuGrid) research platform [52]. NuGrid offers a software framework for nucleosynthesis simulations in astrophysical environments [87, 88]. Temperature and density profiles, so-called "trajectories" or "tracers", are obtained from simulations of stellar evolution that include only reactions relevant for the energy production. PPN processes the trajectories and calculates the stellar yields with a large network including more than 5,000 isotopes and more than 60,000 reactions. Different nuclear data sets can be chosen as input for the reaction network. This work uses the Basel reaction library (last updated on January 20, 2009) [44, 89] and the JINA Reaclib Database V1.1 [45, 90].

3.1.2   Initial abundance distributions

Pre-explosive isotopic abundances serve as seed distributions for the PPN simulations in this work. Figure 3.1 shows the seed distributions for the SNII and SNIa models as well as the solar abundances. The seeds for the SNII simulation were generated from a weak s-process trajectory [91, 92] processed in a PPN simulation of a 25 $M_\odot$ star [93, 94]. In this scenario, convective He core burning and C shell burning produce the s-abundances below $A \leq 90$ [17]. The seeds for the SNIa simulation were obtained from the model of a Chandrasekhar mass carbon-oxygen white dwarf that has accreted material from a companion giant star [53]. The material is assumed to become enriched with s-nuclei above $A \geq 90$ in a sequence of thermal pulse instabilities, with abundance distributions similar to the main s-component [17, 37] (compare Section 1.1.3). This work uses a seed distribution with metallicity of half the solar metallicity, $Z = 0.01$ [86].
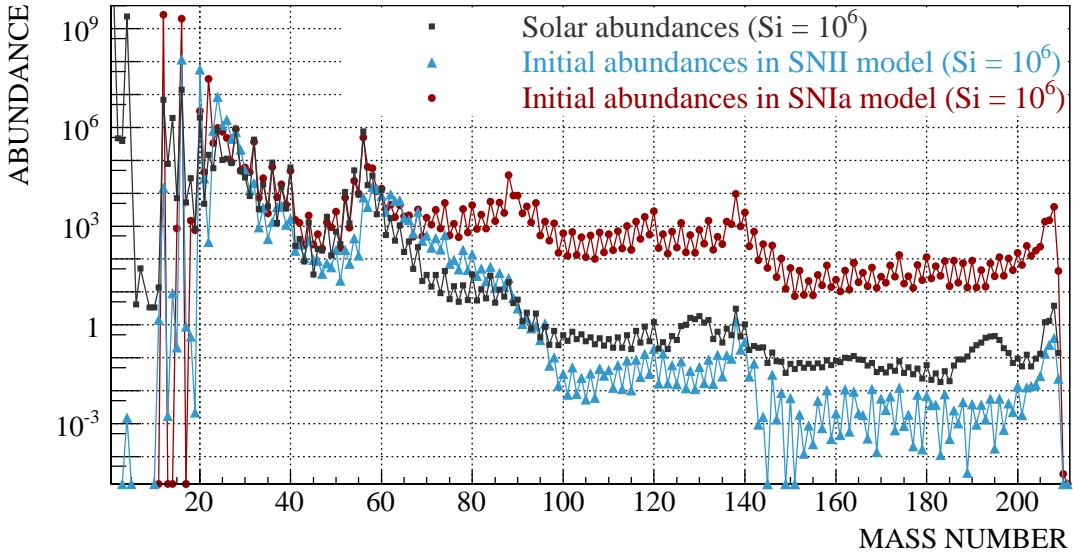
Figure 3.1.: Solar abundances (gray squares) [1], initial abundances for PPN simulations with a SNII model (blue triangles) [93, 94] and a SNIa model (red circles) [86]. The sum of the abundances of the stable Si isotopes was normalized to 10^6.

The PPN simulation stores the isotopic mass fractions and the (time-integrated) nucleosynthesis fluxes for every time step. The fluxes show the abundance variation caused by each reaction of the network [95]. NuGrid provides a set of python tools to analyze and visualize the data [88]. This work uses these tools for plotting the mass fraction evolution in the simulation. Several tools were developed within this work to display abundance distributions (ROOT [96]) and nucleosynthesis fluxes (Graphics Layout Engine (GLE) [97]).

3.1.3 Analysis tools

The analysis of the PPN simulation's data output uses several presentations of the data. This section gives a general overview of the chosen tools in this work.

Mass fraction evolution

The mass fraction X_i of an isotope i is the ratio of its mass m_i and the total mass M_{tot} of all isotopes:

$$X_i = \frac{m_i}{M_{tot}}.$$

M_{tot} is normalized to 1:

$$M_{tot} = \sum_n m_n = 1.$$

The evolution of mass fractions and the corresponding temperature profile are shown for the relevant time ranges in the simulation. Detailed plots concentrate on short time ranges around the maximum temperature of a trajectory.

Relative abundances

To obtain the abundance Y_i of an isotope i, its mass fraction X_i is divided by its mass number A_i:

$$Y_i = \frac{X_i}{A_i}.$$

The variation of a rate affects the final abundances. The ratio of an isotopic abundance obtained in the simulation with a modified rate and the isotopic abundance in the reference run gives the relative change in abundances. A new rate evaluation can directly be translated into an isotopic abundance without rerunning the simulation.

Nucleosynthesis fluxes

Nucleosynthesis fluxes show the main reaction paths for a certain time range in the simulation. The fluxes give important information about the relevance of a reaction for the isotopic abundances. The flux leading to the product nucleus via a certain reaction is defined by [88]

$$\frac{f_{Reaction}}{\Delta t} = \frac{\Delta Y_{Product,Reaction}}{\Delta t}.$$

The reaction rate and the abundance of the parent species determine the flux [87]. Relative nucleosynthesis fluxes for a single isotope represent the relative net abundance yield in the simulation. They also illustrate the most relevant reaction paths for the nucleus.

3.2 PPN simulations using a Supernova type II model

PPN simulations using a Supernova type II model aim at identifying the relevant reactions for the production and destruction of the Mo and Ru p-nuclei and at quantifying the effect of rate changes on the final mass fractions. Previous studies varied the rates of a certain type of reactions for either all reactions in the network or for all reactions involving the p-nuclei simultaneously [98, 99]. Single rates were varied in this work. The rates were multiplied/divided by factors of 2 and 5 for reactions involving a neutron ((γ,n) and (n,γ)) or a proton ((γ,p) and (p,γ)), and by factors of 5 and 10 for reactions involving an α-particle ((γ,α) and (α,γ)). The factors were chosen according to the commonly stated uncertainties of the reaction rates, which are a factor of 2 to 3 for proton and neutron captures, and up to a factor of 10 for reactions with low-energy α-particles [99] (and references therein).

3.2.1 Supernova type II model of a 25 $M_\odot$ star

A stellar progenitor with an initial mass of 25 $M_\odot$ and a metallicity of $Z = 0.02$ was used [92]. The Supernova type II model is the same as used by Rapp et al. [98]. In the model, the shock front passes through the Ne/O burning zone, which is subdivided into 14 mass layers. Table 3.1 lists the masses inside the shells, the maximum temperatures and densities for all mass layers. The innermost mass layer provides the hottest and densest environment with a peak temperature of 3.45 GK and a peak density of $7.85 \cdot 10^5$ g cm^{-3}. The maximum values drop continuously to 1.79 GK and $1.68 \cdot 10^5$ g cm^{-3} for the outermost mass layer. Figure 3.2 shows the temperature and density profiles of the so-called "Hashimoto trajectories", which describe the astrophysical environment of each layer as a function of time. The shock front reaches the mass layers successively. Temperature and density rapidly increase to the maximum values and afterwards drop slowly. Most of the nuclear reaction rates for the PPN simulations adopted are taken from the JINA Reaclib Database V1.1.

Layer	Mass inside the shell ($M_\odot$)	Maximum temperature (GK)	Maximum density (10^5 g cm^{-3})
1	1.9336	3.45	7.85
2	1.9658	3.11	6.64
3	2.0085	2.96	5.68
4	2.0508	2.76	4.82
5	2.1037	2.60	4.07
6	2.1564	2.44	3.56
7	2.2090	2.32	3.16
8	2.2614	2.21	2.80
9	2.3136	2.12	2.54
10	2.3655	2.04	2.30
11	2.4171	1.97	2.11
12	2.4684	1.91	1.94
13	2.5249	1.84	1.75
14	2.5825	1.79	1.68

Table 3.1.: Parameters of the Hashimoto trajectories: masses inside each of the 14 mass shells, maximum temperatures and maximum densities for each mass layer [98].
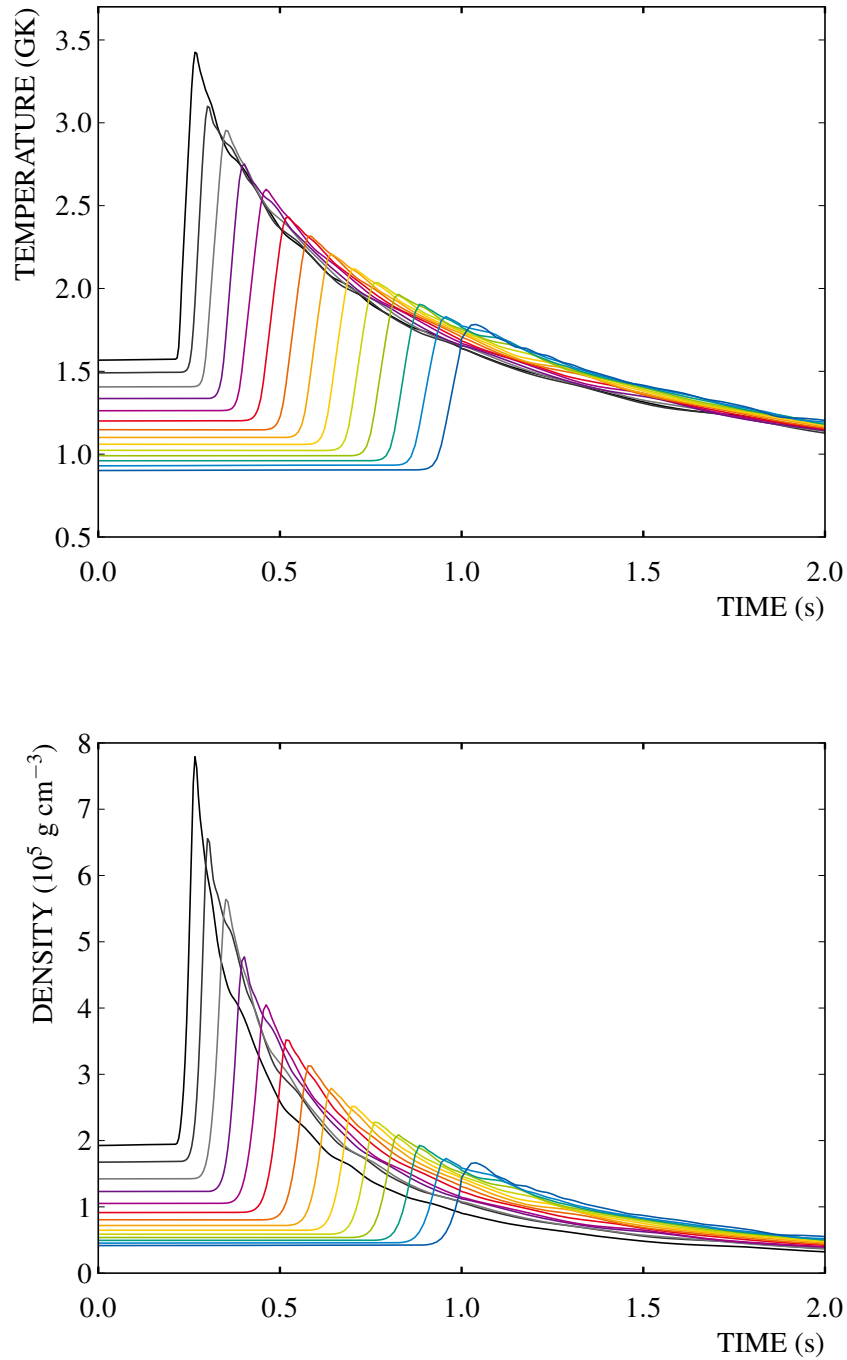
Figure 3.2.: Temperature (top) and density (bottom) profiles of the Hashimoto trajectories. Left to right: profiles from the innermost mass layer to the outermost one. The shock front reaches the mass layers successively.

3.2.2 Production and destruction of the Mo and Ru p-nuclei

Figure 3.3 shows an overview of the nucleosynthesis fluxes producing and destroying molybdenum and ruthenium isotopes. In the isotopic chains, (γ,n) and (n,γ) reactions compete and are the main reaction paths for the production of the neutron-rich isotopes. The reaction paths branch on the proton-rich side. The isotopes ^{92}Mo, ^{93}Mo and ^{94}Mo, as well as ^{96}Ru, ^{97}Ru and ^{98}Ru are also produced and destroyed by (γ,p) and (γ,α) reactions. The (p,γ), (n,α), (n,p) and (p,n) reactions account for a small fraction of the nucleosynthesis fluxes, which is three to four orders of magnitude lower than the maximum flux.
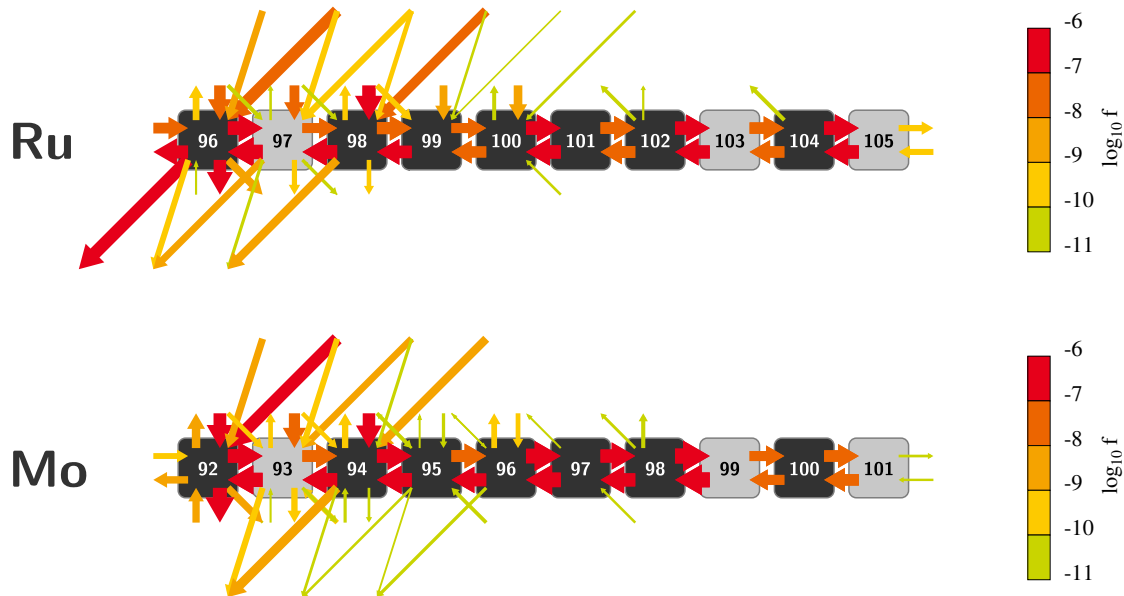
Figure 3.3.: Time-integrated fluxes f producing and destroying the Mo and Ru isotopes in the post-processing nucleosynthesis simulation of the 25 $M_\odot$ Supernova type II model. Colors indicate the order of magnitude of the flux, the arrow thicknesses scale linearly with $\log_{10} f$.

The relative time-integrated fluxes for the isotopes ^{92}Mo, ^{94}Mo, ^{96}Ru and ^{98}Ru are shown in Figure 3.4. For each isotope, the sum of all production fluxes is normalized to 100%, and the destruction fluxes are scaled with the same factor. Fluxes smaller than 1% are not shown. If the sum of destruction fluxes is less than 100%, there is a net yield in the simulation, otherwise the isotope is depleted. For all isotopes in the plot, the sum of the production fluxes is larger than the sum of the destruction fluxes, i.e. all abundances increase. The isotope ^{92}Mo has the largest net yield with 100% production and 93% destruction.
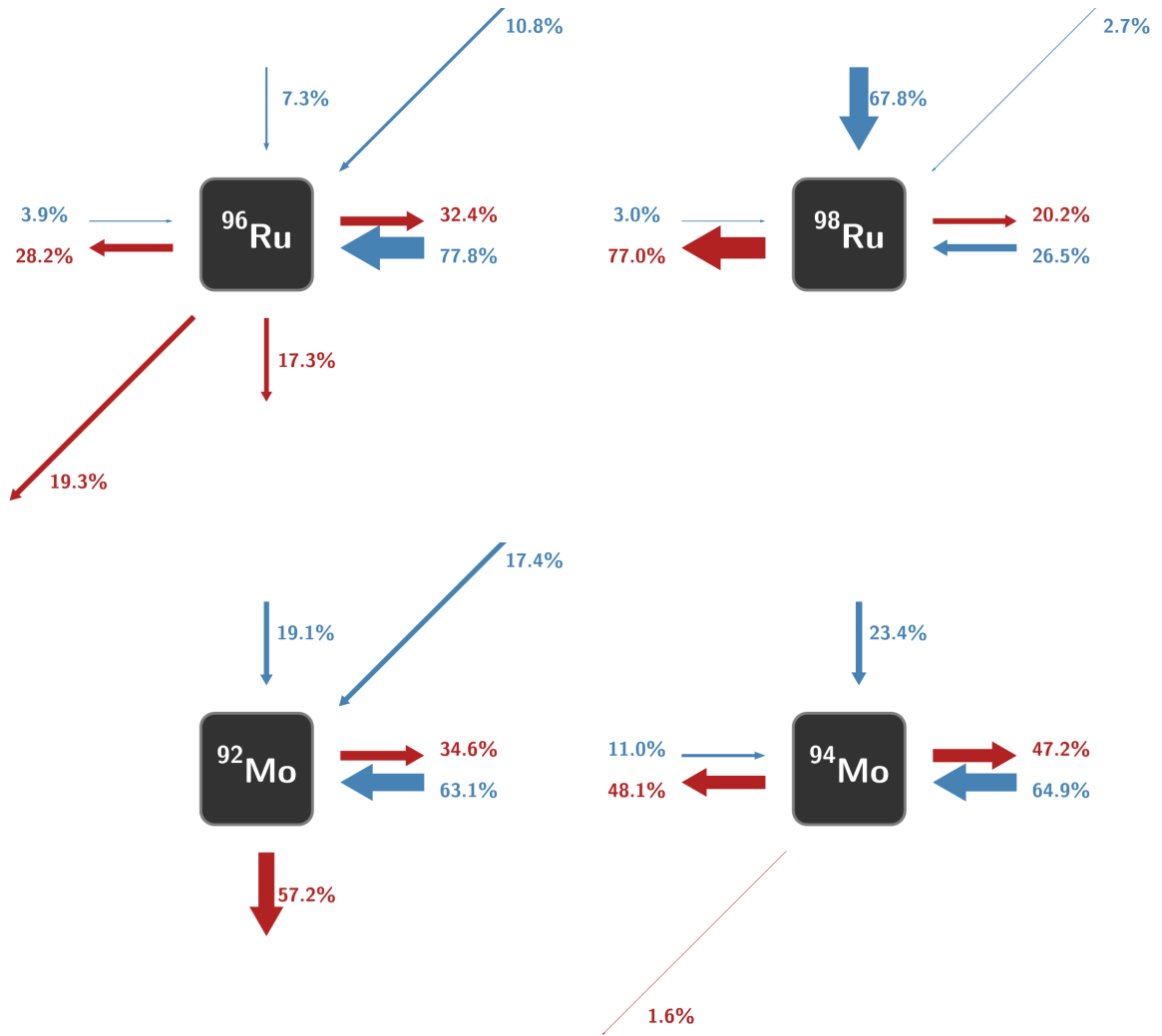
Figure 3.4.: Relative time-integrated fluxes producing (blue) and destroying (red) the p-nuclei ^{92}Mo, ^{94}Mo, ^{96}Ru and ^{98}Ru in the post-processing nucleosynthesis simulation of the 25 $M_\odot$ Supernova type II model. The sum of all production fluxes is normalized to 100% for each isotope, and the destruction fluxes are scaled with the same factor. Fluxes smaller than 1% are not shown.

The isotopes ^{92}Mo and ^{94}Mo are mainly produced by photodisintegration reactions on more neutron-rich molybdenum isotopes. The reaction ^{92}Mo(γ,p) is the main destruction path of the proton-rich isotope ^{92}Mo, which has a closed neutron shell. The isotope ^{94}Mo is destroyed by neutron-dissociation and neutron-capture reactions on equal terms.

The ^{97}Ru(γ,n) reaction is the main production path of ^{96}Ru. Several γ-induced reactions as well as neutron-capture reactions are responsible for the destruction of ^{96}Ru. The isotope ^{98}Ru is mainly produced by ^{99}Rh(γ,p) reactions and destroyed by neutron dissocitation reactions.

The reactions shown here determine the abundances of the Mo and Ru p-nuclei. These local reactions are subject of the rate variation study (Section 3.2.3). However, reactions on heavier isotopes may affect the nucleosynthesis fluxes leading to the p-nuclei of Mo and Ru. Section 3.2.4 investigates the global production and destruction flows in the Supernova type II simulation.

3.2.3   Abundances of ^{92,94}Mo and ^{96,98}Ru depending on local production and destruction rates

The effect of single rate variations on the final abundances of the p-nuclei ^{92}Mo, ^{94}Mo, ^{96}Ru and ^{98}Ru was determined by variation of the reaction rates accounting for more than 1% of the relative nucleosynthesis fluxes (Section 3.2.2). The rate is calculated in the astrophysical environment in the PPN simulation from the parameters taken from the chosen reaction library (Equation 1.10) and then multiplied by the factor set by the user.

Reactions may alter the abundances of the p-nuclei directly if the p-nuclei is the parent or the product of the reaction. In addition, reactions may affect the p-nuclei's abundance indirectly by changing the abundance of species, which in turn may act as parent specie of the p-nuclei, or by altering the reaction path, which then may bypass the p-nuclei.

The production and destruction nucleosynthesis fluxes determine the isotopic abundances. The fluxes result from the reaction rates and the abundances of the parent isotopes of the reactions in the astrophysical environment. The impact of a rate therefore depends on its absolute value and the abundance distribution in every time step of the simulation. Both parameters are discussed in detail in the following.

3.2.3.1   Photon-induced production and destruction rates

Figures 3.5 and 3.6 show the γ-induced reaction rates relevant for the production and destruction of the light p-nuclei. The parameters to calculate the rates according to equation 1.10 are taken from JINA Reaclib Database V1.1 [45].

The upper plot in Figure 3.5 displays the rates relevant for the production and destruction of ^{92}Mo. The ^{93}Mo(γ,n) rate is the highest rate in the temperature range shown followed by the ^{94}Mo(γ,n) rate. The ^{96}Ru(γ,α) and ^{98}Ru(γ,n) rates are equal at $T = 2.4$ GK, but the ^{98}Ru(γ,n) rate increases faster with higher temperatures. The rate of the reaction ^{92}Mo(γ,p), which destroys ^{92}Mo, and the rate of the reaction ^{94}Mo(γ,α), which affects the ^{92}Mo abundance by changing the reaction path, are in the same order of magnitude.

The production and destruction rates of ^{94}Mo are shown in the lower part of Figure 3.5. The highest rate is ^{95}Mo(γ,n). Of the destruction rates, the ^{94}Mo(γ,n) rate is higher and shows a steeper slope than the ^{94}Mo(γ,α) rate. The reaction ^{93}Mo(γ,n) affects the ^{94}Mo abundance due to the competition with the ^{93}Mo(n,γ) rate producing ^{94}Mo. The ^{93}Mo(γ,n) rate is the highest one of the γ-induced destruction rates plotted here.

The upper plot in Figure 3.6 shows the rates of reactions producing and destroying ^{96}Ru. The reaction ^{98}Ru(γ,n) is part of the main production path of photodisintegration reactions starting from heavier Ru isotopes. Its rate is the highest one plotted here. The rate of the direct production reaction ^{100}Pd(γ,α) is 1 to 1.5 orders of magnitude lower. The reaction ^{102}Pd(γ,α) produces ^{98}Ru and, therefore, indirectly affects the ^{96}Ru abundance. The rate is an order of magnitude lower than the ^{100}Pd(γ,α) rate. The destruction rates of the ^{96}Ru(γ,α), ^{96}Ru(γ,p) and ^{96}Ru(γ,n) reactions are in the same order of magnitude.

The rate of the ^{98}Ru production reaction ^{99}Ru(γ,n) is about four orders of magnitude higher than the ^{102}Pd(γ,α) rate (Figure 3.6, lower plot). The rate of the destruction reaction ^{98}Ru(γ,n) is 1 to 1.5 orders of magnitude lower than the rate of ^{97}Ru(γ,n), which has an indirect impact on the ^{98}Ru abundance. The reaction ^{100}Pd(γ,α) shows the lowest rate.
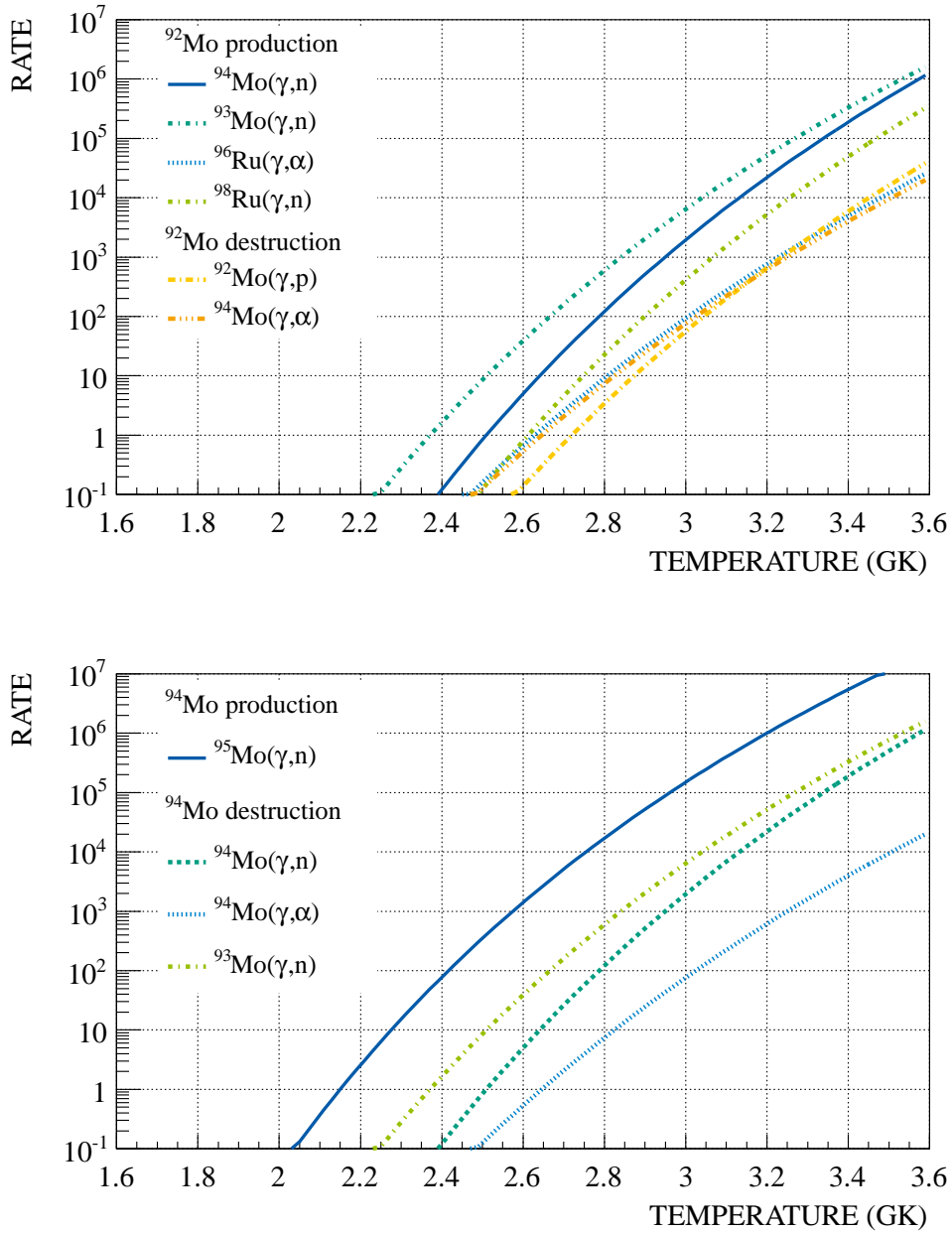
Figure 3.5.: Photon-induced rates from JINA reaction library V1.1 relevant for the production and destruction of the p-nuclei ^{92}Mo (top) and ^{94}Mo (bottom). For details, see text.
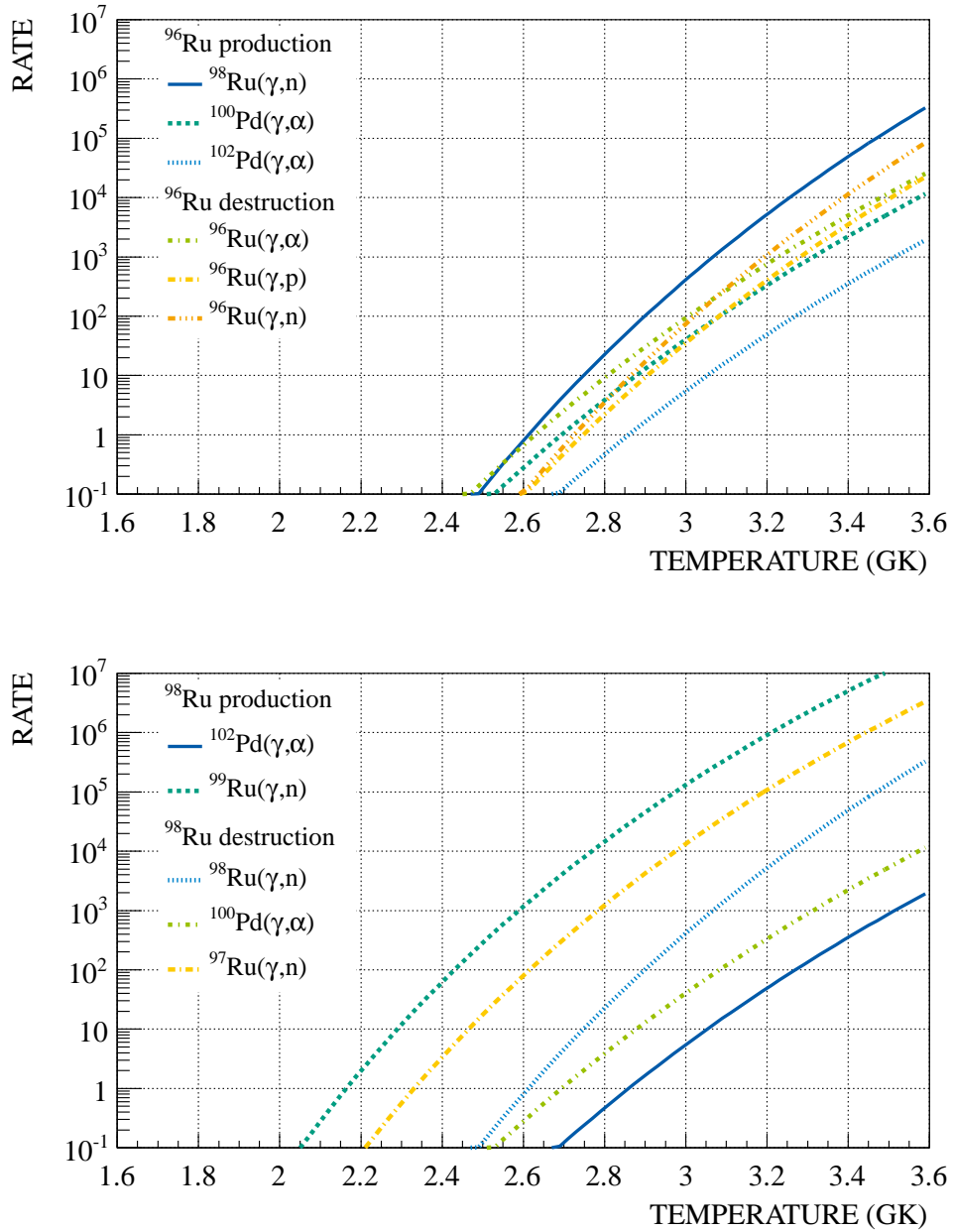
Figure 3.6.: Photon-induced rates from JINA reaction library V1.1 relevant for the production and destruction of the p-nuclei ^{96}Ru (top) and ^{98}Ru (bottom). For details, see text.

3.2.3.2   Mass fraction trends in the Supernova type II simulation

The nucleosynthesis fluxes depend on the abundance of the parent species of the reaction. Figure 3.7 show the mass fractions of the isotopes discussed in this work as a function of time for the Hashimoto trajectories 1 (hottest environment) and 4. The isotope ^{94}Mo is produced most in trajectories 4 and 5. The abundances of the Mo, Ru and Pd isotopes are strongly affected in these trajectories. For completeness, the mass fraction trends of the other Hashimoto trajectories are plotted in Figures A.1 to A.12 in the appendix.

When the temperature reaches about 2.5 GK, the light p-nuclei are produced by photodisintegration reactions starting from heavier nuclei. The light p-nuclei are destroyed by γ-induced reactions when the temperature is higher than about 3.0 GK (compare Figures in 3.7).

The masses are shifted from heavier isotopes to the light isotopes via γ-induced reactions in the innermost mass shell of the 25 $M_\odot$ star (Hashimoto trajectory 1, Figure 3.7 (top)). The isotope ^{92}Mo is the most abundant one in the high temperature phase followed by ^{96}Ru, ^{100}Pd and ^{102}Pd. The p-nucleus ^{98}Ru is about an order of magnitude less abundant than ^{92}Mo, the nuclei ^{97}Ru is about two orders of magnitude less abundant. The peak abundances of the isotopes ^{94}Mo, ^{93}Mo, ^{95}Mo and ^{99}Ru are reached earlier and drop by one to two orders of magnitude until the peak abundance of ^{92}Mo is reached.

The temperature profile of the fourth mass shell (Hashimoto trajectory 4, Figure 3.7 (bottom)) reaches a maximum of 2.76 GK. The light p-nuclei are produced by γ-induced reactions but not disintegrated further due to the relatively low temperature. The p-nucleus ^{94}Mo is the most abundant isotope at the temperature peak. The abundances of ^{92}Mo, ^{93}Mo, ^{95}Mo, ^{98}Ru and ^{102}Pd are about equal and an order of magnitude lower than the ^{94}Mo abundance. The isotopes ^{96}Ru, ^{97}Ru and ^{99}Ru are yet another order of magnitude less abundant. The isotope ^{100}Pd is produced in the high temperature phase and reaches an abundance about four orders of magnitude lower than ^{94}Mo at the peak temperature.
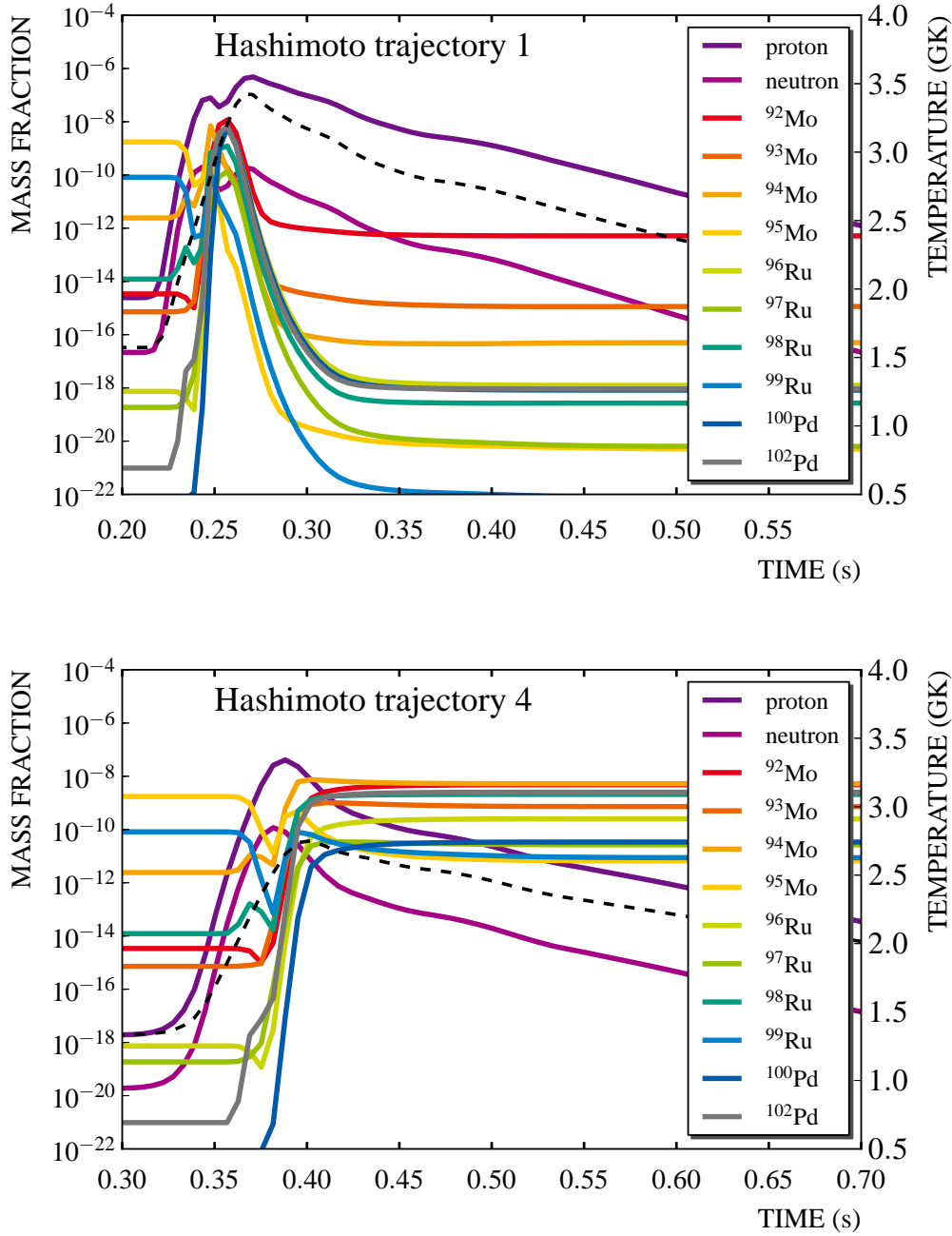
Figure 3.7.: Mass fractions of Mo, Ru and Pd isotopes as a function of time in the high temperature phases of Hashimoto trajectories 1 (top) and 4 (bottom) of the Supernova type II model. The dashed black line shows the temperature profile.

3.2.3.3   Results

This work shows the dependencies for the rates where the maximum abundance ratio is larger than 5% within the applied rate variations.

The case of ^{92}Mo

Figure 3.8 shows the final abundance of ^{92}Mo as a function of the factor applied to one production or one destruction rate. The ^{92}Mo abundance strongly depends on the ^{92}Mo(γ,p) rate, which is the main destruction path. The ^{92}Mo abundance drops with increasing rate, and vice versa (Figure 3.8, top). Neutron-dissociation reactions are the main production path of ^{92}Mo (Figure 3.8, bottom). Variations of the rate of the reaction ^{94}Mo(γ,n) show a stronger impact on the ^{92}Mo abundance than of the reaction ^{93}Mo(γ,n) since ^{93}Mo is unstable and has to be produced first. The rate of the reaction ^{96}Ru(γ,α) shows a small influence as the rate is lower than the other production rates of ^{92}Mo (compare Figure 3.5). The reaction ^{98}Ru(γ,n) indirectly affects the abundance of ^{92}Mo since it is one of the reactions producing ^{96}Ru from heavier Ru isotopes. The ^{92}Mo abundance drops if the rate of the reaction ^{94}Mo(γ,α) increases. If the ratio of the reaction rates of ^{94}Mo(γ,α) and ^{94}Mo(γ,n) is larger, the nucleosynthesis path is altered and the isotope ^{92}Mo is bypassed.

The case of ^{94}Mo

Photodisintegration reactions starting from heavier Mo isotopes produce ^{94}Mo. The destruction reaction ^{94}Mo(γ,n) mainly determines the final abundance of ^{94}Mo. A small fraction of the nucleosynthesis fluxes proceeds via ^{94}Mo(γ,α). A decrease of the rate hardly changes the ^{94}Mo abundance since the rate is about two orders of magnitude smaller than the ^{94}Mo(γ,n) rate (compare Figure 3.5). The reaction ^{95}Mo(γ,n) directly produces ^{94}Mo. Variations of the reaction rate change the abundance of ^{94}Mo by up to about 15%. If the ^{93}Mo(γ,n) rate is increased compared to the ^{93}Mo(n,γ) rate, the production of ^{94}Mo via (n,γ) reactions becomes less prominent. However, variations of the reaction rate of ^{93}Mo(γ,n) show little modifications of the ^{94}Mo abundance since the abundance of ^{93}Mo is smaller (see Figure 3.7), although the rate is larger than the ^{94}Mo(γ,n) rate (Figure 3.5).
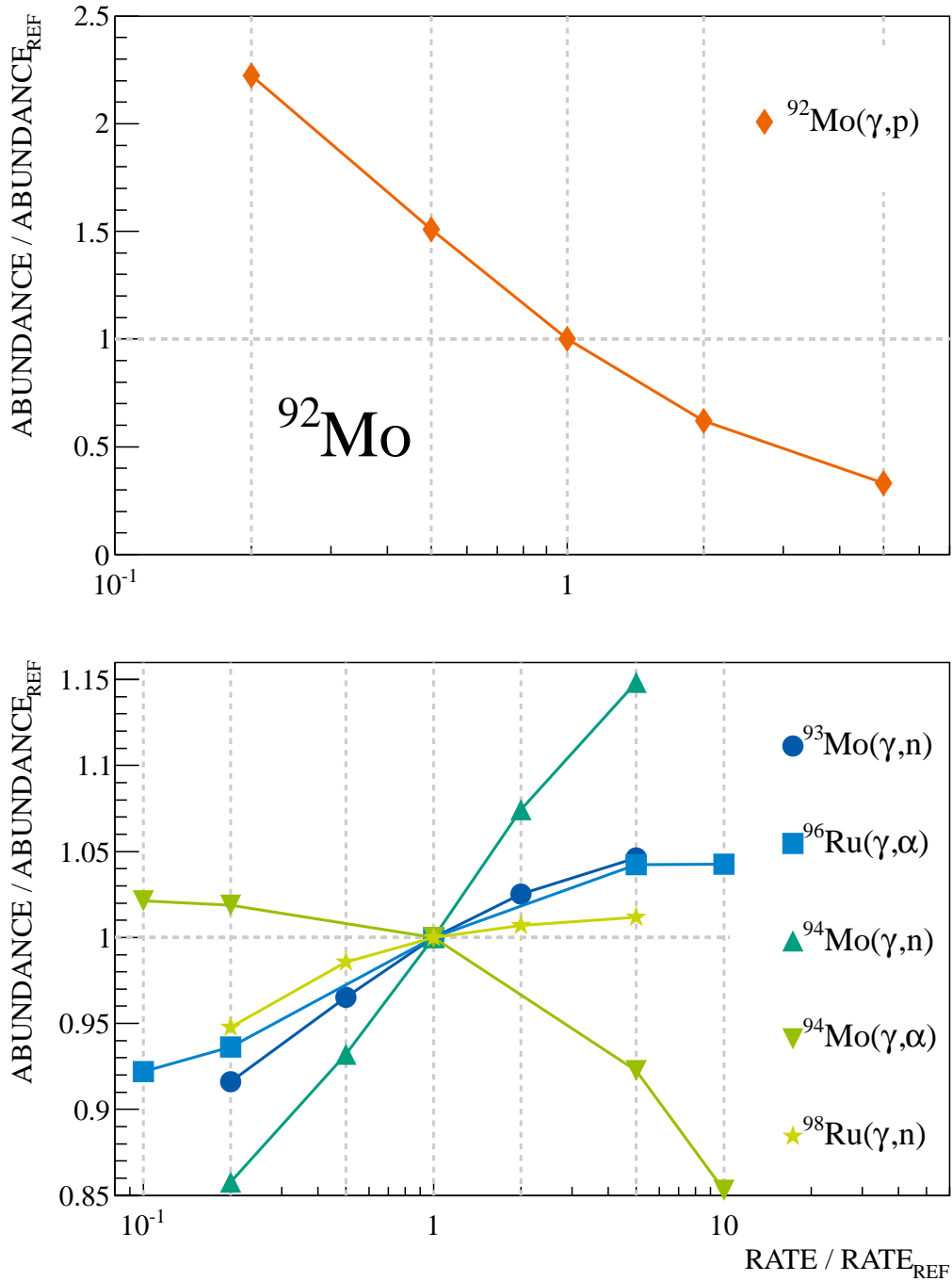
Figure 3.8.: Impact on the abundance of ^{92}Mo depending on the γ-induced rates producing and destroying the light p-nuclei ^{92}Mo, ^{94}Mo, ^{96}Ru and ^{98}Ru. The results for the reaction rate of ^{92}Mo(γ,p) (top) are shown in a single plot due to its large impact on the abundance compared to the other reaction rates.
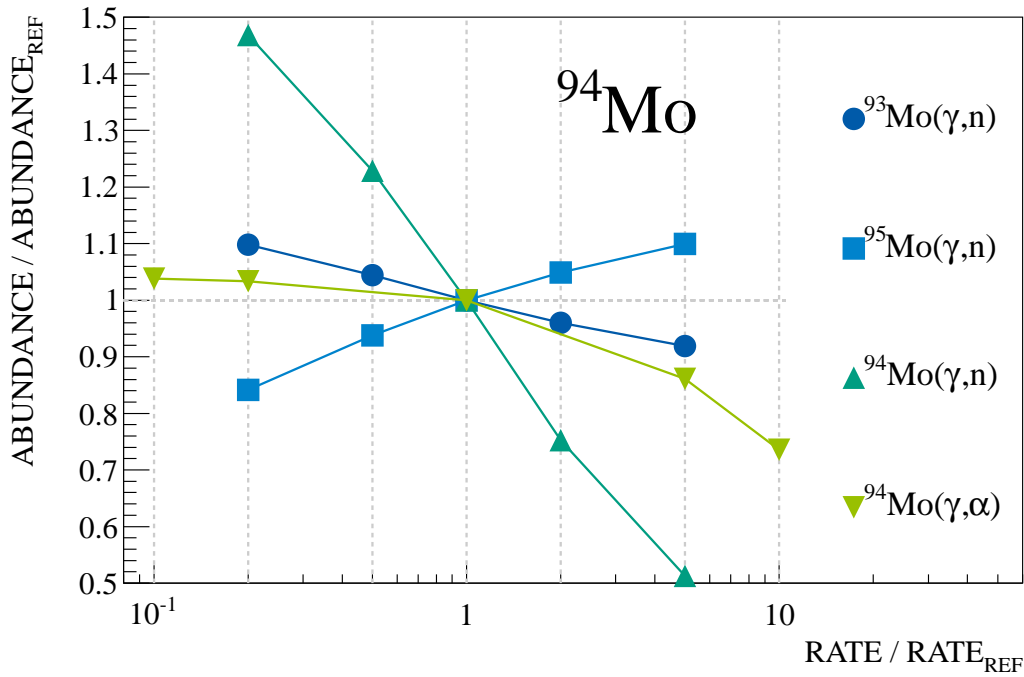
Figure 3.9.: Impact on the abundance of ^{94}Mo depending on the γ-induced rates producing and destroying the light p-nuclei ^{92}Mo, ^{94}Mo, ^{96}Ru and ^{98}Ru.

The case of ^{96}Ru

Photodisintegration reactions starting from heavier Ru isotopes are the main production path of ^{96}Ru. The reaction ^{98}Ru(γ,n) has the largest influence on the ^{96}Ru abundance. Variations in the ^{100}Pd(γ,α) rate have a smaller impact. The variation of the reaction ^{102}Pd(γ,α), which produces ^{98}Ru, has a small indirect impact on ^{96}Ru.

The reaction rate of ^{96}Ru(γ,α) strongly affects the ^{96}Ru abundance. The rate of the reaction ^{96}Ru(γ,α) is higher than the rates of the reactions ^{96}Ru(γ,p) and ^{96}Ru(γ,n) for temperatures up to 3 GK (compare Figure 3.6). The latter two are in the same order of magnitude, while the rate of the reaction ^{96}Ru(γ,n) rises steeper. Nevertheless, they show the same impact on the ^{96}Ru abundance.
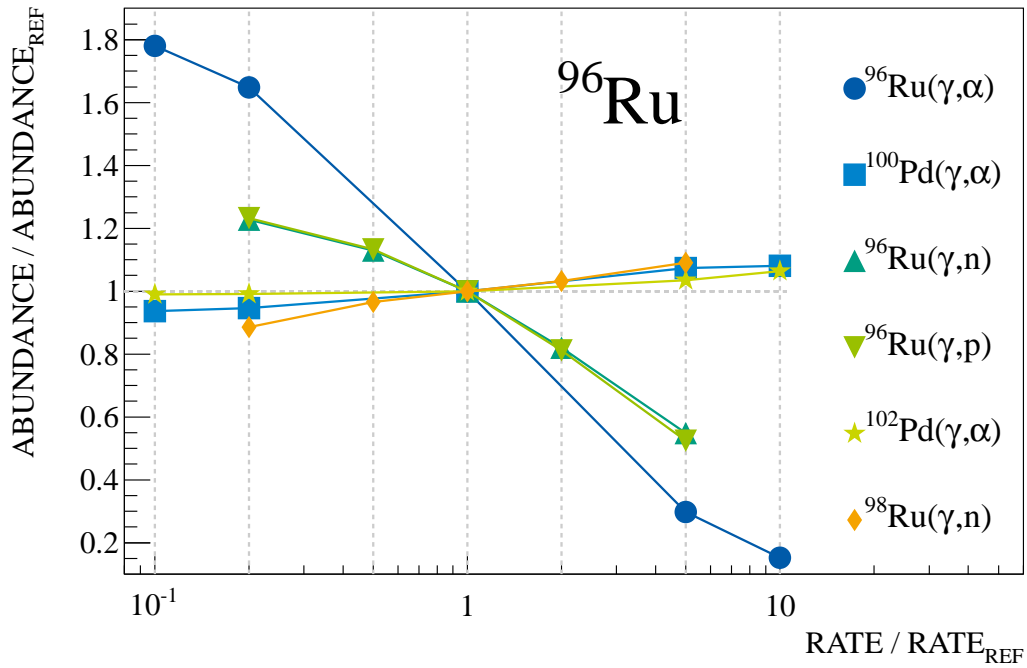
Figure 3.10.: Impact on the abundance of ^{96}Ru depending on the γ-induced rates producing and destroying the light p-nuclei ^{92}Mo, ^{94}Mo, ^{96}Ru and ^{98}Ru.

The case of ^{98}Ru

The variation of the ^{102}Pd(γ,α) rate has the largest impact on the production of ^{98}Ru (compare Figure 3.11, bottom). Although the ^{99}Ru(γ,n) rate is by orders of magnitude larger than the ^{102}Pd(γ,α) rate (Figure 3.6), the variation of the rate changes the final abundance of ^{98}Ru by less than 10%. The isotope ^{102}Pd is about two orders of magnitude more abundant than ^{99}Ru in the high temperature phase of the simulation (compare Figure 3.7) and, therefore, determines the nucleosynthesis fluxes producing ^{98}Ru.

The reaction ^{98}Ru(γ,n) strongly impacts the destruction of ^{98}Ru (Figure 3.11, top). The reaction ^{100}Pd(γ,α) determines the reaction path. If the rate is increased, the isotope ^{98}Ru is bypassed. Changes in the rate of the reaction ^{97}Ru(γ,n) indirectly affect the ^{98}Ru abundance by reducing the backflow via (n,γ) reactions.
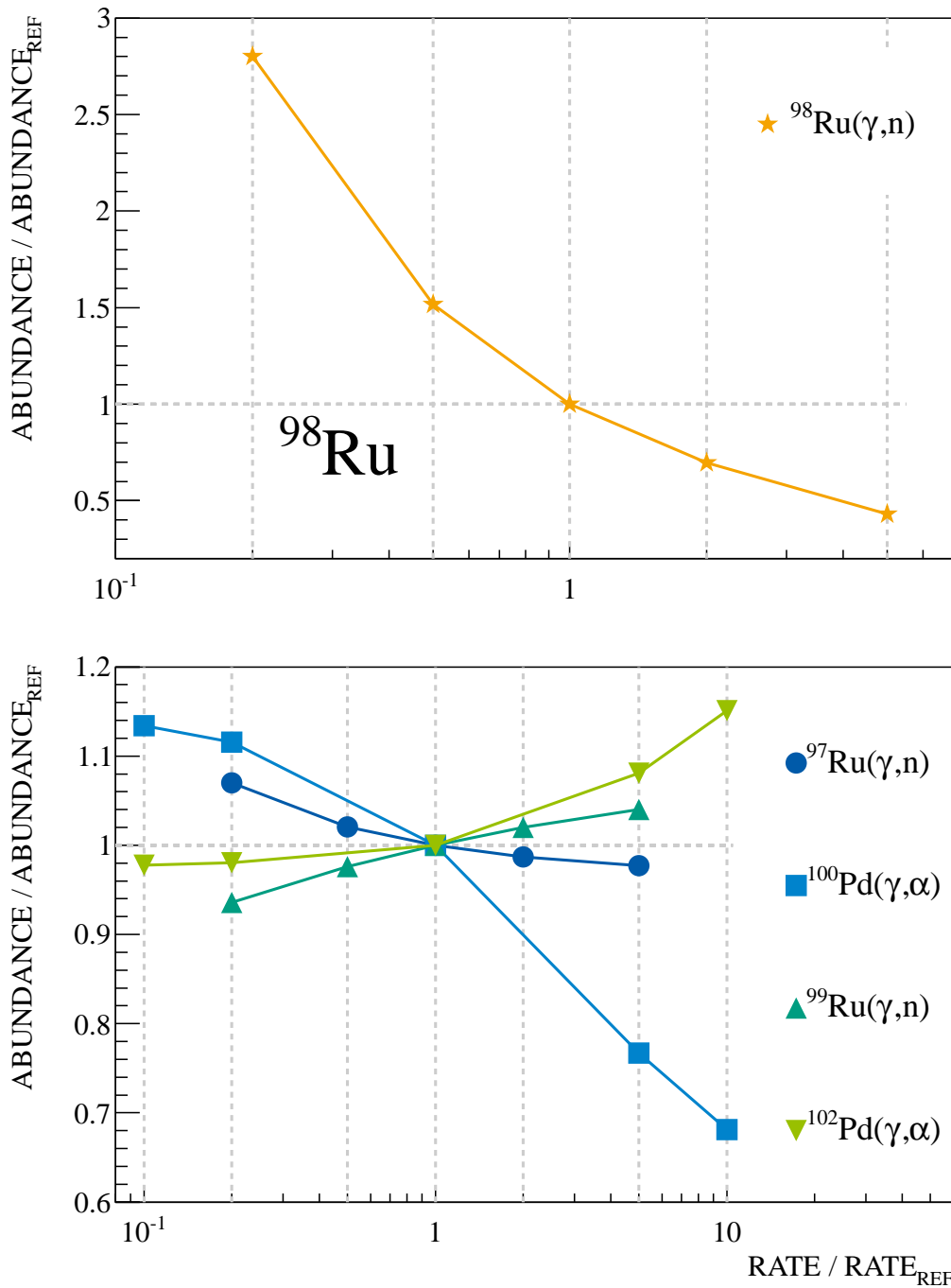
Figure 3.11.: Impact on the abundance of ^{98}Ru depending on the γ-induced rates producing and destroying the light p-nuclei ^{92}Mo, ^{94}Mo, ^{96}Ru and ^{98}Ru. The results for the reaction rate of ^{98}Ru(γ,n) (top) are shown in a single plot due to its large impact on the abundance compared to the other reaction rates.

Conclusions

Table 3.2 lists the reactions that change the mass fractions of the p-nuclei ^{92}Mo, ^{94}Mo, ^{96}Ru and ^{98}Ru by more than 20% within the applied rate variations. All rates destroy the corresponding p-nuclei directly, with the exception of ^{100}Pd(γ,α), which indirectly reduces the amount of ^{98}Ru produced. New evaluated data can be compared to the reaction rates taken from JINA Reaclib Database V1.1. The new final mass fractions of the Mo and Ru p-nuclei can be obtained directly from the results presented here if the new values lie within the range of the variations applied in this work.

p-nuclei	reaction
^{92}Mo	^{92}Mo(γ,p)
^{94}Mo	^{94}Mo(γ,n), ^{94}Mo(γ,α)
^{96}Ru	^{96}Ru(γ,α), ^{96}Ru(γ,p), ^{96}Ru(γ,n)
^{98}Ru	^{98}Ru(γ,n), ^{100}Pd(γ,α)

Table 3.2.: Reactions changing the mass fractions of the p-nuclei ^{92}Mo, ^{94}Mo, ^{96}Ru and ^{98}Ru by more than 20% within the applied rate variations. The reaction rates were taken from JINA Reaclib Database V1.1 [90].

3.2.3.4   Neutron-capture reactions

Figure 3.12 shows the abundances of ^{92}Mo, ^{94}Mo, ^{96}Ru and ^{98}Ru depending on the neutron-capture rates producing and destroying the light p-nuclei. The rates were varied by factors 0.5 and 2.0. The dependencies for those rates are plotted where the maximum abundance ratio is larger than 2% within the applied rate variations. The final abundances change by less than 10%. The isotope ^{94}Mo shows the largest abundance ratio when its destruction rate ^{94}Mo(n,γ) is varied.

The rate of the reaction ^{94}Mo(n,γ) affects the final abundance of ^{92}Mo. If the rate increases, the abundance of ^{92}Mo increases, and vice versa. The isotope ^{92}Mo is mainly destroyed by proton-dissociation reactions in the high temperature regime. An increase in the rate may delay the nucleosynthesis flow via neutron-dissociation reactions towards the neutron shell closure at ^{92}Mo and reduce the fraction of (γ,p) destruction reactions of ^{92}Mo.

Variations of local neutron-capture rates hardly influence the abundances of the p-nuclei of molybdenum and ruthenium. However, experimentally determined (n,γ) cross sections are

used to calculate the (γ,n) cross sections by applying the detailed balance theorem. Neutron-capture cross sections are typically uncertain by about 20% in s-process scenarios and by up to a factor of 2 in hot environments like p-process scenarios [17]. Reduced uncertainties from improved measurements may further constrain the neutron-dissociation reactions relevant for the p-process.
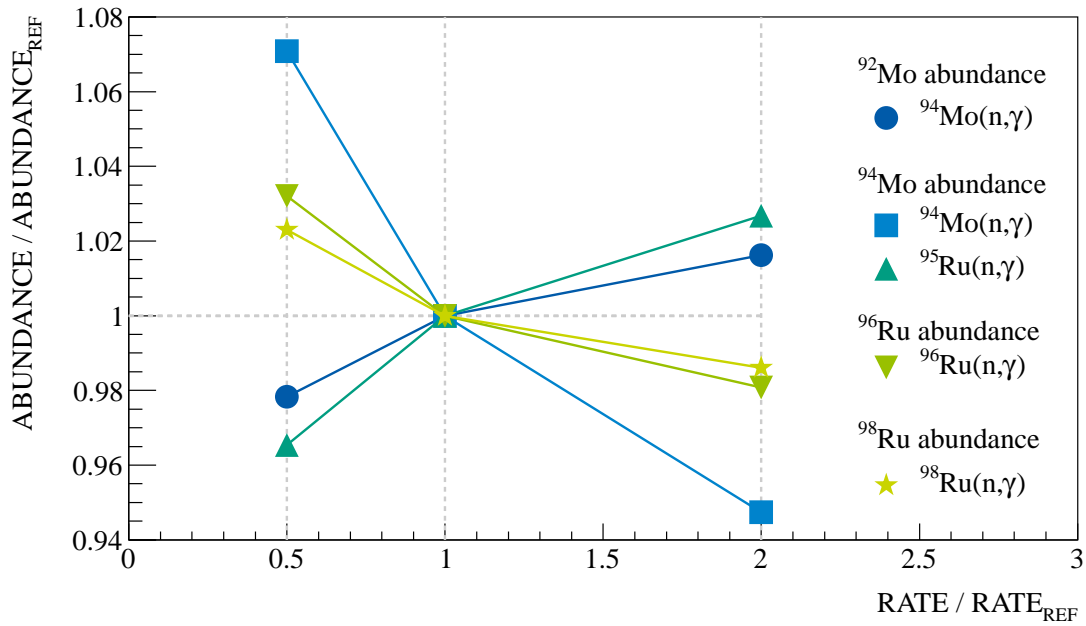
Figure 3.12.: Abundances of ^{92}Mo, ^{94}Mo, ^{96}Ru and ^{98}Ru depending on the neutron-capture rates producing and destroying the light p-nuclei ^{92}Mo, ^{94}Mo, ^{96}Ru and ^{98}Ru. The plot shows the dependencies for the rates where the maximum abundance ratio is larger than 2% within the applied rate variations.

3.2.4 Production and destruction flows

Figure 3.13 shows the initial abundances of the p-nuclei for the Supernova type II simulations and the final abundances of Hashimoto trajectories 1 to 6. The heavy p-nuclei are disintegrated in the innermost mass shells. Even the p-nuclei of Mo and Ru are destroyed in the hottest environment of trajectory 1. The reaction flow leads to high abundances of the lightest p-nuclei ^{74}Se, ^{78}Kr, ^{84}Sr and ^{92}Mo (trajectories 1 to 3). Trajectories 2 to 4 dominate the production of the p-nuclei with mass numbers 100 to 140. The heavy p-nuclei are mostly produced by disintegration reactions on heavier isotopes in the same isotopic chain in the cooler trajectories 4 to 6.
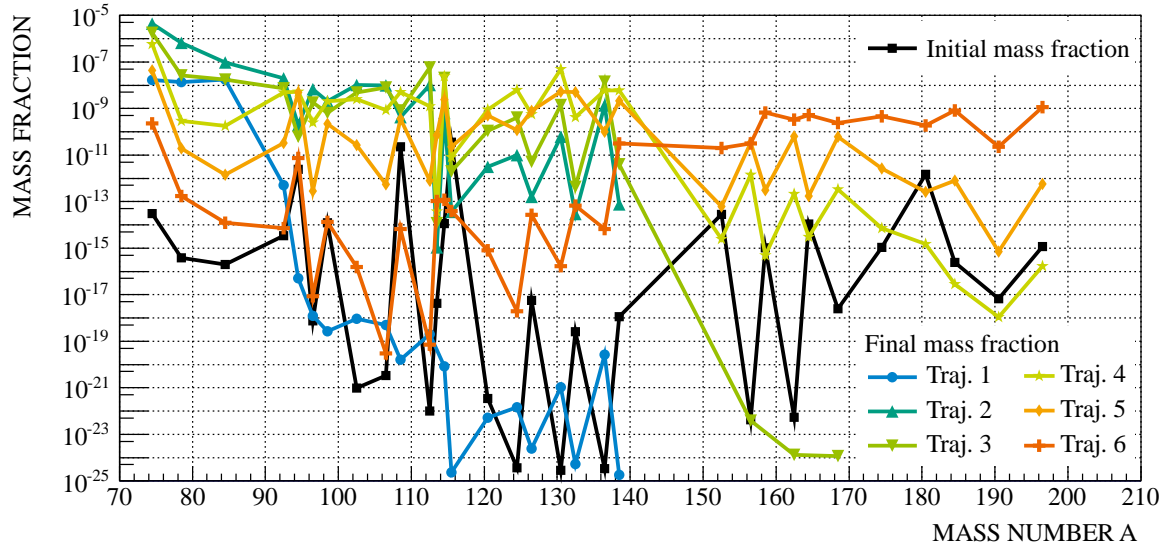
Figure 3.13.: Initial and final mass fractions of all p-nuclei for Hashimoto trajectories 1 to 6. Mass fractions smaller than 10^{-25} are not shown.

Figures 3.14 and 3.15 show the time-integrated fluxes producing and destroying the nuclei ^{92}Mo, ^{94}Mo, ^{96}Ru and ^{98}Ru for Hashimoto trajectories 1 and 5. Many γ-induced reactions produce or destroy the p-nuclei in the hottest environment. Photon-induced reactions are each responsible for more than 90% of the production fluxes in the cooler temperature regime of trajectory 5. In turn, radiative neutron-capture reactions are the main destructions paths, but account only for up to about 50% of the destruction fluxes.

The isotopes ^{92}Mo and ^{96}Ru behave similarly. They are mostly produced in trajectories 2 to 4, and only little in trajectory 6. Neutron-, proton- and α-dissociation reactions lead to the p-nuclei ^{92}Mo and ^{96}Ru in the hottest environment. Also, the main fraction of ^{96}Ru is destroyed by these reactions. Of the γ-induced reactions, only (γ,p) reactions destroy ^{92}Mo due to the high neutron- and α-separation energies at the neutron shell closure.

The isotope ^{94}Mo is produced by (γ,n), (γ,p) and (n,γ) reactions in the innermost mass shell. About the same amount of ^{94}Mo is destroyed via the reactions ^{94}Mo(γ,n) and ^{94}Mo(n,γ), only a minor fraction via the reaction ^{94}Mo(γ,α). In trajectory 5, the isotope ^{94}Mo is only produced and destroyed by the reactions ^{94}Mo(γ,n) and ^{94}Mo(n,γ).

The main production and destruction paths of ^{98}Ru are similar to those of ^{94}Mo, but the fractions are different. ^{98}Ru is mainly produced by (γ,p) reactions and mainly destroyed by (γ,n) reactions.

Conclusions

The p-nuclei ^{92}Mo, ^{94}Mo and ^{96}Ru are mainly produced by (γ,n) reactions starting from heavier Mo and Ru isotopes, respectively, independent of the maximum temperature of the mass shell. The fraction of production fluxes via (γ,p) reactions increases with higher temperatures. The production via (γ,α) reactions is only relevant for the lightest p-nuclei of Mo and Ru in the high temperature regime.
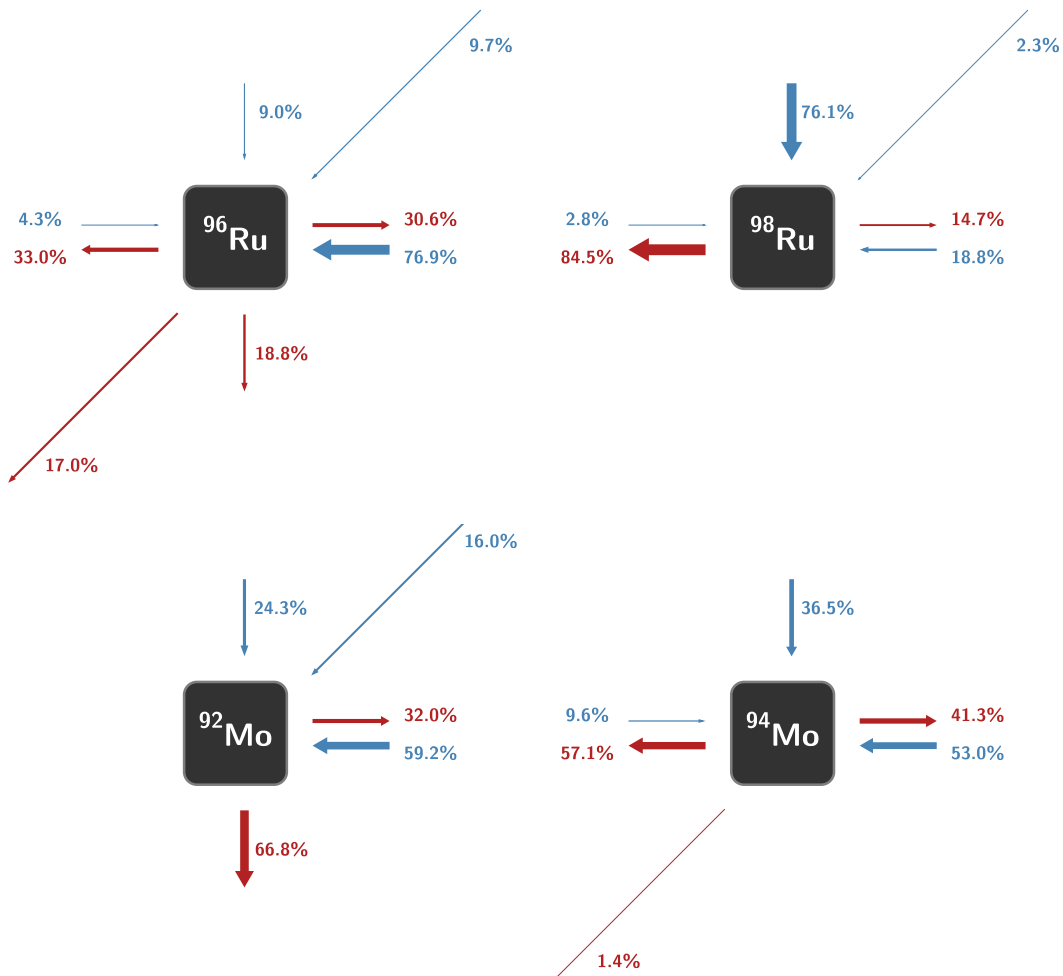
Figure 3.14.: Relative time-integrated fluxes producing (blue) and destroying (red) the nuclei ^{92}Mo, ^{94}Mo, ^{96}Ru and ^{98}Ru for Hashimoto trajectory 1 in the post-processing nucleosynthesis simulation of the 25 $M_\odot$ Supernova type II model. The sum of all production fluxes is normalized to 100% for each isotope, and the destruction fluxes are scaled with the same factor. Fluxes smaller than 1% are not shown.
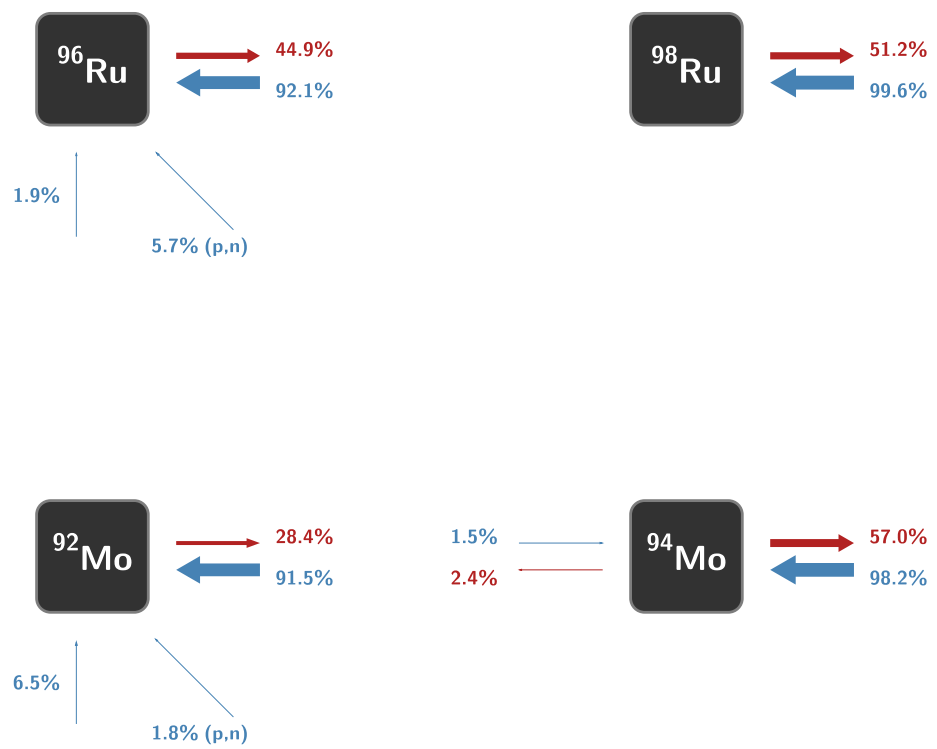
Figure 3.15.: Same as Figure 3.14, for Hashimoto trajectory 5.

3.3 PPN simulations using a Supernova type Ia model

3.3.1 Supernova type Ia model

The Supernova type Ia explosion model is a two-dimensional delayed detonation model, described in detail by Kasen et al. [100] and Travaglio et al. [37]. A White Dwarf accretes material from a main-sequence or evolved companion star until it reaches the Chandrasekhar mass and explodes in a Supernova type Ia. The stellar simulation starts with the onset of the explosion and considers only the reactions relevant for the energy production. The nucleosynthesis with a full reaction network is calculated in a post-processing step. 51,200 tracer particles are distributed uniformly over the white dwarf star and record the evolution of temperature and density (see [37] and [101] for a detailed description of the tracer particle method). 4,624 of these tracers experience temperatures in the range relevant to the production of the p-nuclei. These tracers represent a total mass of 0.127 $M_\odot$, a single tracer accounts for $2.75 \cdot 10^{-5}$ $M_\odot$ [53]. All 4,624 tracer particles are ejected in the explosion.

3.3.1.1 Selection of tracers and aim of the study

Figure 3.16 shows the final abundances of the molybdenum isotopes as a function of maximum temperature of the corresponding tracer in the simulation of the Supernova type Ia model carried out by C. Travaglio [86]. The final abundances vary by 10 to 15 orders of magnitude in the temperature range presented. For a given maximum temperature, the spread in abundances of one isotope is up to 5 orders of magnitude. The current study aims at understanding the different final abundances of ^{92}Mo and ^{94}Mo, respectively, for tracers with the same maximum temperatures. Five tracers were selected from the set, see table 3.3.

Tracer	Abundance study	T_{max} (GK)	Comment
1	^{92}Mo	3.2	maximum abundance of ^{92}Mo
2	^{92}Mo	3.2	minimum abundance of ^{92}Mo
3	^{94}Mo	2.8	maximum abundance of ^{94}Mo
4	^{94}Mo	2.8	minimum abundance of ^{94}Mo
5	^{94}Mo	3.0	abundance of ^{94}Mo drops for tracers with $T_{\mathrm{max}} \gtrsim 2.9$ GK

Table 3.3.: Tracers selected for the PPN simulations using a Supernova type Ia model.

Two tracers were chosen from the set of tracers with a maximum temperature of 2.8 GK: Tracer-1 produces most ^{92}Mo, Tracer-2 produces least ^{92}Mo. The same criteria were applied for the selection of tracers to study the production of ^{94}Mo. Tracer-3 and Tracer-4 both show a maximum temperature of 3.2 GK. An additional tracer is taken from the set for ^{94}Mo as the abundance drops at peak temperatures higher than 2.9 GK (green markers in Figure 3.16). A tracer with $T_{\max} \approx 3.0$ GK is chosen, Tracer-5.

3.3.1.2 Temperature profiles of the selected tracers

Figure 3.17 shows the temperature profiles of the five selected tracers. The upper plot displays a time range starting shortly before the temperature of one tracer rises until the temperatures of all tracers drop below 1 GK. The lower plot shows a detailed view of the high temperature phases.

The temperature in Tracer-1 rises quickly to the maximum of 3.2 GK and then decreases slowly. The profile shows two further peak structures, a small peak at about $t = 1.1$ s and a larger peak at about $t = 1.35$ s.

The temperature of Tracer-2 rises and oscillates between the base level and about 0.5 GK. After $t = 0.5$ s it decreases until it rises again at $t \approx 0.7$ s. The temperature reaches 1 GK and fluctuates. Then it rises further and oscillates around 2.5 GK before reaching the maximum of 3.2 GK. The falling slope shows a continuously fluctuating structure.

Tracer-3 is similar to Tracer-1. The temperature increases steeply up to the maximum of 2.8 GK and then decreases exponentially. About 0.2 s later a second peak is reached with a local maximum of about 1.5 GK.

Like in Tracer-2, the temperature of Tracer-4 fluctuates around 0.5 GK in the time range from 0.3 s to 0.5 s. It decreases back to the base level until about 0.9 s. The temperature rises again and oscillates around 0.7 GK. It increases to the maximum temperature of 2.8 GK and then falls quickly to about 2.5 GK. The period of time above 2.5 GK is only about a fourth that of Tracer-3. The exponential decrease is slower than in Tracer-3 and the tracer exhibits several more peak structures.

The temperature profile of Tracer-5 resembles Tracer-3. It increases steeply to the maximum value of 3.0 GK and then drops exponentially. The profile shows a second peak about 0.1 s after the maximum with about 2.4 GK and another small peak at about $t = 1.2$ s.
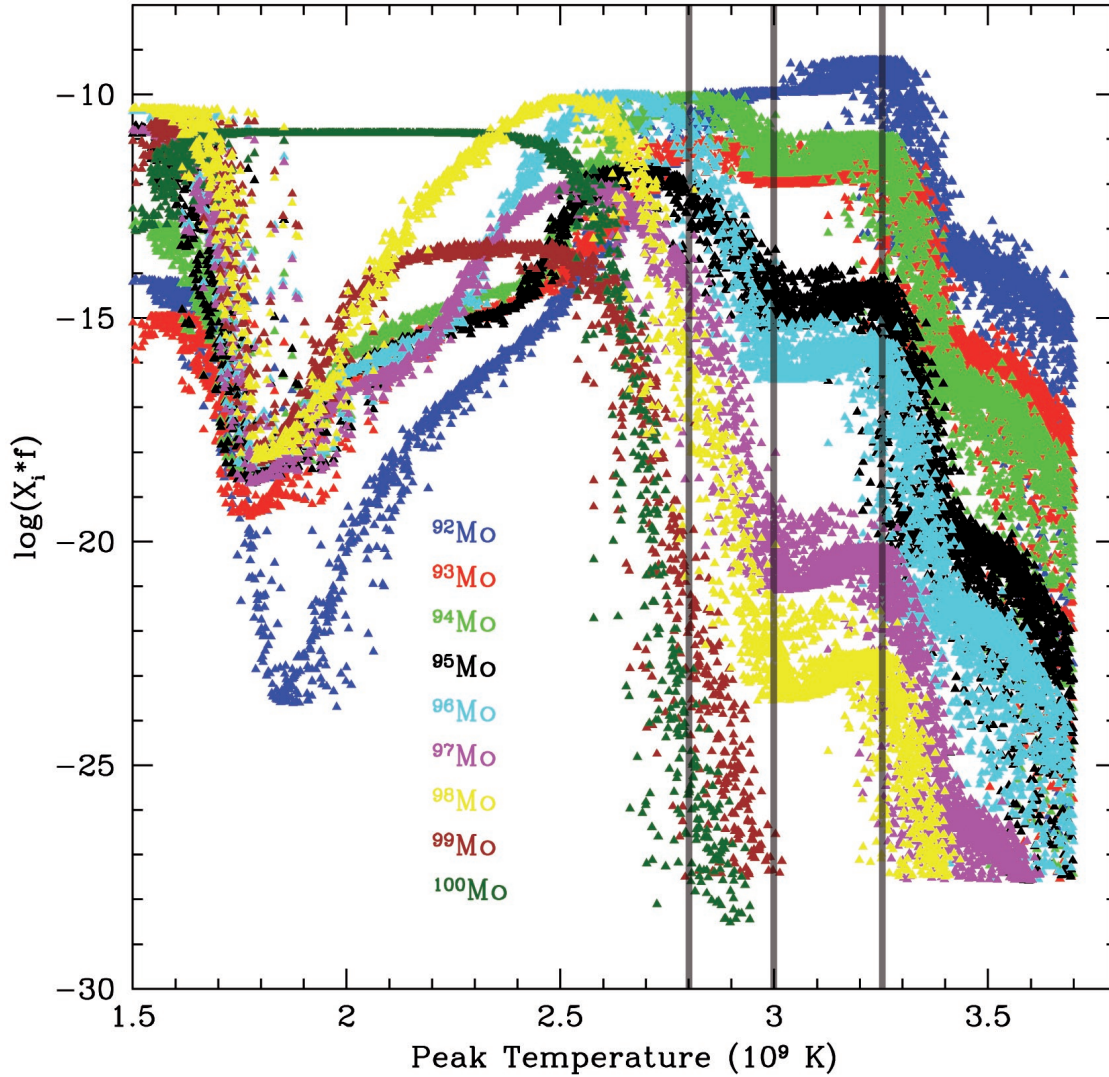
Figure 3.16.: Abundances of the molybdenum isotopes obtained from the nucleosynthesis simulation using a Supernova type Ia model vs. maximum temperature of the corresponding tracer. Each marker represents one tracer. The gray lines mark the tracer sets with a certain maximum temperature from which the tracers were chosen for the current study. Data and figure provided by C. Travaglio [86].
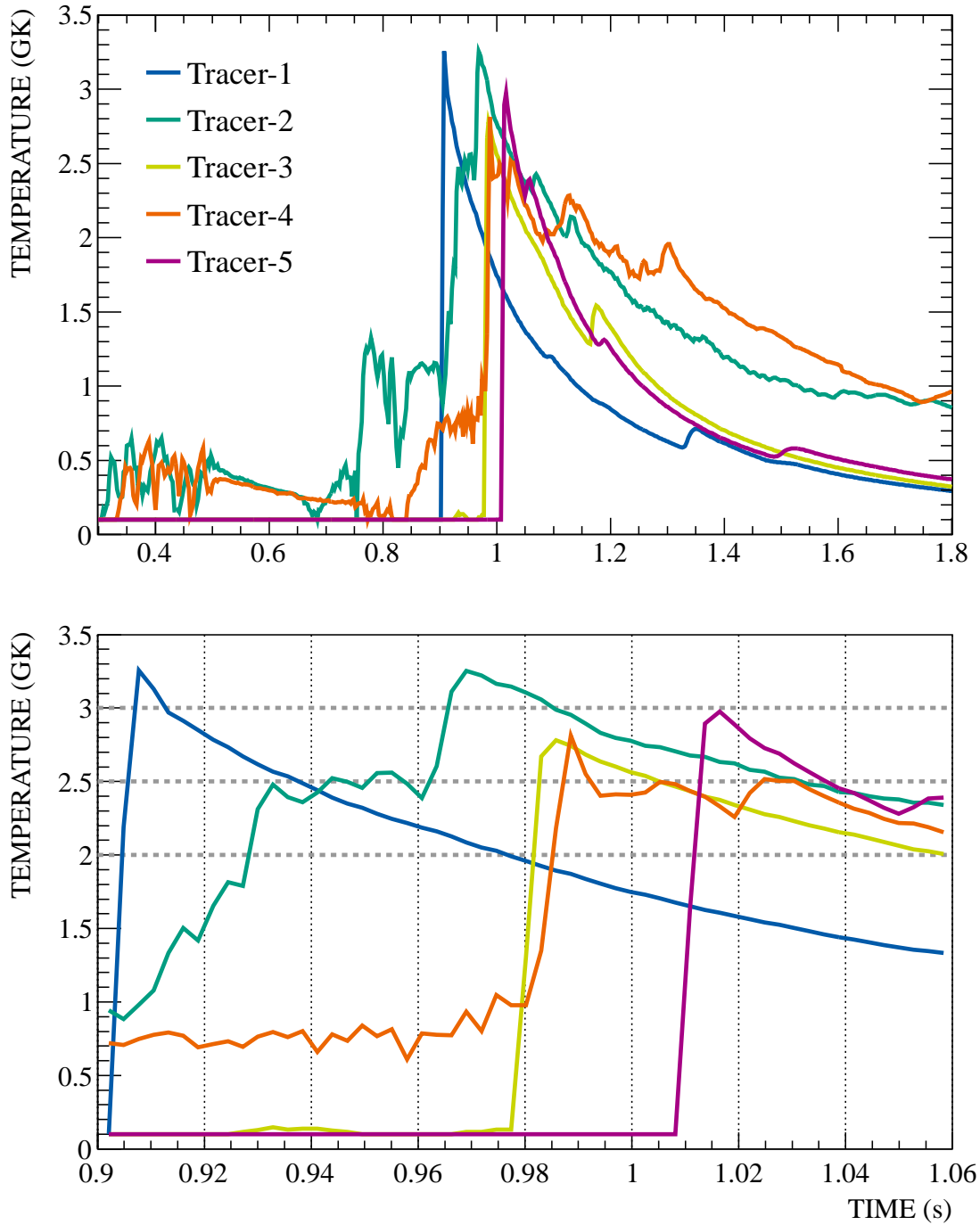
Figure 3.17.: Temperature profiles of the selected tracers from Supernova type Ia model. See text and table 3.3 for a detailed description.

3.3.2 Reaction libraries

The impact of the reaction rate sets Basel reaction library (last updated on January 20, 2009) [44, 89] and JINA Reaclib Database V1.1 [45] on the final mass fractions is studied in PPN simulations of a Supernova type Ia model. The results are compared to Travaglio's simulations with Basel reaction library (2009) [86].

In general, an agreement between the results obtained with different reaction libraries or post-processing codes is desirable. However, differences between the results with different reaction libraries are expected due to possible strong influences of single reaction rates. Each post-processing code applies its own numerical solver, which may also give different results, although the same reaction library is used.
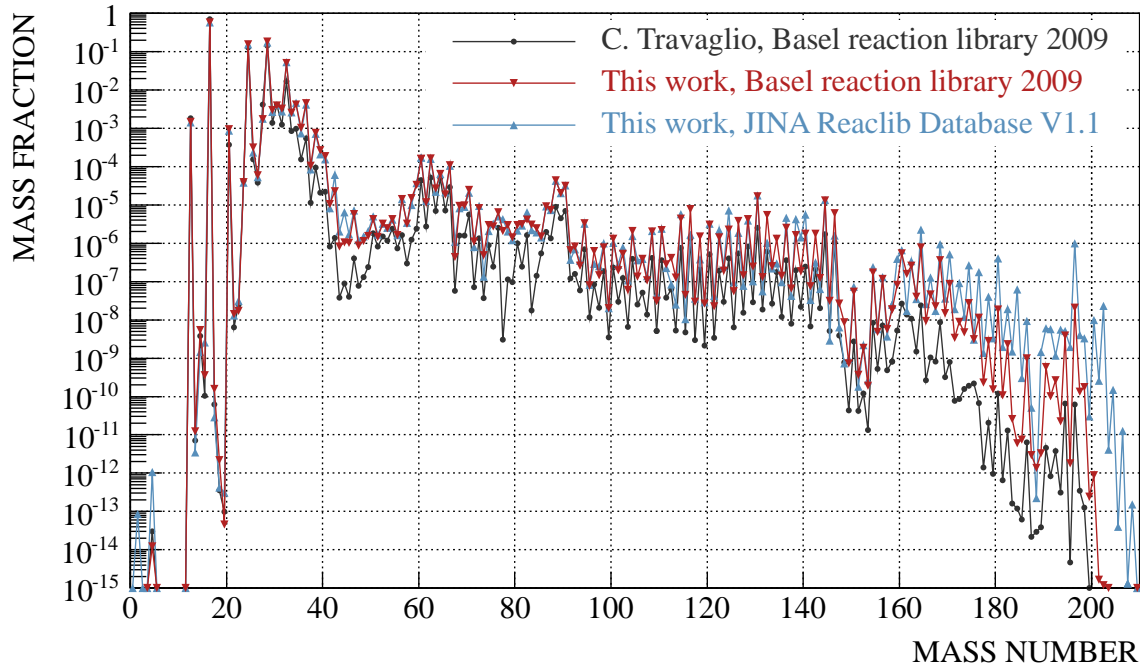
Figure 3.18.: Final mass fractions as function of mass number *A* for Tracer-3 in the simulation of a Supernova type Ia model. Gray circles: data provided by Claudia Travaglio, Basel reaction library. Red triangles down: PPN simulation using Basel reaction library. Blue triangles up: PPN simulation using JINA Reaclib Database V1.1.

Figure 3.18 shows the final mass fractions as a function of mass number *A* for Tracer-3. The PPN simulations give higher yields for the isotopes with *A* > 30, whereas Travaglio's simulations produce more isotopes in the C-O-region. The general trends are in good agreement,

except for the mass numbers between 40 and 50, 75 and 85, as well as 170 and 175. In the mass range above 180, the abundances obtained from the simulations differ by orders of magnitudes. PPN simulations using Basel reaction library produce more isotopes in the $110 < A < 150$ mass region and less in the $A > 150$ mass region compared to the results using JINA Reaclib Database.

Figure 3.19 shows the final mass fractions for the Mo isotopes in Travaglio's simulations of a Supernova type Ia model and in the PPN simulations with Basel reaction library and JINA Reaclib Database for Tracer-1. The yields in the PPN simulations are about one order of magnitude higher than in Travaglio's simulations, but the production trends across the isotopic chain are in good agreement. The mass fractions of the heaviest isotopes in the chain obtained in the PPN simulation with Basel reaction library agree better with Travaglio's results than the results from JINA Reaclib Database. In the following, this work uses Basel reaction library.
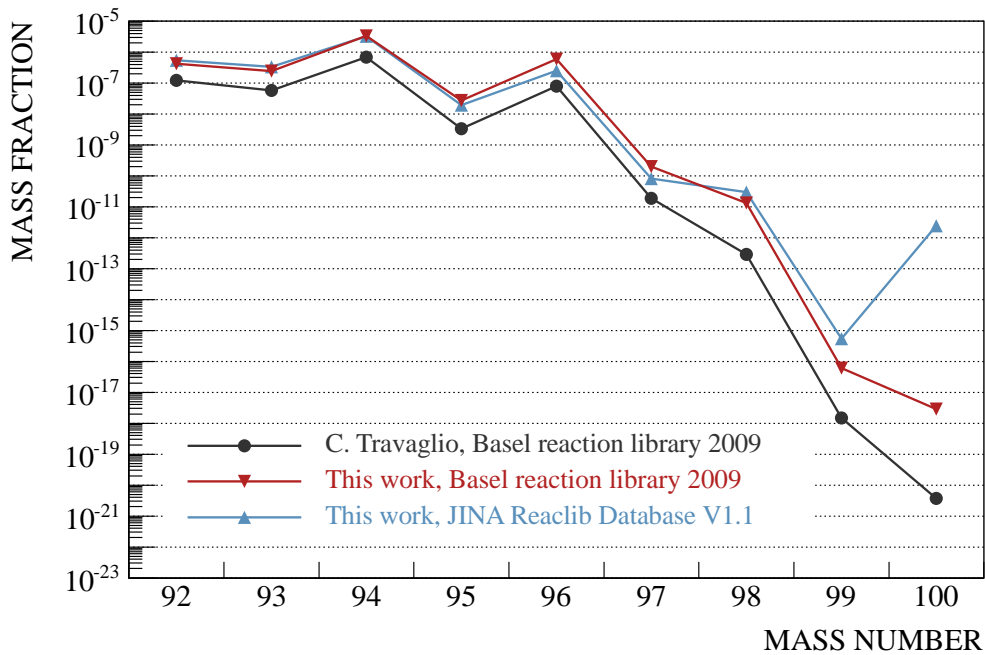
Figure 3.19.: Final mass fractions for the Mo isotopes for Tracer-3 in the simulations of a Supernova type Ia model. Black circles: Travaglio's simulations using Basel reaction library. Red triangles down: PPN simulations using Basel reaction library. Blue triangles up: PPN simulations using JINA Reaclib Database V1.1.

3.3.3 Production and destruction of ^{92}Mo and ^{94}Mo

3.3.3.1 The case of ^{92}Mo

Figure 3.20 shows the relative time-integrated production and destruction fluxes of ^{92}Mo for Tracer-1 and Tracer-2. The γ-induced reactions form the main production paths. For Tracer-1, neutron-dissociation reactions starting from heavier Mo isotopes account for about half of the production fluxes. The isotope ^{92}Mo is mainly destroyed by proton-dissociation reactions. The isotope shows a net production flux of 20%. For Tracer-2, the neutron-dissociation reactions producing ^{92}Mo as well as proton-dissociation reactions depleting ^{92}Mo make up a larger fraction of the fluxes than in Tracer-1. The sum of destruction fluxes gives about 98%, which results in a net production flux of ^{92}Mo of only about 2%.
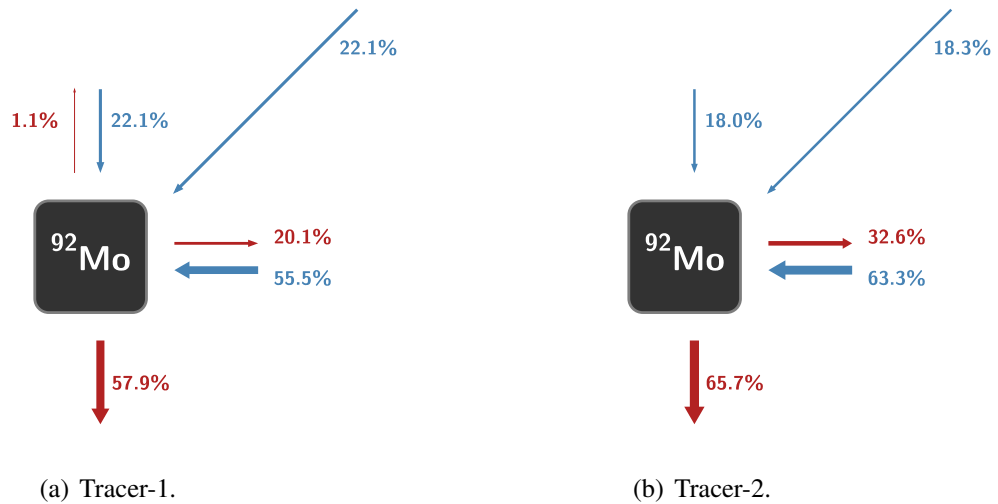

(a) Tracer-1. (b) Tracer-2.

Figure 3.20.: Relative time-integrated fluxes producing (blue) and destroying (red) the p-nucleus ^{92}Mo for Tracer-1 and Tracer-2 in the post-processing nucleosynthesis simulation of the Supernova type Ia model. The sum of all production fluxes is normalized to 100% for each isotope, and the destruction fluxes are scaled with the same factor. Fluxes smaller than 1% are not shown.

Figures 3.21 and 3.22 show the mass fractions of the molybdenum isotopes as a function of time for Tracer-1 and Tracer-2. The following discussion focuses on the isotope ^{92}Mo; additional information for other Mo isotopes supports the discussion. To identify the relevant reactions in different phases of the tracers, Figures 3.23 and 3.24 show the nucleosynthesis fluxes for different time ranges in the simulations, which are marked in Figures 3.21 and 3.22.

In Tracer-1, the isotope ^{92}Mo is at first destroyed by neutron-capture reactions when the temperature rises (compare Figures 3.21 and 3.23 (a)). When the temperature reaches about 2 GK, other reactions producing and destroying ^{92}Mo set in (Figure 3.23 (b)). Besides the reactions shown in Figure 3.20, the reactions ^{91}Nb(p,γ), ^{91}Mo(n,γ), ^{95}Ru(n,α), ^{92}Mo(p,γ), ^{92}Mo(γ,n), ^{92}Mo(p,γ), and ^{92}Mo(n,p) account for a small fraction of the nucleosynthesis fluxes about two orders of magnitude lower than the maximum fluxes. The mass fraction of ^{92}Mo increases to its maximum and final value up to the point when the peak temperature is reached.
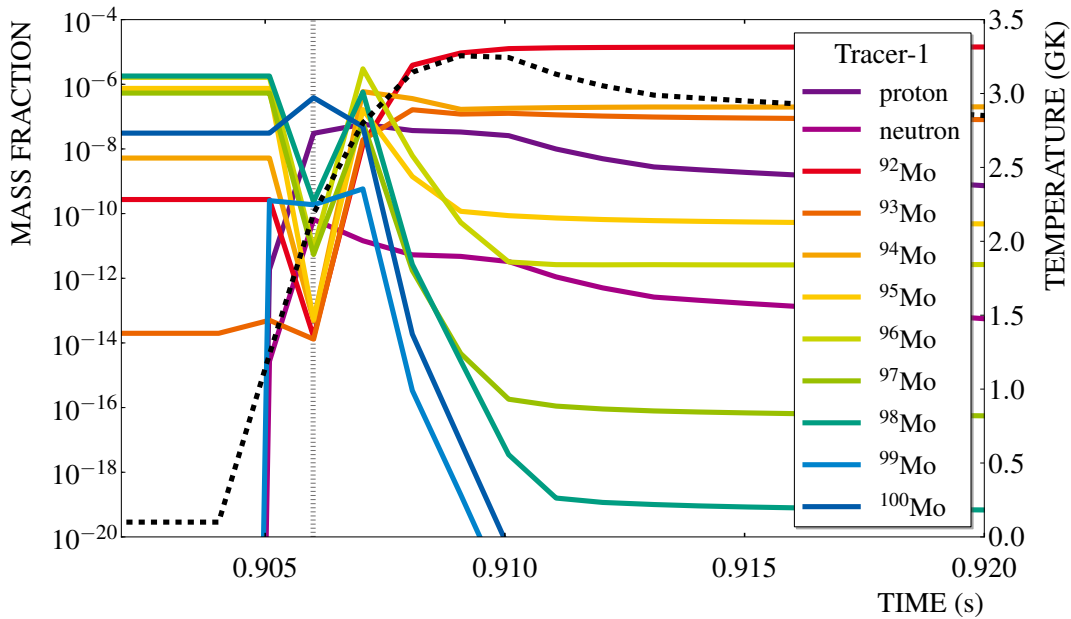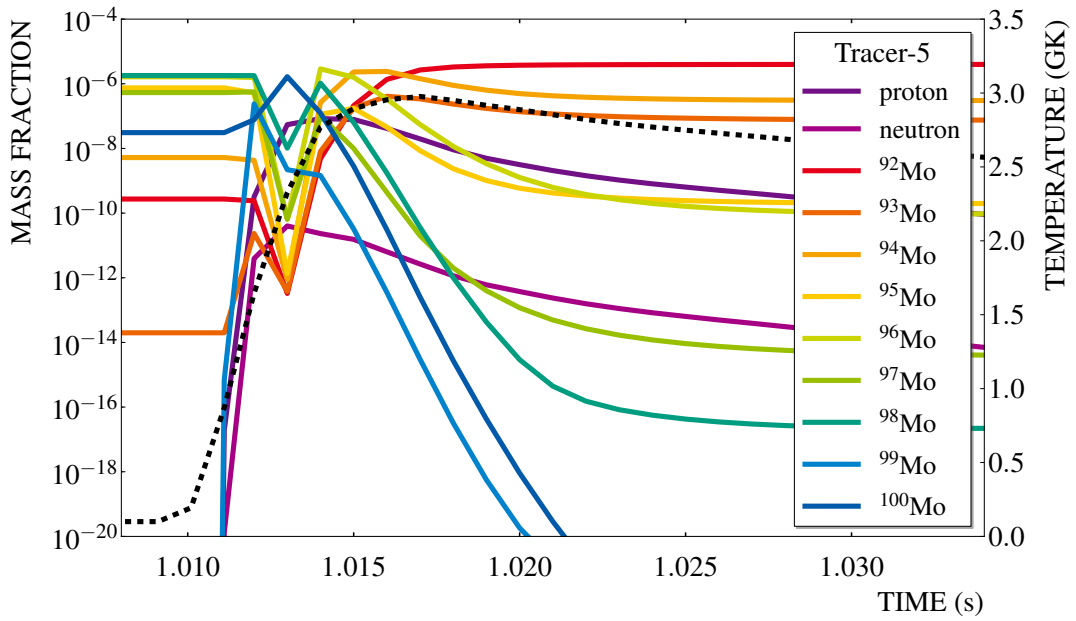

Figure 3.21.: Mass fractions of the molybdenum isotopes for Tracer-1 in the PPN simulation of the Supernova type Ia model. Black dashed line: temperature profile of the tracer.

As in Tracer-1, neutron-capture reactions destroy the p-nucleus ^{92}Mo up to about $t = 0.929$ s in Tracer-2 (Figures 3.22 and 3.24 (a)). The temperature rises further and fluctuates around 2.5 GK. In this time range, the reactions ^{91}Nb(p,γ), ^{92}Nb(p,n) and ^{93}Mo(γ,n) produce ^{92}Mo (Figure 3.24 (b)). When the temperature increases up to 3.2 GK, ^{92}Mo is produced by the same reactions as in the high temperature phase of Tracer-1 (compare Figures 3.23 (b) and 3.24 (b)).

The mass fraction of ^{92}Mo decreases about an order of magnitude after the maximum temperature is reached. The final mass fractions of all molybdenum isotopes are one to three orders of magnitude lower than in Tracer-1 (compare Figures 3.21 and 3.22). The high temperature phase above 3.0 GK of Tracer-2 is about four times longer than for Tracer-1. Photon-induced

reactions destroy the Mo isotopes in this phase. Neutron-dissociation reactions lead to ^{92}Mo at the neutron shell closure where the destruction path continues via proton-dissociation reactions. When the mass fractions of the heavier Mo isotopes decrease, the abundance of ^{92}Mo cannot be fed by neutron-dissociation reactions anymore (Figure 3.20). The final mass fraction of ^{92}Mo is therefore lower than in Tracer-1.
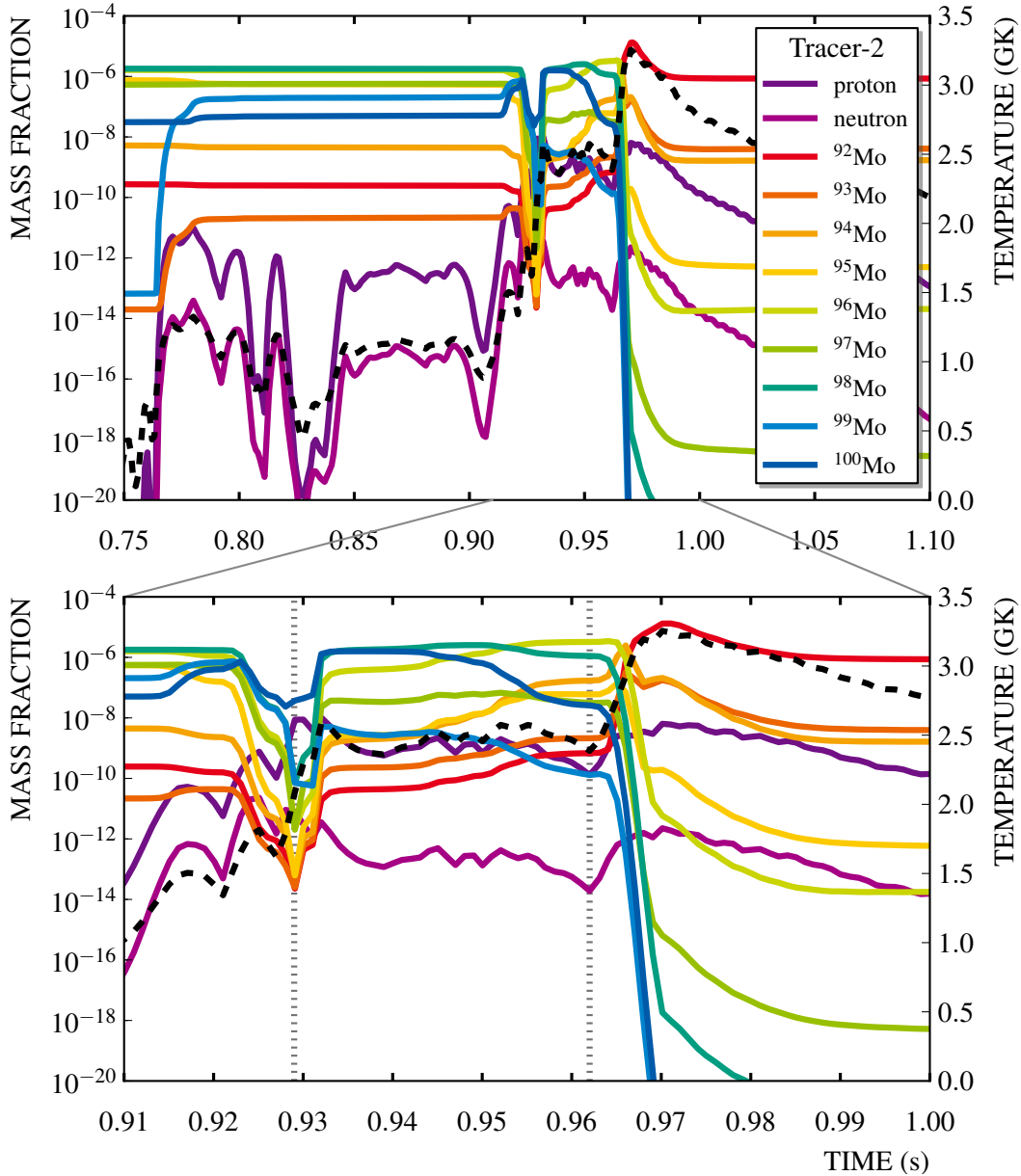
Figure 3.22.: Same as Figure 3.21, for Tracer-2.

(a) Time range 0.0 s to 0.906 s for Tracer-1.

(b) Time range 0.906 s to end for Tracer-1.

(c) Full time range of Tracer-1.
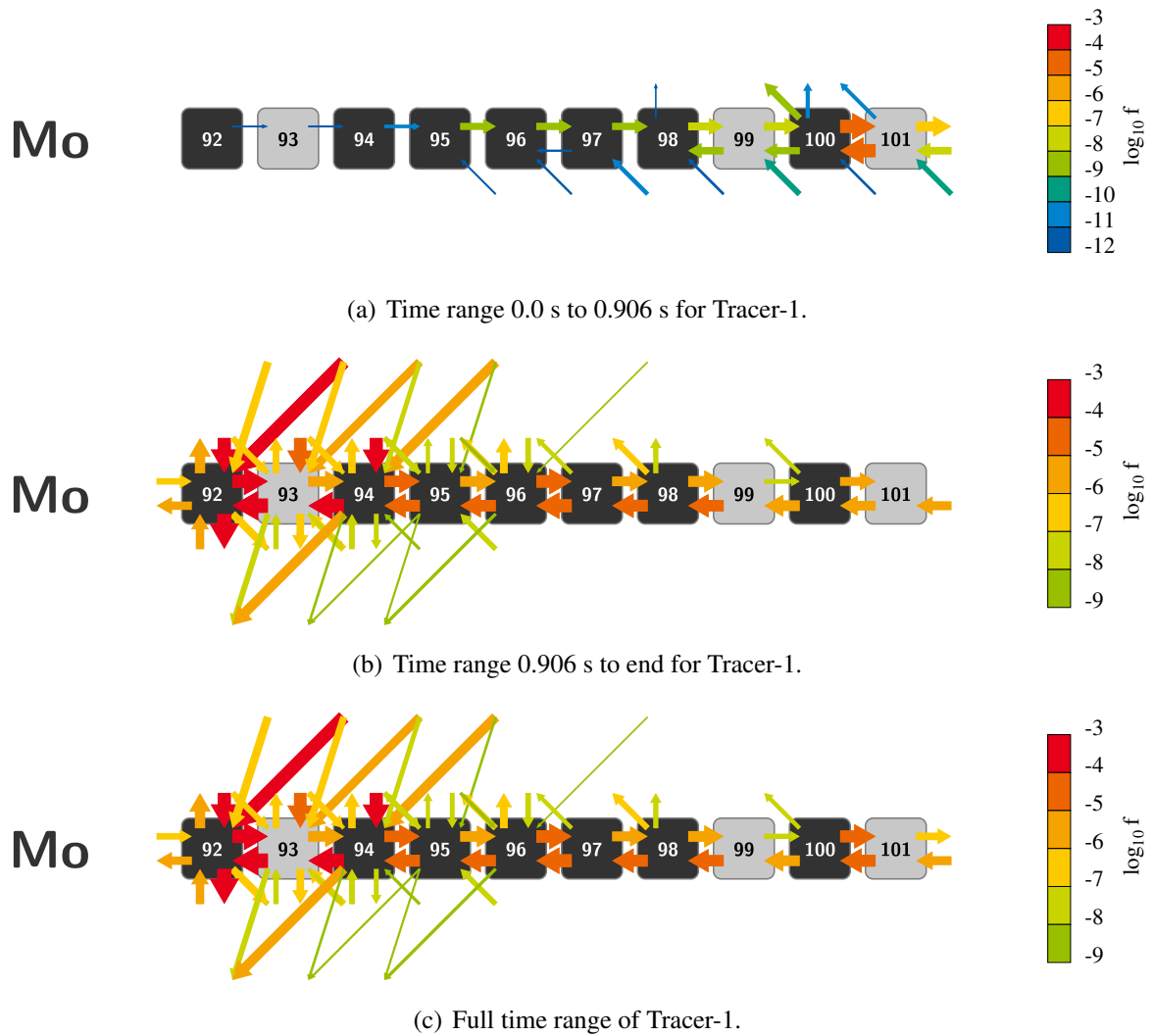
Figure 3.23.: Time-integrated nucleosynthesis fluxes producing and destroying the Mo isotopes for Tracer-1 in the PPN simulation of the Supernova type Ia model. Colors indicate the order of magnitude of the flux, the arrow thicknesses scale linearly with $\log_{10} f$.

(a) Time range 0.0 s to 0.929 s for Tracer-2.

(b) Time range 0.929 s to 0.962 s for Tracer-2.

(c) Time range 0.962 s to end for Tracer-2.

(d) Full time range of Tracer-2.
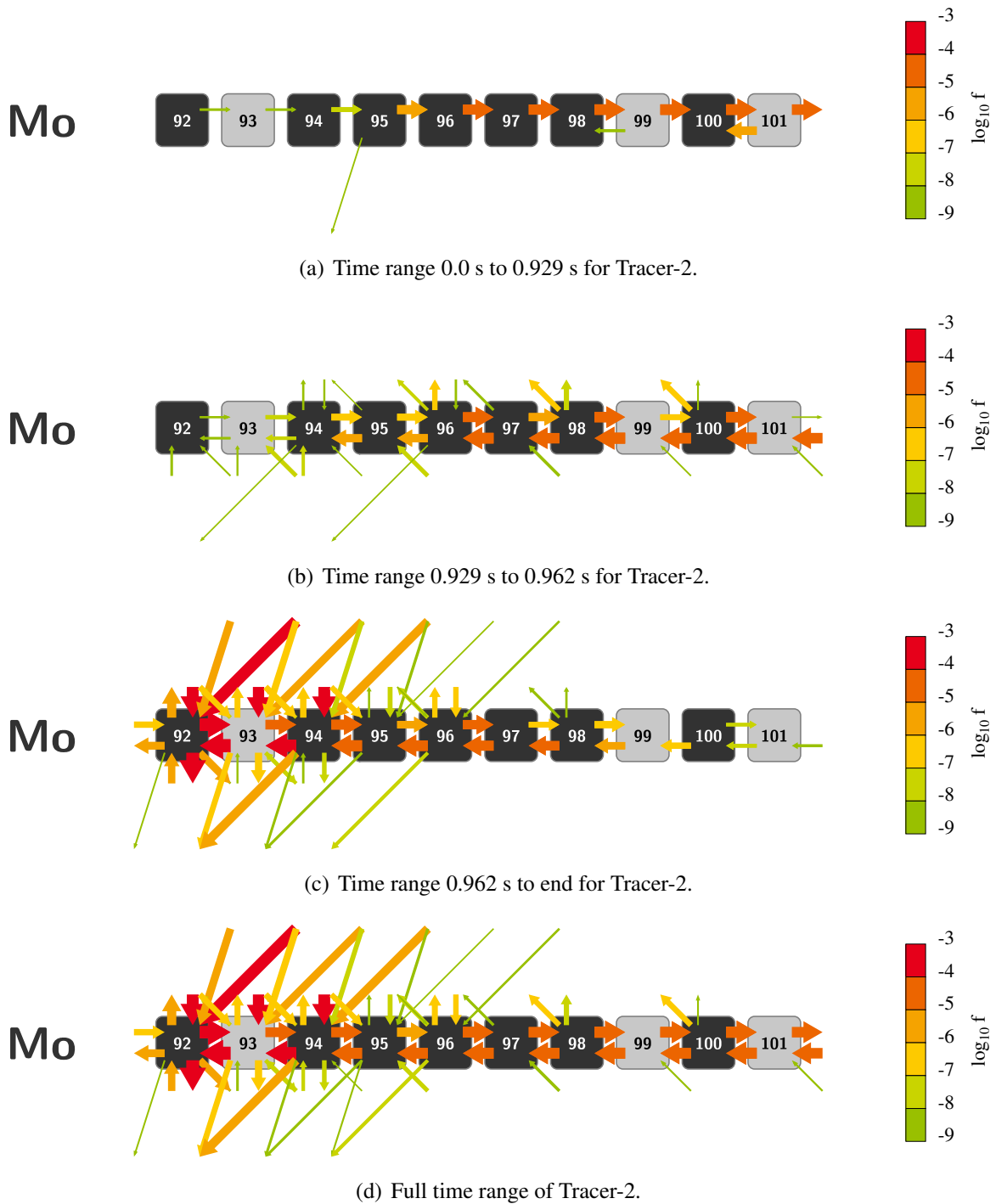
Figure 3.24.: Same as Figure 3.23, for Tracer-2.

3.3.3.2 The case of ^{94}Mo

Figure 3.25 shows the nucleosynthesis fluxes producing and destroying ^{94}Mo in Tracer-3 and Tracer-4. Neutron-dissociation reactions starting from heavier Mo isotopes are the main production paths accounting for about 93% of the production fluxes for Tracer-3 and for about 96% for Tracer-4. Neutron-capture and proton-dissociation reactions make up a few percent of the production for Tracer-3. In Tracer-4, only neutron-capture reactions produce a relevant fraction of ^{94}Mo. The destruction fluxes add up to about 63% for both tracers.
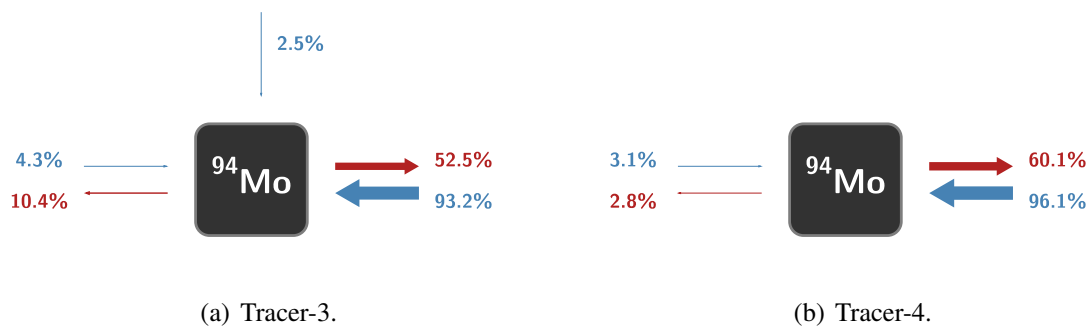
(a) Tracer-3. (b) Tracer-4.

Figure 3.25.: Relative time-integrated fluxes producing (blue) and destroying (red) the p-nucleus ^{94}Mo for Tracer-3 and Tracer-4 in the PPN simulation of the Supernova type Ia model. The sum of all production fluxes is normalized to 100% for each isotope, and the destruction fluxes are scaled with the same factor. Fluxes smaller than 1% are not shown.

The mass fractions of the molybdenum isotopes in the simulation of Tracer-3 and Tracer-4 are plotted as a function of time in Figures 3.26 and 3.27. The following discussion focuses on the isotope ^{94}Mo; additional information for other Mo isotopes supports the discussion. The nucleosynthesis fluxes for several time ranges of the simulations, which are marked in Figures 3.26 and 3.27, are shown in Figures 3.28 and 3.29.

At first, the stable molybdenum isotopes are destroyed by neutron-capture reactions shifting the mass to higher mass isotopes in the chain (Figures 3.28 (a) and 3.29 (a)). When the temperature of Tracer-3 increases above about 2.3 GK, the light molybdenum isotopes ^{92}Mo, ^{93}Mo and ^{94}Mo are produced by neutron-dissociation reactions starting from heavier Mo isotopes, which are destroyed by orders of magnitude in return (Figures 3.26 and 3.28 (b)). Furthermore, (γ,α) reactions on stable Ru isotopes produce the isotopes ^{92}Mo, ^{94}Mo and ^{96}Mo.

Tracer-4 produces the light Mo isotopes from ^{92}Mo to ^{96}Mo in the high temperature phase while the heavier Mo isotopes are destroyed at the same time (Figure 3.27). Compared to Tracer-3, the mass fractions of ^{97}Mo to ^{100}Mo only decrease by about an order of magnitude.

The nucleosynthesis fluxes between the light Mo isotopes are lower and the production, and destruction fluxes due to (γ,α) and (n,α) reactions are less prominent than in Tracer-3 (compare Figures 3.28 (b) and 3.29 (b)).

^{94}Mo is produced by neutron-dissociation reactions when the temperature is higher than about 2.3 GK. The reaction chain starts from the heavier Mo isotopes. If the high temperature phase is long (Tracer-3), the disintegration reactions shift the mass fractions to the proton-rich side of the Mo isotopes. If the high temperature phase is short (Tracer-4), only a small fraction of the heavy Mo isotopes is disintegrated. Therefore, Tracer-4 produces a smaller final mass fraction of ^{94}Mo than Tracer-3.
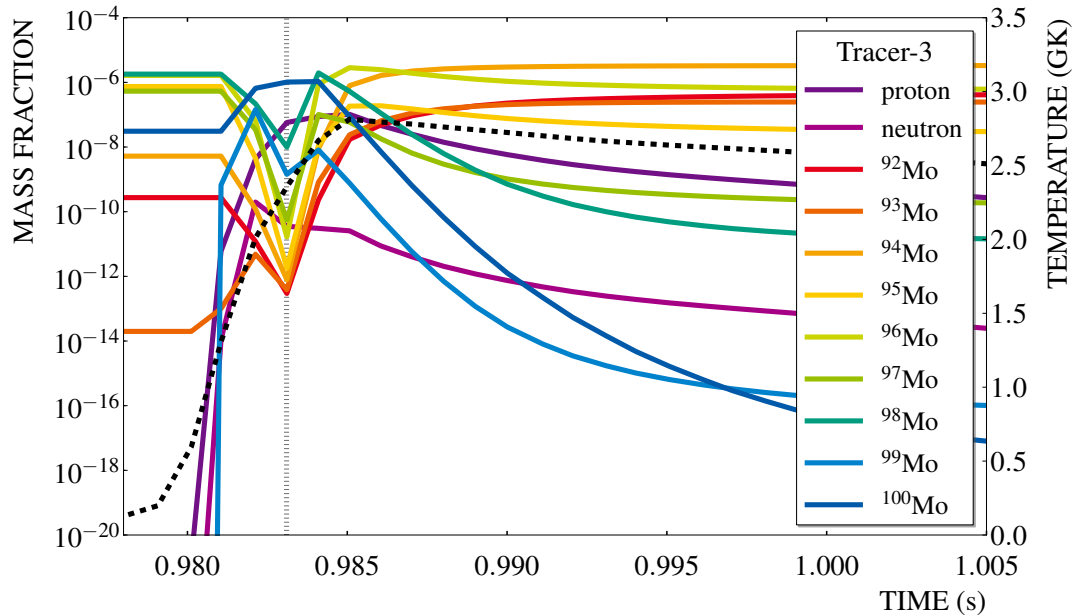
Figure 3.26.: Mass fractions of the molybdenum isotopes for Tracer-3 in the PPN simulation of Supernova type Ia model. Black dashed line: temperature profile of the tracer.
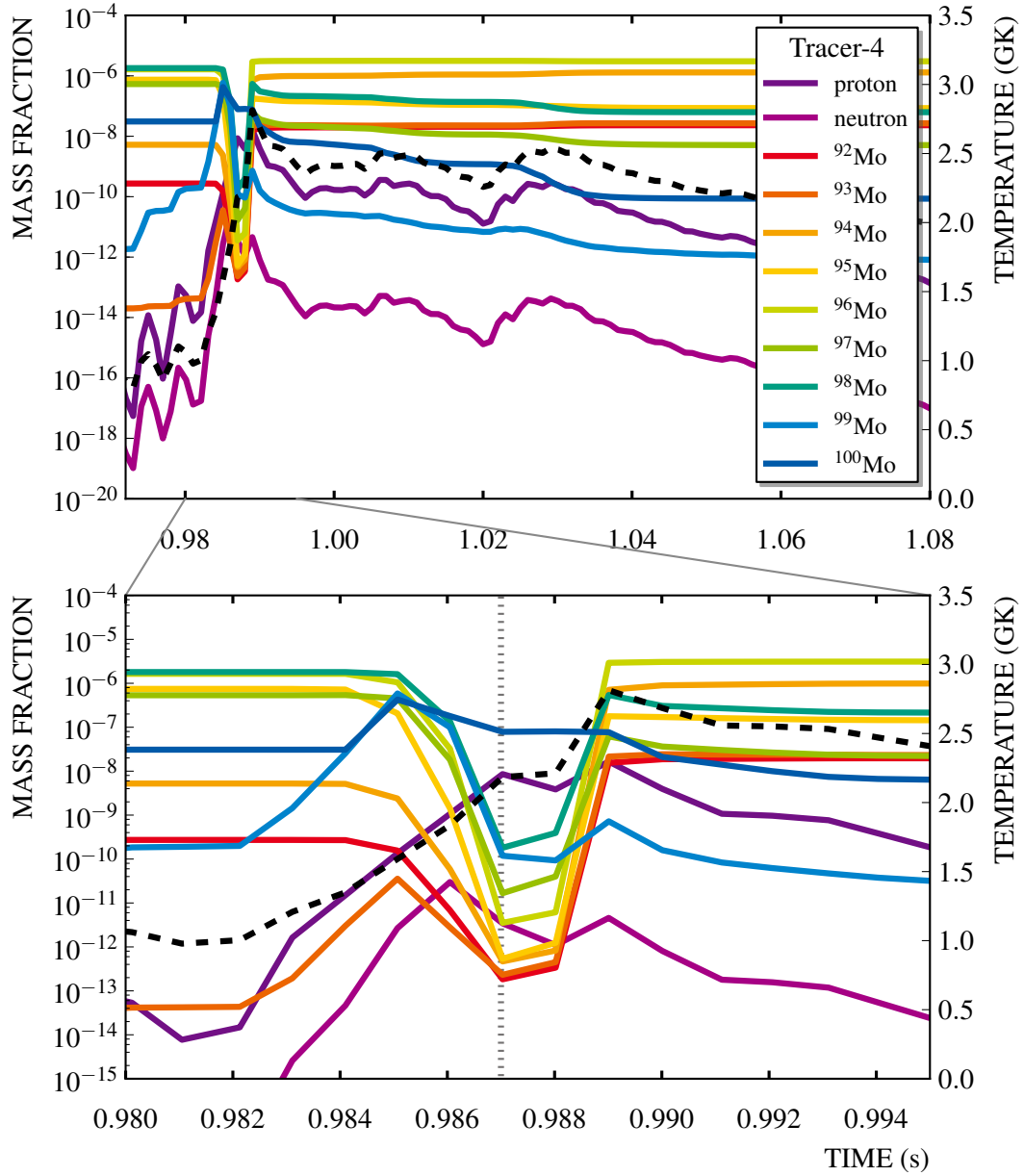
Figure 3.27.: Mass fractions of the molybdenum isotopes for Tracer-4 in the PPN simulation of Supernova type Ia model. Black dashed line: temperature profile of the tracer.

(a) Time range 0.0 s to 0.983 s for Tracer-3.

(b) Time range 0.983 s to end for Tracer-3.

(c) Full time range of Tracer-3.
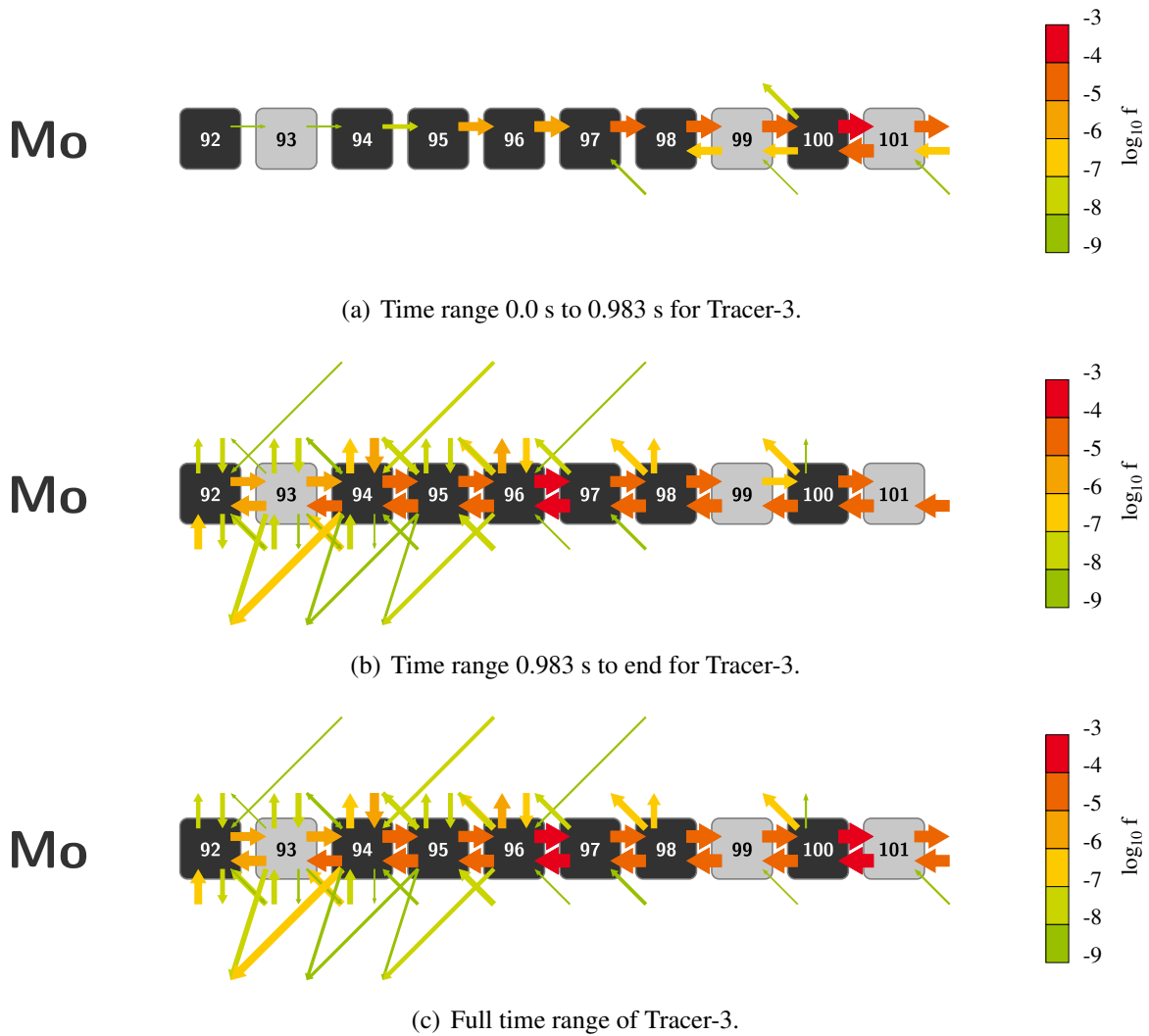
Figure 3.28.: Time-integrated nucleosynthesis fluxes producing and destroying the Mo isotopes for Tracer-3 in the PPN simulation of the Supernova type Ia model. Colors indicate the order of magnitude of the flux, the arrow thicknesses scale linearly with $\log_{10} f$.

(a) Time range 0.0 s to 0.987 s for Tracer-4.

(b) Time range 0.987 s to end for Tracer-4.

(c) Full time range of Tracer-4.
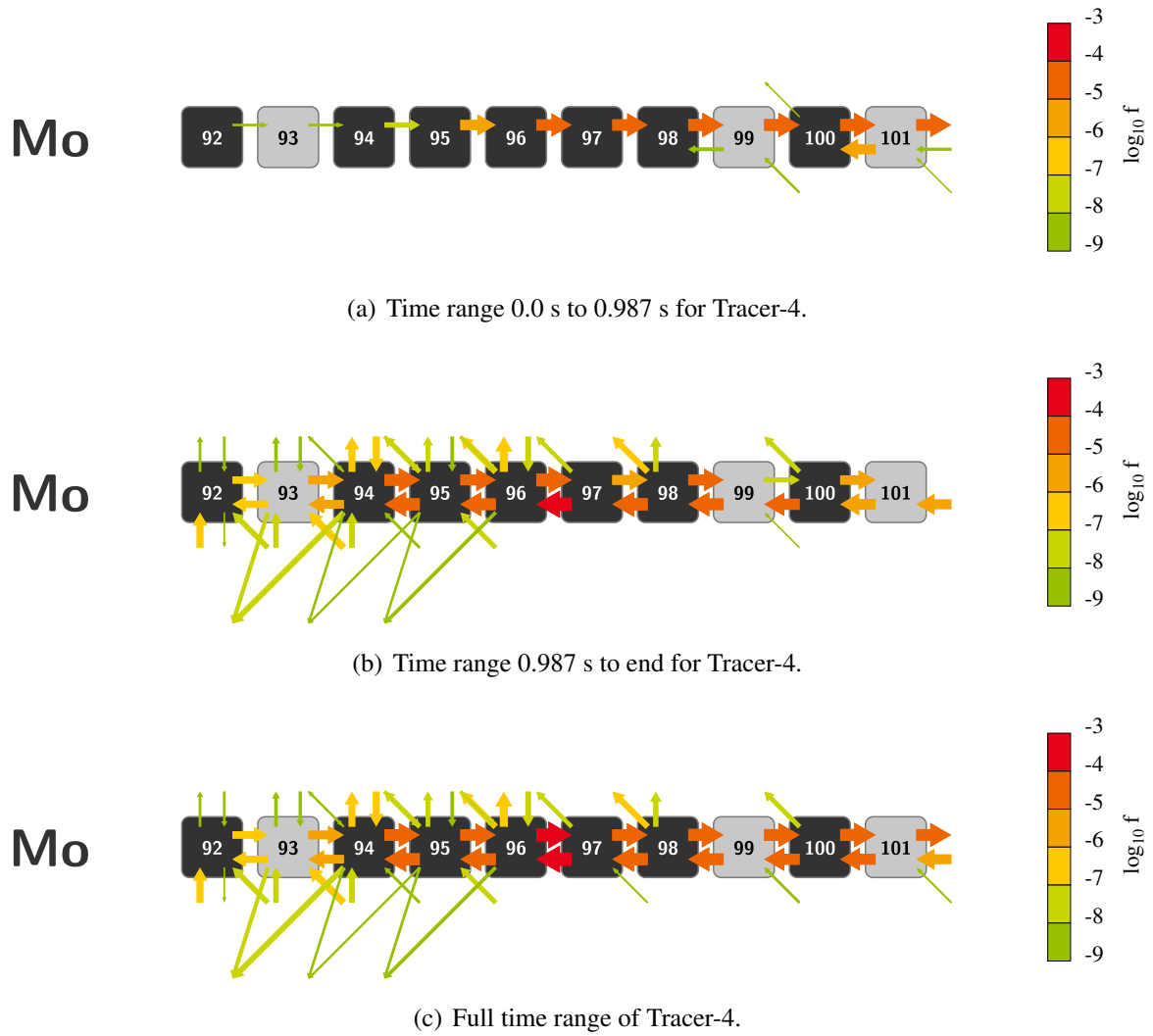
Figure 3.29.: Same as Figure 3.28, for Tracer-4.

Tracer-5 is selected from a set of tracers with a maximum temperature of about 3.0 GK. The temperature profile resembles that of Tracer-3. It is shifted to higher temperatures, therefore, the high temperature phase above 2.5 GK is longer than in Tracer-3.

Figure 3.30 shows the relative time-integrated fluxes producing and destroying ^{94}Mo in Tracer-5. Neutron-dissociation reactions mainly produce ^{94}Mo, while neutron-capture and proton-dissociation reactions represent a small fraction of the production fluxes. The p-nucleus ^{94}Mo is about equally destroyed by neutron-dissociation and neutron-capture reactions. A small fraction of the destruction fluxes is formed by (γ,α) reactions.
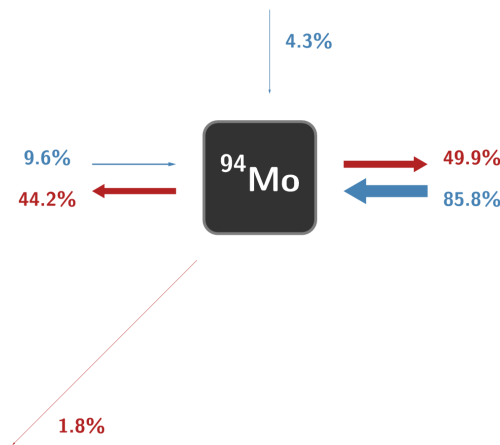
Figure 3.30.: Relative time-integrated fluxes producing (blue) and destroying (red) the p-nucleus ^{94}Mo for Tracer-5 in the PPN simulation of the Supernova type Ia model. The sum of all production fluxes is normalized to 100% for each isotope, and the destruction fluxes are scaled with the same factor. Fluxes smaller than 1% are not shown.

The mass fractions of the Mo isotopes as a function of time are plotted in Figure 3.31. In the time range with $T > 2.3$ GK, the ^{94}Mo mass fraction increases at first. The mass fraction starts to decrease again before the maximum temperature is reached and until the temperature drops below about 2.3 GK. At the same time, the mass fraction of ^{92}Mo increases. The p-nucleus ^{92}Mo is produced by neutron-dissociation reactions starting from ^{94}Mo and heavier Mo isotopes.

Figure 3.32 shows the nucleosynthesis fluxes of the molybdenum isotopes for Tracer-5. More reactions are relevant for the production and destruction of the light Mo nuclei due to the higher temperature than in Tracer-3. The isotope ^{94}Mo is stronger destroyed by γ-induced reactions. Neutron-dissociation reactions lead to the lightest stable Mo isotope ^{92}Mo. The isotope ^{92}Mo is destroyed by proton-dissociation reactions. The inverse flow via neutron-capture reactions is therefore less prominent than in Tracer-3.

Figure 3.31.: Mass fractions of the molybdenum isotopes for Tracer-5 in the PPN simulation of Supernova type Ia model. Black dashed line: temperature profile of the tracer. The profile of Tracer-5 is similar to Tracer-3, but shows a higher maximum temperature.
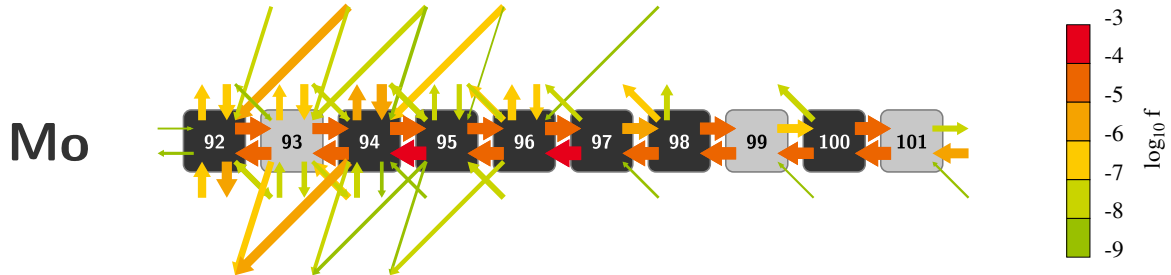
Figure 3.32.: Time-integrated nucleosynthesis fluxes producing and destroying the Mo isotopes for Tracer-5 in the PPN simulation of the Supernova type Ia model. Colors indicate the order of magnitude of the flux, the arrow thicknesses scale linearly with $\log_{10} f$.

3.3.3.3 Conclusion

The maximum temperatures and the duration of the high temperature phases determine the final mass fraction of ^{92}Mo and ^{94}Mo. Photon-induced reactions destroy the heavy Mo isotopes in the high temperature phase. The higher the maximum temperature, the further the masses are shifted towards the proton-rich nuclei in the isotopic chain.

The isotope ^{94}Mo is produced by neutron-dissociation reactions on heavier Mo isotopes when the temperature rises above about 2.3 GK. The longer the temperature phase between 2.3 and 2.7 GK lasts, the more ^{94}Mo is produced. At higher temperatures, ^{94}Mo is efficiently destroyed, and ^{92}Mo at the neutron shell closure is produced.

Neutron-dissociation reactions on heavier Mo isotopes efficiently produce ^{92}Mo at temperatures above 3.0 GK. At the same time, ^{92}Mo is destroyed by proton-dissociation reactions. If the high temperature phase is long, the mass fractions of the heavier Mo isotopes decrease and the abundance of ^{92}Mo cannot be fed by neutron-dissociation reactions anymore. The longer the high temperature phase above 3.0 GK lasts, the lower is the final mass fraction of ^{92}Mo.

100

4   Summary and outlook

The origin of the p-nuclei, in particular of the light p-nuclei ^{92}Mo, ^{94}Mo, ^{96}Ru and ^{98}Ru, has been little understood so far. Many possible production sites are under discussion, however, nucleosynthesis simulations of these astrophysical environments fail to reproduce the p-nuclei abundances observed in the solar system. The nucleosynthesis simulations rely on information about the seed abundance distributions, the nuclear reaction network and the astrophysical environment.

This work addressed the nuclear data input. The key reaction ^{94}Mo(γ,n) for understanding of the production ratio of the p-nuclei ^{94}Mo and ^{92}Mo was measured by Coulomb dissociation at the LAND setup at GSI Helmholtzzentrum für Schwerionenforschung in Darmstadt, Germany. Post-processing nucleosynthesis simulations were carried out within the NuGrid research platform to investigate the production of the light p-nuclei ^{92}Mo, ^{94}Mo, ^{96}Ru and ^{98}Ru.

Measurement of the ^{94}Mo(γ,n) reaction by Coulomb dissociation

Coulomb dissociation experiments allow the study of photon-induced dissociation reactions in inverse kinematics. The nuclei impinge on a highly charged target and interact with a virtual photon of the time-varying, Lorentz-contracted electromagnetic field of the target nucleus. The complete kinematics of the reaction as well as the energy loss of the ions are measured by the detectors of the setup. This allows the unambiguous identification of all particles involved in the reaction. The method can be applied to unstable nuclei, which cannot be prepared as a sample for experiments using real photons.

The integral Coulomb dissociation cross section of the ^{94}Mo(γ,n) reaction was determined in a complex analysis. The systematic uncertainties were determined by systematic studies of the impact of data selection criteria on the cross section. An integral Coulomb dissociation cross section of $(571 \pm 14_{stat} \pm 46_{syst})$ mb was obtained for the neutron-dissociation reaction of ^{94}Mo for a beam energy of 500 AMeV. The same analysis was carried out for the isotope ^{100}Mo, the cross section of which had been determined previously by O. Ershova [48]. The independent analyses agree within the uncertainties.

The results obtained for the isotopes ^{100}Mo, ^{94}Mo and ^{92}Mo were compared with real photon experiments carried out at the Saclay linear accelerator by Beil et al. [49]. Previous measurements of photoabsorption cross section had shown discrepancies to Beil et al. Therefore, normalization factors of 0.8 to 0.88 had been proposed for photoabsorption cross sections measured at Saclay in the mass range of A = 85-93 [84]. O. Ershova confirmed the normalization factors in the analysis of the Coulomb dissociation of ^{100}Mo [48]. However, the ratios calculated for the proton-rich isotopes ^{94}Mo and ^{92}Mo were found to be lower than the expected ratios. The data showed a systematically increasing ratio from about 0.6 to 0.8 with increasing neutron numbers of the nuclei. Possible reasons for the disagreement will be investigated in the future.

The measurement of Coulomb dissociation reactions at the LAND setup suffers from large systematic uncertainties induced in particular by the neutron reconstruction algorithm of LAND. Currently, a new neutron detector NeuLAND is under construction, which will feature a high resolution and a high detection efficiency with up to 95% for one neutron and up to 60% for four neutrons in the outgoing reaction channel [102]. NeuLAND will be installed at the R^{3}B setup at the Facility for Antiproton and Ion Research in Europe GmbH, which is currently being built in Darmstadt, Germany. The R^{3}B setup will allow the kinematically complete measurements of reactions, such as Coulomb dissociation reactions, with relativistic heavy-ion beams of short-lived nuclei with beam energies up to about 1 AGeV [103].

Post-processing nucleosynthesis simulations for the p-process

The impact of the direct production and destruction reactions of the light p-nuclei ^{92}Mo, ^{94}Mo, ^{96}Ru and ^{98}Ru was investigated within the framework of a classical Supernova type II model with post-processing nucleosynthesis simulations. It was shown that the light p-nuclei are mainly produced via neutron-dissociation reactions on heavier nuclei in the isotopic chains. The higher the temperature of the astrophysical environment, the higher the fraction of production fluxes starting on nuclei of heavier elements than molybdenum and ruthenium. The final abundances of the light p-nuclei are determined by their main destruction reactions. Future systematic sensitivity studies of all reactions in the network could identify all reactions relevant for the production of the light p-nuclei.

The reaction rates for the nucleosynthesis simulations were calculated from JINA Reaclib Database. The corresponding parameters were obtained from fits of theoretical values, which were determined within the Hauser-Feshbach model. Future studies should include experimentally determined rates, which are only available for some of the important reactions and for the ground states of the corresponding nuclei. Data of energy-dependent cross sections close to the threshold of the reactions ^{92}Mo(γ,p), ^{94}Mo(γ,α), ^{96}Ru(γ,α), ^{96}Ru(γ,p),

^{96}Ru(γ,n), ^{98}Ru(γ,n) and ^{100}Pd(γ,α) are desirable to constrain the nucleosynthesis of the light p-nuclei. The inverse reactions ^{92}Mo(α,γ) and ^{96}Ru(α,γ) of the reactions ^{96}Ru(γ,α) and ^{100}Pd(γ,α) have been measured, which allows the calculation of the desired cross sections. The data are not yet included in the available reaction libraries. Future studies should consider these results.

For the first time tracers obtained from a two-dimensional Supernova type Ia model were post-processed with the NuGrid nucleosynthesis code and compared to previous results. The nucleosynthesis of the p-nuclei ^{92}Mo and ^{94}Mo was studied in different environments of the Supernova type Ia model. The nucleosynthesis flow proceeds via neutron-dissociation reactions starting on more neutron-rich molybdenum isotopes. At the neutron shell closure, ^{92}Mo is destroyed by proton-dissociation reactions. The maximum temperature and the duration of the high temperature phase determine the final abundances of ^{92}Mo and ^{94}Mo. The longer the high temperature phase lasts, the more Mo isotopes are disintegrated, and the mass fraction is shifted towards the proton-rich Mo isotopes. The higher the peak temperature, the more ^{92}Mo is destroyed by proton-dissociation reactions, preventing the backflow to heavier Mo isotopes via neutron-capture reactions.

Future studies foresee a detailed study of the complete stellar environment of a Supernova type Ia relevant for the production of the p-nuclei of molybdenum as well as the investigation of all p-nuclei. Furthermore, up-to-date three-dimensional Supernova type Ia models will soon become available for detailed post-processing nucleosynthesis studies.

5 Kurzfassung

Die Nukleosynthese der chemischen Elemente

Ziel der nuklearen Astrophysik ist es, die Synthese der Elemente von Wasserstoff bis zu den schwersten Kernen im Universum zu erklären. Spektroskopische Beobachtungen der Sonne, Analysen der Zusammensetzung von Meteoriten und die Bestimmung der Elementzusammensetzungen auf der Erde erlauben Rückschlüsse auf die solare Häufigkeitsverteilung der Elemente [1]. Strukturen in der Häufigkeitsverteilung weisen auf unterschiedliche Produktionsszenarien für verschiedene Massenbereiche hin [2].

Die leichtesten Elemente Wasserstoff, Helium und kleine Mengen Lithium und Beryllium wurden in der primordialen Nukleosynthese in den ersten drei Minuten nach dem Urknall erzeugt [4, 5]. Lithium, Beryllium und Bor werden auch später durch Spaltreaktionen schwerer Kerne durch kosmische Strahlung erzeugt [6].

Die Elemente bis zur Eisengruppe werden durch Fusionsreaktionen geladener Teilchen in verschiedenen stellaren Brennphasen produziert. Helium wird in der Proton-Proton-Kette und im CNO-Zyklus während des hydrostatischen Wasserstoffbrennens erzeugt [7–9]. Im folgenden Heliumbrennen wird Kohlenstoff durch den Drei-Alpha-Prozess fusioniert [10–12]. Die weiteren Brennphasen hängen von der Masse des Sterns ab. Die Elemente der Eisengruppe werden schließlich im Siliziumbrennen von Sternen mit mehr als acht Sonnenmassen erzeugt [13]. Die Bindungsenergie pro Nukleon ist dort am größten, sodass ein lokales Maximum in der solaren Häufigkeitsverteilung entsteht. Mit dem Erlöschen des Siliziumbrennens kollabiert der stellare Kern und der Stern explodiert als Supernova.

Die Elemente schwerer als Eisen werden hauptsächlich durch Neutroneneinfangprozesse im schnellen r-Prozess und im langsamen s-Prozess gebildet. Der r-Prozess findet in explosiven Szenarien mit hohen Neutronendichten von mehr als 10^{20} cm^{-3} und Temperaturen über 10^9 K statt. Durch viele Neutroneneinfänge werden sehr neutronenreiche, instabile Kerne erzeugt, die nach Abklingen des Neutronenflusses zum Stabilitätstal zerfallen [14–16]. Der s-Prozess findet während stellarer Helium- und Kohlenstoffbrennphasen mit Neutronendichten von 10^8 und 10^{10} cm^{-3} statt. Auf einer Zeitskala von etwa zehn Jahren fängt ein Kern ein Neutron ein. Wird so ein instabiler Kern mit einer kürzeren Halbwertszeit er-

reicht, zerfällt dieser. Der Pfad des s-Prozesses bewegt sich folglich entlang des Tals der Stabilität bis hin zu Blei [17].

Der p-Prozess

Etwa 35 protonenreiche Kerne zwischen Selen und Quecksilber, die sogenannten p-Kerne, können nicht durch Neutroneneinfangprozesse erzeugt werden [2]. Viele Produktionsszenarien werden diskutiert, die sich in drei wesentlichen Eigenschaften unterscheiden: in den Temperatur- und Dichteprofilen der stellaren Umgebung, in den Anfangshäufigkeiten aller Atomkerne und in den Raten der Kernreaktionen im Reaktionsnetzwerk [28].

Die Häufigkeiten der p-Kerne sind typischerweise zwei Größenordnungen kleiner als die der r- und s-Kerne des gleichen Elements. Die häufigsten p-Kerne ^{92,94}Mo und ^{96,98}Ru hingegen weisen deutlich höhere Isotopenhäufigkeiten von 14,9%, 9,2%, 5,5% und 1,9% auf. Nukleosynthesesimulationen können diese Häufigkeiten bisher nicht reproduzieren, sodass ihr Ursprung rätselhaft bleibt [28, 29].

Im γ-Prozess werden p-Kerne durch Photodissoziationsreaktionen an r- und s-Kernen erzeugt. Neutronen-, Protonen- und α-Dissoziationsreaktionen an neutronenreichen Isotopen führen direkt oder durch β-Zerfälle instabiler Kerne zu den p-Kernen. In explosiven Szenarien werden die für den γ-Prozess notwendigen Temperaturen von 2,0 bis 3,5·10^9 K erreicht. Im explosiven Brennen in der Ne/O-Schale während einer Supernovae Typ II könnten p-Kerne produziert werden [30–33]. Die Häufigkeiten der p-Kerne können aber nicht allein durch Supernovae Typ II erklärt werden. Als weitere astrophysikalische Umgebung wurden Supernovae Typ Ia vorgeschlagen, die mehr als 50% der p-Kerne produzieren könnten. Neben dem γ-Prozess in den äußeren Schichten könnten auch Protoneneinfangreaktionen die leichten p-Kerne ^{92,94}Mo und ^{96,98}Ru erzeugen [36, 37].

Zielsetzung der Arbeit

Ziel der vorliegenden Arbeit war es, zum Verständnis der Produktion der leichten p-Kerne ^{92}Mo und ^{94}Mo beizutragen. Nukleosynthesesimulationen haben gezeigt, dass ^{94}Mo hauptsächlich durch Neutronen-Dissoziationsreaktionen an schwereren Molybdänisotopen erzeugt wird. Um das Verhältnis der Häufigkeiten von ^{94}Mo zu ^{92}Mo zu erklären, ist die Kenntnis des Wirkungsquerschnitts der Reaktion ^{94}Mo(γ,n) notwendig. Die Reaktion wurde mit der Coulombaufbruchmethode am LAND Aufbau am GSI Helmholtzzentrum für Schwerionenforschung in Darmstadt, Deutschland, untersucht. Die Messung wurde im Rahmen der vorliegenden Arbeit ausgewertet.

Die Produktion der leichten p-Kerne wurde in Nukleosynthesesimulationen innerhalb des NuGrid Projekts untersucht. Für das Modell einer Supernova Typ II wurden die wichtigsten Produktions- und Destruktionsreaktionen der p-Kerne ^{92,94}Mo und ^{96,98}Ru bestimmt und der Einfluss von Ratenunsicherheiten auf die Endhäufigkeiten quantifiziert. Die Synthese der p-Kerne ^{92}Mo und ^{94}Mo wurde ebenfalls in einem Supernova Typ Ia Modell simuliert. Der Einfluss stellarer Parameter auf die Endhäufigkeiten der beiden Molybdänisotope wurde untersucht.

Messung der Reaktion ^{94}Mo(γ,n) mit der Coulombaufbruchmethode

Die Reaktion ^{94}Mo(γ,n) wurde in inverser Kinematik mit der Coulombaufbruchmethode untersucht. Im Rahmen des Experiments wurden auch die Dissoziationsreaktionen der Isotope ^{100}Mo, ^{93}Mo und ^{92}Mo gemessen. Die Ergebnisse wurden in der Doktorarbeit von O. Ershova veröffentlicht [48].

Ein Primärstrahl von ^{94}Mo-Kernen wurde mit einer Energie von 500 AMeV auf ein Bleitarget gelenkt. Die Strahlteilchen konnten im elektromagnetischen Feld des Bleikerns durch virtuelle Photonen angeregt werden, sodass sie ein Neutron emittierten. Zur Rekonstruktion der Neutronen-Dissoziationsreaktion ^{94}Mo(γ,n) wurden alle Ionen im Eingangs- und Ausgangskanal anhand ihrer Ladung und ihrer Kinematik identifiziert. Die geladenen Ionen im Ausgangskanal wurden durch den Magneten ALADIN abgelenkt. Die Teilchentrajektorien wurden vor und nach dem Magneten bestimmt, sodass die Massenzahl der ausgehenden Ionen bei bekannter Ladungszahl anhand der Ablenkung im Magnetfeld ermittelt werden konnte. Das dissoziierte Neutron wurde mit LAND (Large Area Neutron Detector) nachgewiesen. Anhand einer Reihe von Selektionskriterien wurden die Neutronen-Dissoziationsreaktionen aus den Daten extrahiert und der Coulombdissoziationswirkungsquerschnitt bestimmt. Die systematischen Unsicherheiten des Wirkungsquerschnitts ergaben sich aus der Variation der Selektionskriterien und der dominierenden Unsicherheit in der softwarebasierten Rekonstruktion des Neutrons durch LAND. Der integrale Coulombdissoziationswirkungsquerschnitt wurde bestimmt zu

$$\sigma_{CD} = (571 \pm 14_{stat} \pm 46_{syst}) \text{ mb.}$$

Mit der gleichen Analyse wurde die Reaktion ^{100}Mo(γ,n) untersucht. Es ergab sich ein integraler Coulombdissoziationswirkungsquerschnitt von $(815 \pm 37_{stat} \pm 67_{syst})$ mb. Das Ergebnis stimmt innerhalb der Unsicherheiten mit dem von O. Ershova ermittelten Wert von $(799 \pm 17_{stat} \pm 81_{syst})$ mb überein [48]. Somit konnten die Ergbnisse unabhängiger Analysen verifiziert werden.

Die Ergebnisse für die Isotope ^{100}Mo, ^{94}Mo und ^{92}Mo wurden mit Photoabsorptionsdaten verglichen, die von Beil et al. am Linearbeschleuniger in Saclay gewonnen wurden [49]. Frühere Vergleiche hatten eine Diskrepanz gezeigt, sodass Normierungsfaktoren von 0,8 bis 0,88 für die Photoabsorptionsdaten aus Saclay für Kerne im Massenbereich von $A = 85$-93 vorgeschlagen worden waren [84]. O. Ershova hatte die Normierungsfaktoren mit einem Wert von 0,8 in die Analyse des Isotops ^{100}Mo bestätigen können. Jedoch zeigte der Vergleich für die Isotope ^{92}Mo und ^{94}Mo kleinere Normierungsfaktoren von etwa 0,6. Mögliche Ursachen für die Abweichungen werden künftig untersucht.

Nukleosynthesesimulationen zur Produktion der p-Kerne

Der Einfluss der Produktions- und Destruktionsreaktionen auf die Häufigkeiten der leichten p-Kerne ^{92}Mo, ^{94}Mo, ^{96}Ru und ^{98}Ru wurde in Nukleosynthesesimulationen einer Supernova Typ II untersucht. Im Modell werden die p-Kerne im γ-Prozess erzeugt, wenn die Schockfront durch die Ne/O-Schicht des Sterns läuft. Die leichten p-Kerne werden dabei hauptsächlich durch Neutronen-Dissoziationsreaktionen an schwereren Kernen in der Isotopenkette produziert. Je höher die Temperatur in der stellaren Umgebung, desto größer ist der Anteil an Protonen- und α-Dissoziationsreaktionen an schwereren Elementen, welche die p-Kerne von Molybdän und Ruthenium erzeugen.

Der Einfluss von Ratenunsicherheiten auf die Endhäufigkeiten der leichten p-Kerne wurde bestimmt, indem einzelne Raten in der Simulation variiert wurden. Es zeigte sich, dass Variationen der Destruktionsraten die Endhäufigkeiten um bis zu 300% änderten. Die Variation der Produktionsraten hatte einen weit geringeren Einfluss. Folglich werden die Endhäufigkeiten der leichten p-Kerne durch die Unsicherheiten ihrer Destruktionsreaktionen dominiert.

Die Synthese der p-Kerne ^{92}Mo und ^{94}Mo wurde ebenfalls in einem Supernova Typ Ia Modell untersucht. Für beide Isotope wurden verschiedene Umgebungen ausgewählt, welche die gleiche Maximaltemperatur aufweisen, sich aber im Temperaturprofil unterscheiden. Es zeigte sich, dass die Häufigkeiten der beiden p-Kerne durch die Maximaltemperatur und die Dauer der Hochtemperaturphase bestimmt werden. Photoneninduzierte Reaktionen, insbesondere Neutronen-Dissoziationsreaktionen zerstören die schweren, neutronenreichen Molybdänisotope. Je höher die Maximaltemperatur ist, desto größer ist der Massenfluss zu den protonenreichen Isotopen.

Bei Temperaturen über 2,3 GK wird ^{94}Mo durch Neutronen-Dissoziationsreaktionen produziert. Je länger die Temperatur zwischen 2,3 und 2,7 GK liegt, desto mehr ^{94}Mo wird erzeugt. Steigt die Temperatur weiter an, wird ^{94}Mo wiederum durch Neutronen-Dissoziationsreaktionen zerstört, sodass das neutronenmagische Isotop ^{92}Mo produziert wird. Das

Isotop ^{92}Mo wird durch Protonen-Dissoziationsreaktionen zerstört, wenn die Temperatur 3,0 GK überschreitet. Hält die Phase extremer Temperaturen lange an, werden die schwereren Molybdänisotope effizient zerstört, sodass ^{92}Mo nicht mehr produziert werden kann. Je länger die Hochtemperaturphase andauert, desto kleiner ist die Endhäufigkeit von ^{92}Mo.

Ausblick

Coulombaufbruchreaktionen können zukünftig an der im Bau befindlichen Facility for Antiproton and Ion Research in Europe (FAIR) gemessen werden. Am dort ebenfalls bereits im Aufbau befindlichen R^{3}B Experiment werden Neutronen-Dissoziationsreaktionen durch den neuen Neutronendetektor NeuLAND mit hoher Auflösung und hoher Nachweiswahrscheinlichkeit detektiert werden können. Die Messungen von Coulombaufbruchreaktionen relativistischer Ionenstrahlen mit kurzen Halbwertszeiten werden mit Strahlenergien bis zu 1 AGeV möglich sein [102, 103].

Zukünftige Nukleosynthesesimulationen sehen die vollständige Analyse des Reaktionsnetzwerks vor. Einerseits sollen aktuelle kernphysikalische Wirkungsquerschnittsmessungen einbezogen werden. Andererseits sollen die globalen Einflüsse einzelner Reaktionen auf die Produktion der p-Kerne untersucht werden. Für die Simulationen werden aktuelle dreidimensionale Sternmodelle zur Verfügung stehen.

A   Appendix

A.1   Additional information for the Coulomb dissociation experiment of molybdenum

A.1.1   Tracking parameters and conditions on the data

The mass of the outgoing fragment of a Coulomb dissociation reaction is determined by tracking the fragment through the magnetic field of ALADIN. The tracking software *Tracker* requires several input parameters concerning the geometry of the experimental setup and the reaction under investigation. Conditions are set on the data to preselect events of the reaction under investigation. Table A.1 lists the detector and component positions during the molybdenum experiment in the laboratory system of Cave C.

The tracking parameters describing the reaction under investigation are given in Table A.2. The reaction triggers have to be chosen for minimum bias events and neutron trigger events separately (compare Table 2.2).

To describe the kinematics of the reaction correctly, the velocity β of the ion at the target is needed. From the beam energy the energy loss in the detector material in front of the target and in half the thickness of the target was calculated with the program ATIMA [104]. Table A.3 lists the detector and target properties needed for the calculation.

Detector / component	x (cm)	y (cm)	z (cm)
PSP1	-0.700	0.000	-224.600
PSP2	-0.230	0.000	-73.800
Target	0.000	0.000	0.000
PSP3	0.270	0.000	76.857
Aladin	0.000	0.000	225.400
GFI1	-80.849	0.000	574.736
GFI2	-273.310	2.910	1403.036
GFI3	-285.520	0.000	1452.217
TFW	-362.595	3.080	1636.090

Table A.1.: Detector positions during the molybdenum experiment in the laboratory system of Cave C. The target is located at (0,0,0). The beam travels in positive z-direction. The y-direction points upwards, and looking in z-direction x points left to create a right-handed coordinate system (compare Figure 2.4).

Parameter	Value / condition	
	^{94}Mo	^{100}Mo
Charge of incoming ion	42	42
A/Z of incoming ion	2.238	2.381
β of incoming ion at half Pb target	0.7539	0.7534
β of incoming ion at half C target	0.7551	0.7546
β of incoming ion at target position (no target)	0.7569	0.7562
Charge of outgoing fragment	42	42
Physics trigger	$0 < Tpat < 255$	
Reject pile-up events	$Tnext > 10000$	
	$5500 < Tprev < 5700$	
Fragment multiplicity	$Tfmul == 1$	
Reaction triggers	$Tpat\&1 \: != 0$ Minimum bias	
	or	
	$Tpat\&4 \: != 0$ Neutron trigger	
Neutron multiplicity (with neutron trigger)	$Ntmul == N_{\text{neutron}}$	
PSP3, GFI1, and GFI2/GFI3 detected signals		

Table A.2.: Tracking parameters and conditions on the data.

Detector / Material	Z	A (u)	thickness (mg/cm^2)
PSP1 (Si)	14	28.085	70.00
POS (C)	6	12.011	0.21
PSP2 (Si)	14	28.085	70.00
Half Pb target	82	207.200	259.50
Half C target	6	12.011	93.50

Table A.3.: Characteristics of the detectors in front of the target and of the Pb and C targets. The data are needed to calculate the energy loss of the ions in the detector material with ATIMA [104].

A.2   Additional information from PPN simulations

A.2.1   Abundance trends of Hashimoto trajectories in the simulation of the Supernova type II model

Post-processing nucleosynthesis (PPN) simulations were carried out for a Supernova type II model to identify the relevant reactions for the production and destruction of the Mo and Ru p-nuclei and to quantify the effect of rate changes on the final mass fractions. The Supernova type II model is the same as used by Rapp et al. [98]. The stellar progenitor had an initial mass of 25 $M_\odot$ and a metallicity of $Z = 0.02$ [92]. In the model, the shock front passes through the Ne/O burning zone, which is subdivided into 14 mass layers. The shock front reaches the mass layers successively. Temperature and density rapidly increase to the maximum values and afterwards drop slowly. The evolution of the temperatures and densities of all mass layers is described by the Hashimoto trajectories (compare Table 3.1).

Figures A.1 to A.12 show the mass fractions of several Mo, Ru and Pd isotopes as a function of time for the Hashimoto trajectories 2-3 and 5-14. The abundances change by up to ten orders of magnitude in the high temperature regime of the innermost layers (trajectories 2-5). If the peak temperatures are lower, more neutron-rich nuclei are produced or destroyed by up to several orders of magnitude, while the abundances of the proton-rich nuclei vary only slightly (trajectories 8-11). Hashimoto trajectories 12-14 do not affect the abundances of the nuclei selected for the analysis.
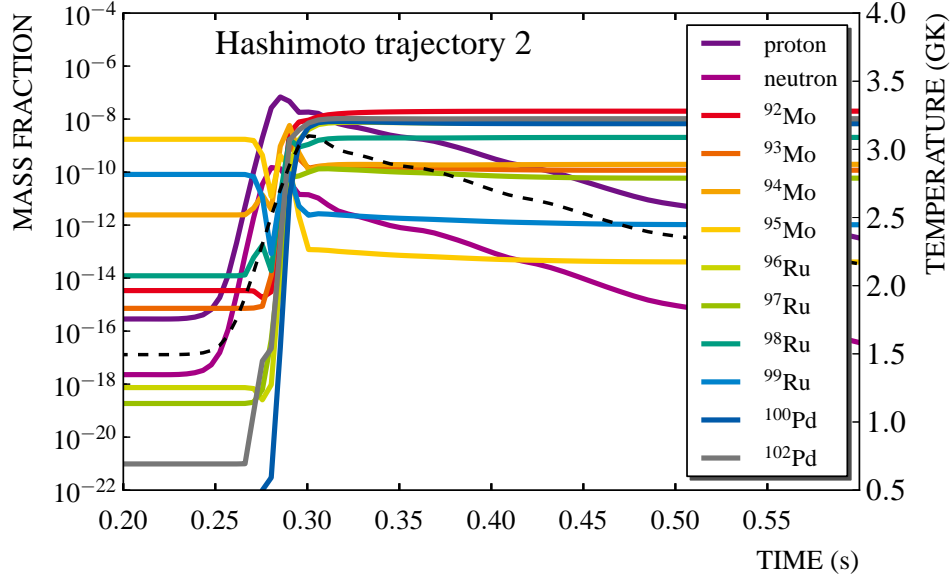
Figure A.1.: Mass fractions of Mo, Ru and Pd isotopes in the simulation of Hashimoto trajectory 2 of the Supernova type II model. The dashed black line shows the temperature profile.
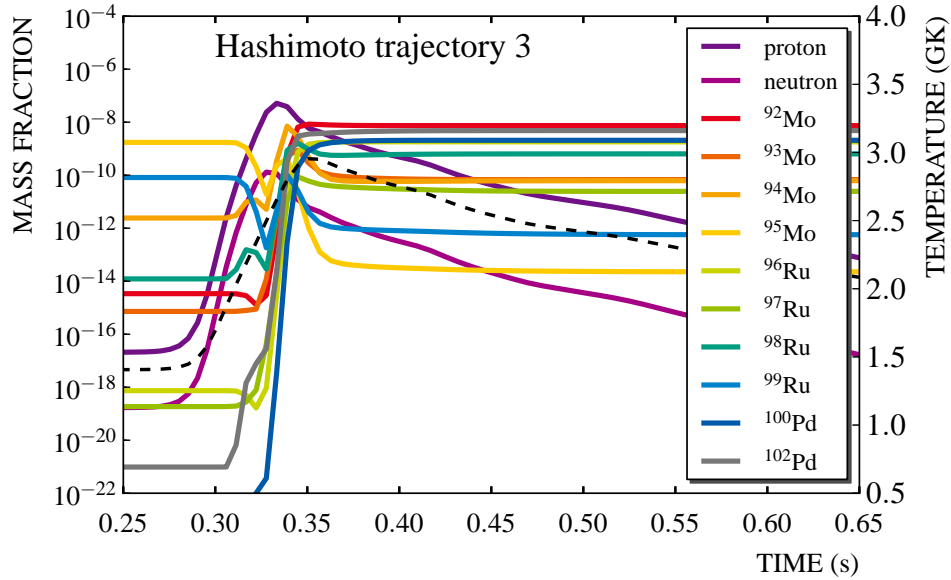
Figure A.2.: Same as Figure A.1, for Hashimoto trajectory 3.
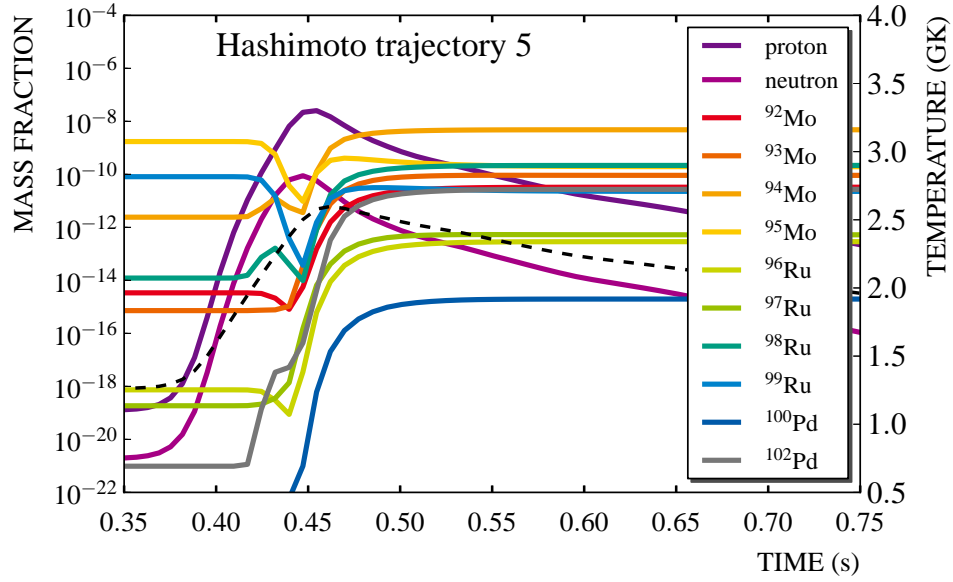
Figure A.3.: Same as Figure A.1, for Hashimoto trajectory 5.
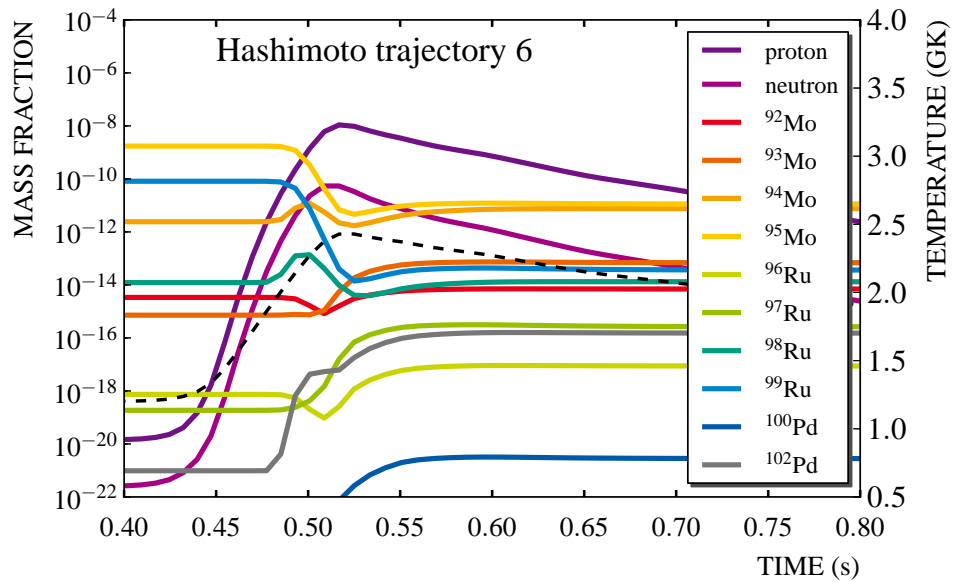
Figure A.4.: Same as Figure A.1, for Hashimoto trajectory 6.
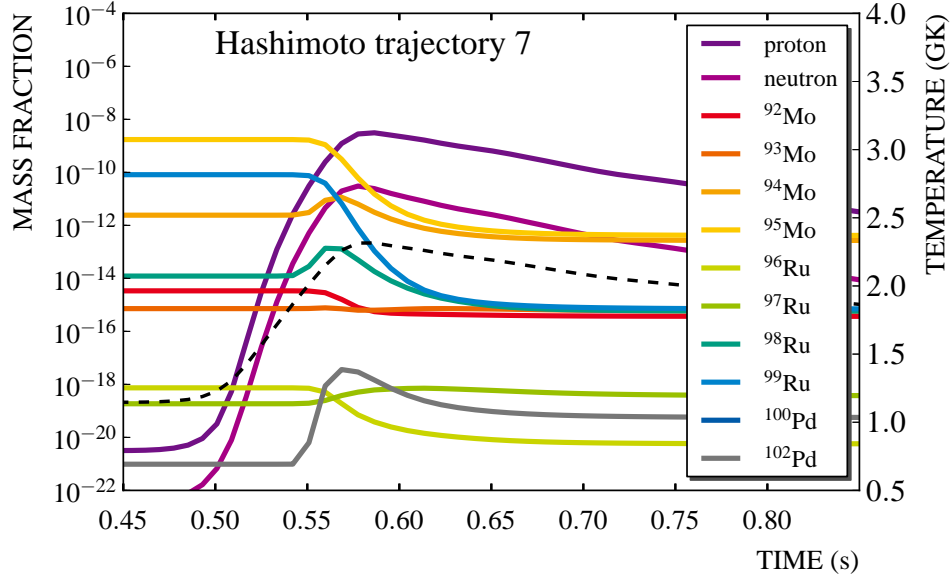
Figure A.5.: Same as Figure A.1, for Hashimoto trajectory 7.
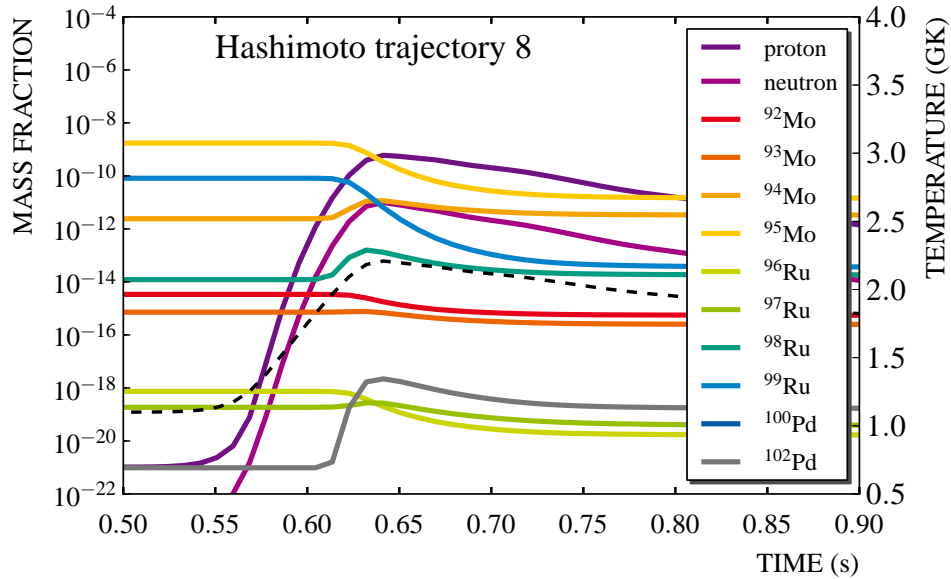
Figure A.6.: Same as Figure A.1, for Hashimoto trajectory 8.
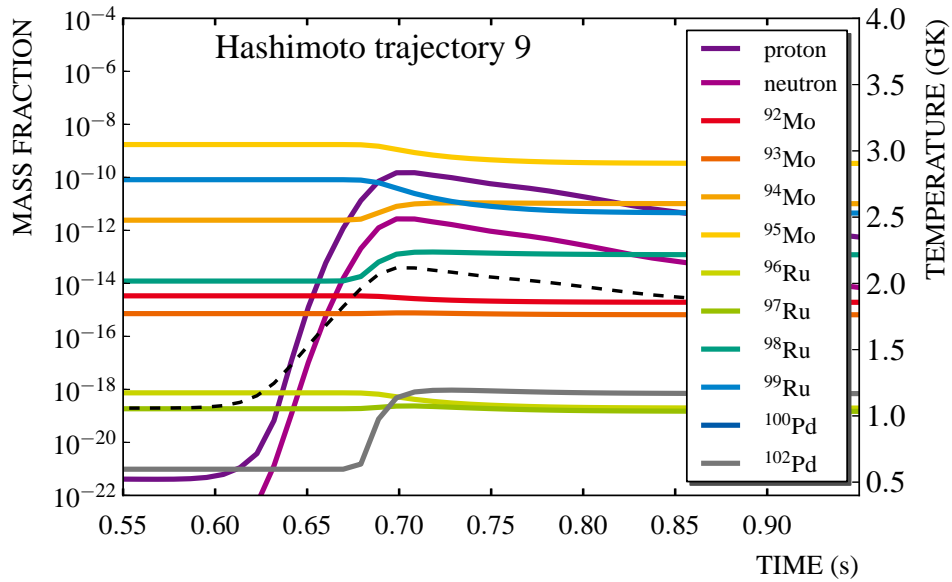
Figure A.7.: Same as Figure A.1, for Hashimoto trajectory 9.
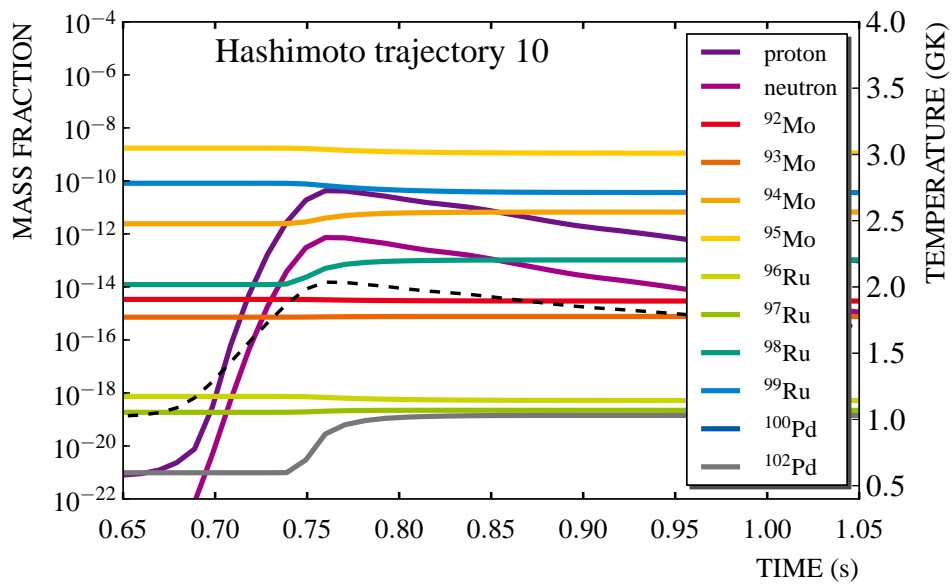
Figure A.8.: Same as Figure A.1, for Hashimoto trajectory 10.
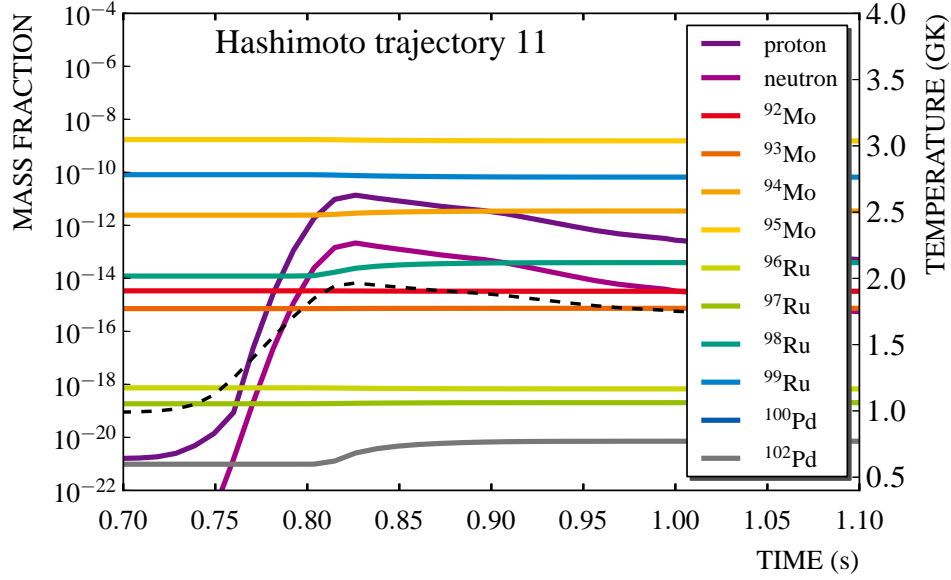
Figure A.9.: Same as Figure A.1, for Hashimoto trajectory 11.
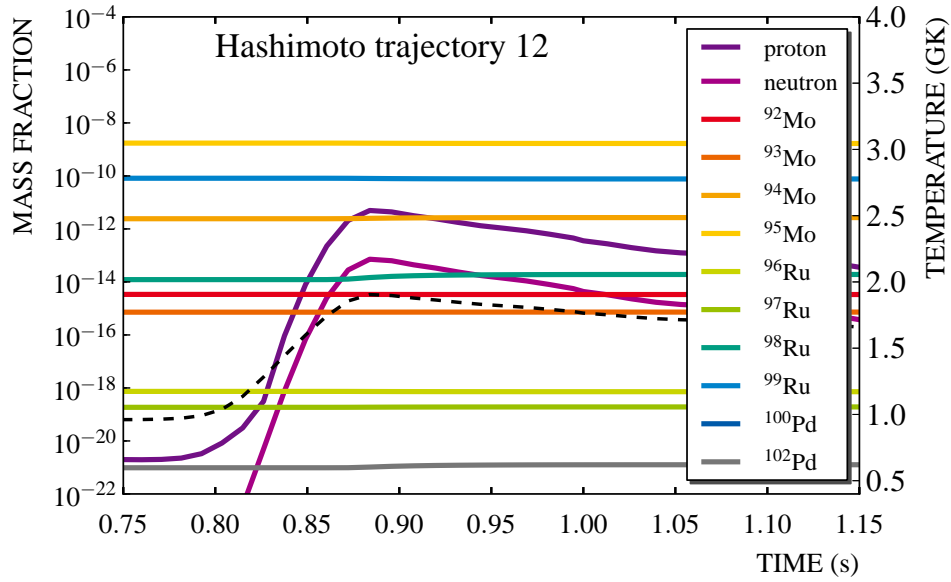
Figure A.10.: Same as Figure A.1, for Hashimoto trajectory 12.
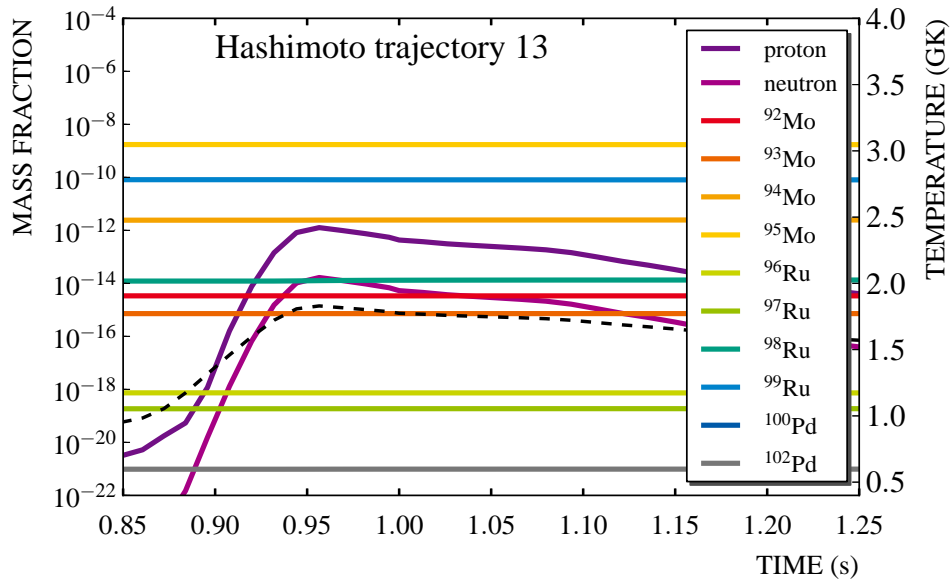
Figure A.11.: Same as Figure A.1, for Hashimoto trajectory 13.
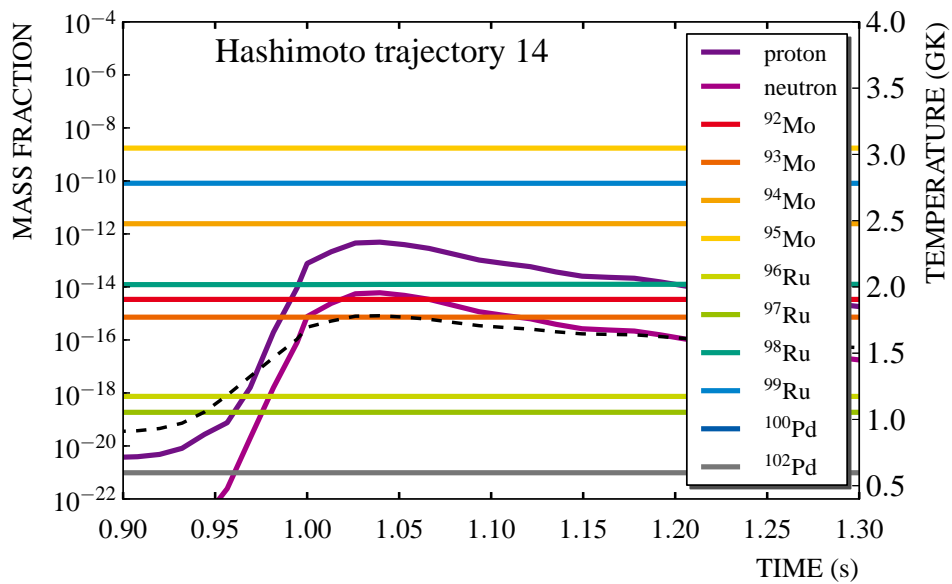
Figure A.12.: Same as Figure A.1, for Hashimoto trajectory 14.

Bibliography

[1] K. Lodders. Solar System Abundances and Condensation Temperatures of the Elements. *The Astrophysical Journal*, 591:1220–1247, July 2003.

[2] E. M. Burbidge, G. R. Burbidge, W. A. Fowler, and F. Hoyle. Synthesis of the Elements in Stars. *Reviews of Modern Physics*, 29:547–650, 1957.

[3] J. José and C. Iliadis. Nuclear astrophysics: the unfinished quest for the origin of the elements. *Reports on Progress in Physics*, 74(9):096901, September 2011.

[4] G. Gamow. Expanding Universe and the Origin of Elements. *Physical Review*, 70:572–573, October 1946.

[5] R. A. Alpher, H. Bethe, and G. Gamow. The Origin of Chemical Elements. *Physical Review*, 73:803–804, April 1948.

[6] E. Vangioni-Flam, M. Cassé, and J. Audouze. Lithium-beryllium-boron: origin and evolution. *Physics Reports*, 333:365–387, August 2000.

[7] R. D. E. Atkinson and F. G. Houtermans. Zur Frage der Aufbaumöglichkeit der Elemente in Sternen. *Zeitschrift für Physik*, 54:656–665, September 1929.

[8] H. A. Bethe and C. L. Critchfield. On the Formation of Deuterons by Proton Combination. *Physical Review*, 54:862–862, November 1938.

[9] H. A. Bethe. Energy Production in Stars. *Physical Review*, 55:434–456, March 1939.

[10] F. Hoyle. On Nuclear Reactions Occuring in Very Hot STARS.I. the Synthesis of Elements from Carbon to Nickel. *The Astrophysical Journal, Supplement*, 1:121, September 1954.

[11] D. N. Dunbar, R. E. Pixley, W. A. Wenzel, and W. Whaling. The 7.68-Mev State in C^{12}. *Physical Review*, 92:649–650, November 1953.

[12] C. W. Cook, W. A. Fowler, C. C. Lauritsen, and T. Lauritsen. B^{12}, C^{12}, and the Red Giants. *Physical Review*, 107:508–515, July 1957.

[13] F. E. Clifford and R. J. Tayler. The equilibrium distribution of nuclides in matter at high temperatures. *Memoirs of the Royal Astronomical Society*, 69:21, 1965.

[14] F.-K. Thielemann, A. Arcones, R. Käppeli, M. Liebendörfer, T. Rauscher, C. Winteler, C. Fröhlich, I. Dillmann, T. Fischer, G. Martinez-Pinedo, K. Langanke, K. Farouqi, K.-L. Kratz, I. Panov, and I. K. Korneev. What are the astrophysical sites for the r-process and the production of heavy elements? *Progress in Particle and Nuclear Physics*, 66:346–353, April 2011.

[15] Y.-Z. Qian. Astrophysical models of r-process nucleosynthesis: An update. In S. Kubono, T. Hayakawa, T. Kajino, H. Miyatake, T. Motobayashi, and K. Nomoto, editors, *American Institute of Physics Conference Series*, volume 1484 of *American Institute of Physics Conference Series*, pages 201–208, November 2012.

[16] A. Arcones and F.-K. Thielemann. Neutrino-driven wind simulations and nucleosynthesis of heavy elements. *Journal of Physics G: Nuclear and Particle Physics*, 40(1):013201, 2013.

[17] R. Reifarth, C. Lederer, and F. Käppeler. Neutron reactions in astrophysics. *Journal of Physics G Nuclear Physics*, 41(5):053101, May 2014.

[18] P. A. Seeger, W. A. Fowler, and D. D. Clayton. Nucleosynthesis of Heavy Elements by Neutron Capture. *The Astrophysical Journal, Supplement*, 11:121, February 1965.

[19] F. Herwig, B. Freytag, R. M. Hueckstaedt, and F. X. Timmes. Hydrodynamic Simulations of He Shell Flash Convection. *The Astrophysical Journal*, 642:1057–1074, May 2006.

[20] O. Straniero, A. Chieffi, M. Limongi, M. Busso, R. Gallino, and C. Arlandini. Evolution and Nucleosynthesis in Low-Mass Asymptotic Giant Branch Stars. I. Formation of Population I Carbon Stars. *The Astrophysical Journal*, 478:332–339, March 1997.

[21] C. Travaglio, R. Gallino, M. Busso, and R. Gratton. Lead: Asymptotic Giant Branch Production and Galactic Chemical Evolution. *The Astrophysical Journal*, 549:346–352, March 2001.

[22] R. G. Couch, A. B. Schmiedekamp, and W. D. Arnett. s-process Nucleosynthesis in Massive Stars: Core Helium Burning. *The Astrophysical Journal*, 190:95–100, May 1974.

[23] S. A. Lamb, W. M. Howard, J. W. Truran, and I. Iben, Jr. Neutron-capture nucleosynthesis in the helium-burning cores of massive stars. *The Astrophysical Journal*, 217:213–221, October 1977.

[24] W. D. Arnett and F.-K. Thielemann. Hydrostatic nucleosynthesis. I - Core helium and carbon burning. *The Astrophysical Journal*, 295:589–619, August 1985.

[25] M. Busso and R. Gallino. The production of neutron-rich isotopes during He burning in massive stars. *Astronomy & Astrophysics*, 151:205–214, October 1985.

[26] B. W. Carroll and D. A. Ostlie. *An Introduction to Modern Astrophysics*. Pearson International Edition, 2007.

[27] W. Hillebrandt, M. Kromer, F. K. Röpke, and A. J. Ruiter. Towards an understanding of Type Ia supernovae from a synthesis of theory and observations. *Frontiers of Physics*, 8:116–143, April 2013.

[28] T. Rauscher, N. Dauphas, I. Dillmann, C. Fröhlich, Z. Fülöp, and G. Gyürky. Constraining the astrophysical origin of the p-nuclei through nuclear physics and meteoritic data. *Reports on Progress in Physics*, 76(6):066201, June 2013.

[29] M. Arnould and S. Goriely. The p-process of stellar nucleosynthesis: astrophysics and nuclear physics status. *Physics Reports*, 384:1–84, September 2003.

[30] S. E. Woosley and W. M. Howard. The p-process in supernovae. *The Astrophysical Journal, Supplement*, 36:285–304, February 1978.

[31] M. Rayet, M. Arnould, and N. Prantzos. The p-process revisited. *Astronomy & Astrophysics*, 227:271–281, January 1990.

[32] D. L. Lambert. The p-nuclei - Abundances and origins. *The Astronomy and Astrophysics Review*, 3:201–256, April 1992.

[33] M. Rayet, M. Arnould, M. Hashimoto, N. Prantzos, and K. Nomoto. The p-process in Type II supernovae. *Astronomy & Astrophysics*, 298:517, June 1995.

[34] M. Pignatari, R. Hirschi, M. Wiescher, R. Gallino, M. Bennett, M. Beard, C. Fryer, F. Herwig, G. Rockefeller, and F. X. Timmes. The ^{12}C + ^{12}C Reaction and the Impact on Nucleosynthesis in Massive Stars. *The Astrophysical Journal*, 762:31, January 2013.

[35] W. M. Howard, B. S. Meyer, and S. E. Woosley. A new site for the astrophysical gamma-process. *The Astrophysical Journal, Letters*, 373:L5–L8, May 1991.

[36] M. Kusakabe, N. Iwamoto, and K. Nomoto. Production of the p-process Nuclei in the Carbon-deflagration Model for Type Ia Supernovae. *The Astrophysical Journal*, 726:25, January 2011.

[37] C. Travaglio, F. K. Röpke, R. Gallino, and W. Hillebrandt. Type Ia Supernovae as Sites of the p-process: Two-dimensional Models Coupled to Nucleosynthesis. *The Astrophysical Journal*, 739:93, October 2011.

[38] H. Schatz, A. Aprahamian, J. Goerres, M. Wiescher, T. Rauscher, J. F. Rembges, F.-K. Thielemann, B. Pfeiffer, P. Moeller, K.-L. Kratz, H. Herndl, B. A. Brown, and H. Rebel. rp-Process Nucleosynthesis at Extreme Temperature and Density Conditions. *Physics Reports*, 294:167–264, February 1998.

[39] C. Fröhlich, G. Martínez-Pinedo, M. Liebendörfer, F.-K. Thielemann, E. Bravo, W. R. Hix, K. Langanke, and N. T. Zinner. Neutrino-Induced Nucleosynthesis of $A > 64$ Nuclei: The νp Process. *Physical Review Letters*, 96(14):142502, April 2006.

[40] S. E. Woosley, D. H. Hartmann, R. D. Hoffman, and W. C. Haxton. The ν-process. *The Astrophysical Journal*, 356:272–301, June 1990.

[41] C. E. Rolfs and W. S. Rodney. *Cauldrons in the Cosmos*. The University of Chicago Press, 1998.

[42] T. Rauscher. The Path to Improved Reaction Rates for Astrophysics. *International Journal of Modern Physics E*, 20:1071–1169, 2011.

[43] G. Baur, C. A. Bertulani, and H. Rebel. Coulomb dissociation as a source of information on radiative capture processes of astrophysical interest. *Nuclear Physics A*, 458:188–204, September 1986.

[44] T. Rauscher and F.-K. Thielemann. Astrophysical reaction rates from statistical model calculations. *Atomic Data and Nuclear Data Tables*, 75(1–2):1 – 351, 2000.

[45] R. H. Cyburt, A. M. Amthor, R. Ferguson, Z. Meisel, K. Smith, S. Warren, A. Heger, R. D. Hoffman, T. Rauscher, A. Sakharuk, H. Schatz, F. K. Thielemann, and M. Wiescher. The JINA REACLIB Database: Its Recent Updates and Impact on Type-I X-ray Bursts. *The Astrophysical Journal, Supplement*, 189:240–252, July 2010.

[46] W. Hauser and H. Feshbach. The Inelastic Scattering of Neutrons. *Physical Review*, 87:366–373, July 1952.

[47] LBNL Isotopes Project Nuclear Data Dissemination Home Page. `http://ie.lbl.gov/toi.html`. Retrieved October 5th, 2014.

[48] O. Ershova. *Coulomb Dissociation Reactions on Molybdenum Isotopes for Astrophysics Applications*. PhD thesis, Goethe University Frankfurt, Germany, 2012.

[49] H. Beil, R. Bergère, P. Carlos, A. Leprêtre, A. D. Miniac, and A. Veyssière. A study of the photoneutron contribution to the giant dipole resonance in doubly even Mo isotopes. *Nuclear Physics A*, 227:427–449, 1974.

[50] K. Sonnabend, M. Babilon, J. Hasper, S. Müller, M. Zarza, and A. Zilges. Photo-dissociation of neutron deficient nuclei. *European Physical Journal A*, 27:149–152, March 2006.

[51] O. Ershova, P. Adrich, H. Alvarez-Pol, F. Aksouh, T. Aumann, M. Babilon, K. H. Behr, J. Benlliure, T. Berg, M. Boehmer, K. Boretzky, A. Bruenle, R. Beyer, E. Casarejos, M. Chartier, D. Cortina-Gil, A. Chatillon, U. Datta Pramanik, L. Deveaux, M. Elvers, T. Elze, H. Emling, M. Erhard, B. Fernandez-Dominguez, H. Geissel, M. Gorska, M. Heil, M. Hellstroem, G. Ickert, H. Johansson, A. Junghans, F. Käppeler, O. Kiselev, A. Klimkiewicz, J. V. Kratz, R. Kulessa, N. Kurz, M. Labiche, T. Le Bleis, R. Lemmon, K. Lindenberg, Y. Litvinov, P. Maierbeck, A. Movsesyan, S. Mueller, T. Nilsson, C. Nociforo, N. Paar, R. Palit, S. Paschalis, W. Prokopowicz, R. Reifarth, D. Rossi, L. Schnorrenberger, H. Simon, K. Sümmerer, G. Surowka, D. Vretenar, A. Wagner, S. Walter, W. Walus, H. Weick, N. Winckler, M. Winkler, and A. Zilges. Coulomb dissociation reactions on Mo isotopes for astrophysics applications. In *Proceedings of "Nuclei in the Cosmos" PoS(NIC XI)014*, 2010.

[52] The NuGrid collaboration. `http://www.nugridstars.org`.

[53] C. Travaglio, R. Gallino, T. Rauscher, N. Dauphas, F. K. Röpke, and W. Hillebrandt. Radiogenic p-isotopes from Type Ia Supernova, Nuclear Physics Uncertainties, and Galactic Chemical Evolution Compared with Values in Primitive Meteorites. *The Astrophysical Journal*, 795:141, November 2014.

[54] E. Fermi. Über die Theorie des Stoßes zwischen Atomen und elektrisch geladenen Teilchen. *Zeitschrift für Physik*, 29:315–327, December 1924.

[55] C. F. von Weizsäcker. Ausstrahlung bei Stößen sehr schneller Elektronen. *Zeitschrift für Physik*, 88:612–625, September 1934.

[56] E. J. Williams. Nature of the High Energy Particles of Penetrating Radiation and Status of Ionization and Radiation Formulae. *Physical Review*, 45:729–730, May 1934.

[57] C. A. Bertulani and G. Baur. Relativistic Coulomb collisions and the virtual radiation spectrum. *Nuclear Physics A*, 442:739–752, September 1985.

[58] C. A. Bertulani and G. Baur. Electromagnetic processes in relativistic heavy ion collisions. *Physics Reports*, 163:299–408, June 1988.

[59] C. J. Benesh, B. C. Cook, and J. P. Vary. Single nucleon removal in relativistic nuclear collisions. *Physical Review C*, 40:1198–1206, September 1989.

[60] GSI Accelerators. `https://www.gsi.de/gsiwork/beschleuniger.htm`.

[61] B. Franczak. SIS parameter list. `https://www.gsi.de/fileadmin/`
`PSchwab/Dokumentationen_Berichte/Beschleunigeranlage/SIS18/sis18_`
`parameterliste.pdf`, 1987.

[62] H. Geissel, P. Armbruster, K. H. Behr, A. Brünle, K. Burkard, M. Chen, H. Folger,
B. Franczak, H. Keller, O. Klepper, B. Langenbeck, F. Nickel, E. Pfeng, M. Pfützner,
E. Roeckl, K. Rykaczewski, I. Schall, D. Schardt, C. Scheidenberger, K.-H. Schmidt,
A. Schröter, T. Schwab, K. Sümmerer, M. Weber, G. Münzenberg, T. Brohm,
H. G. Clerc, M. Fauerbach, J.-J. Gaimard, A. Grewe, E. Hanelt, B. Knödler,
M. Steiner, B. Voss, J. Weckenmann, C. Ziegler, A. Magel, H. Wollnik, J. P. Dufour,
Y. Fujita, D. J. Vieira, and B. Sherrill. The GSI projectile fragment separator (FRS):
a versatile magnetic system for relativistic heavy ions. *Nuclear Instruments and
Methods in Physics Research B*, 70:286–297, August 1992.

[63] G. Stengel. *Entwicklung großflächiger Szintillatorfaserdetektoren und aktiver
Blendensysteme*. Diploma thesis, Goethe University Frankfurt, Germany, 1996.

[64] I. Kraus. *Entwicklung eines CsI-Gammadetektors für Experimente mit radioaktiven
Strahlen*. Diploma thesis, Goethe University Frankfurt, Germany, 1999.

[65] T. Lange. *Erprobung und Eichung eines CsI(Na)-Gamma-Detektor-Systems für
Experimente mit radioaktiven Strahlen*. Diploma thesis, Goethe University Frankfurt,
Germany, 2001.

[66] A. Movsesyan. *Quasi-free one-proton and one-neutron knockout reactions on ^{57}Ni*.
PhD thesis, Technical University Darmstadt, Germany, 2013.

[67] H. T. Johansson. *The DAQ always runs. Performing large scale nuclear physics
experiments*. Licentiate thesis, Chalmers University of Technology, Gothenburg, Swe-
den, 2006.

[68] D. M. Rossi. *Investigation of the Dipole Response of Nickel Isotopes in the Presence of
a High-Frequency Electromagnetic Field*. PhD thesis, Johannes Gutenberg University
Mainz, Germany, 2009.

[69] C. Langer. *Coulomb Dissociation of ^{31}Cl and ^{32}Ar - constraining the rp process*. PhD
thesis, Goethe University Frankfurt, Germany, 2012.

[70] T. Blaich, T. W. Elze, H. Emling, H. Freiesleben, K. Grimm, W. Henning,
R. Holzmann, G. Ickert, J. G. Keller, H. Klingler, W. Kneissl, R. König, R. Kulessa,
J. V. Kratz, D. Lambrecht, J. S. Lange, Y. Leifels, E. Lubkiewicz, M. Proft,
W. Prokopowicz, C. Schütter, R. Schmidt, H. Spies, K. Stelzer, J. Stroth, W. Walus,

E. Wajda, H. J. Wollersheim, M. Zinser, and E. Zude. A large area detector for high-energy neutrons. *Nuclear Instruments and Methods in Physics Research A*, 314:136–154, April 1992.

[71] J. Cub, G. Stengel, A. Grünschloß, K. Boretzky, T. Aumann, W. Dostal, B. Eberlein, T. W. Elze, H. Emling, G. Ickert, J. Holeczek, R. Holzmann, J. V. Kratz, R. Kulessa, Y. Leifels, H. Simon, K. Stelzer, J. Stroth, A. Surowiec, and E. Wajda. A large-area scintillating fibre detector for relativistic heavy ions. *Nuclear Instruments and Methods in Physics Research A*, 402:67–74, February 1998.

[72] K. Mahata, H. T. Johansson, S. Paschalis, H. Simon, and T. Aumann. Position reconstruction in large-area scintillating fibre detectors. *Nuclear Instruments and Methods in Physics Research A*, 608:331–335, September 2009.

[73] *land02* software package. `http://web-docs.gsi.de/~rplag/land02/`.

[74] S. Paschalis. *Relativistic One-Nucleon Removal Reactions*. PhD thesis, University of Liverpool, England, 2008.

[75] C. A. Bertulani and A. Gade. Nuclear astrophysics with radioactive beams. *Physics Reports*, 485:195–259, January 2010.

[76] T. Aumann, J. V. Kratz, E. Stiel, K. Sümmerer, W. Brüchle, M. Schädel, G. Wirth, M. Fauerbach, and J. C. Hill. Inclusive measurements of electromagnetic dissociation of ^{197}Au targets. *Physical Review C*, 47:1728–1737, April 1993.

[77] H. Beil, R. Bergère, and A. Veyssière. Système de detection de photoneutrons utilisant un scintillateur à grandes dimensions permettant létude simultanée des reactions (γ,xn). *Nuclear Instruments and Methods*, 67:293–304, 1969.

[78] M. N. Harakeh and A. van der Woude. *Giant Resonances*. Clarendon Press, Oxford, 2001.

[79] S. S. Dietrich and B. L. Berman. Atlas of Photoneutron Cross Sections Obtained with Monoenergetic Photons. *Atomic Data and Nuclear Data Tables*, 38:199, 1988.

[80] N. Auerbach and A. Yeverechyahu. Nuclear viscosity and widths of giant resonances. *Annals of Physics*, 95:35–52, November 1975.

[81] B. L. Berman and S. C. Fultz. Measurements of the giant dipole resonance with monoenergetic photons. *Reviews of Modern Physics*, 47:713–761, 1975.

[82] A. Bohr and B. R. Mottelson. *Nuclear Structure, Volume II: Nuclear Deformations*. W. A. Benjamin Inc., 1975.

[83] A. Moalem, Y. Gaillard, A. M. Bemolle, M. Buenerd, J. Chauvin, G. Duhamel, D. Lebrun, P. Martin, G. Perrin, and P. de Saintignon. Isotopic dependence of the giant quadrupole resonance in the stable even-mass molybdenum nuclei. *Physical Review C*, 20:1593–1596, October 1979.

[84] B. L. Berman, R. E. Pywell, S. S. Dietrich, M. N. Thompson, K. G. McNeill, and J. W. Jury. Absolute photoneutron cross sections for Zr, I, Pr, Au, and Pb. *Physical Review C*, 36:1286–1292, October 1987.

[85] M. Erhard, A. R. Junghans, C. Nair, R. Schwengner, R. Beyer, J. Klug, K. Kosev, A. Wagner, and E. Grosse. Experimental study of the electric dipole strength in the even Mo nuclei and its deformation dependence. *Physical Review C*, 81(3), 2010.

[86] Claudia Travaglio. Private communication, 2014.

[87] F. Herwig, S. Diehl, C. L. Fryer, R. Hirschi, A. Hungerford, G. Magkotsios, M. Pignatari, G. Rockefeller, F. X. Timmes, P. Young, and M. E. Bennet. Nucleosynthesis simulations for a wide range of nuclear production sites from NuGrid. In *Proceedings of "Nuclei in the Cosmos" PoS(NIC X)023*, 2008.

[88] Marco Pignatari and Falk Herwig. The nugrid research platform: A comprehensive simulation approach for nuclear astrophysics. *Nuclear Physics News*, 22(4):18–23, 2012.

[89] T. Rauscher and F.-K. Thielemann. Basel reaction library. `http://download.nucastro.org/astro/reaclib`, January 2009.

[90] JINA REACLIB Database. `https://groups.nscl.msu.edu/jina/reaclib/db/index.php`.

[91] U. Frischknecht. *s-process nucleosynthesis in massive stars*. Master's thesis, University of Basel, Switzerland, 2007.

[92] M. Pignatari, F. Herwig, R. Hirschi, M. Bennett, G. Rockefeller, C. Fryer, F. X. Timmes, A. Heger, S. Jones, U. Battino, C. Ritter, A. Dotter, R. Trappitsch, S. Diehl, U. Frischknecht, A. Hungerford, G. Magkotsios, C. Travaglio, and P. Young. NuGrid stellar data set. I. Stellar yields from H to Bi for stars with metallicities $Z = 0.02$ and $Z = 0.01$. *ArXiv e-prints*, July 2013.

[93] Alexander Koloczek. Private communication, 2014.

[94] R. Schach. *Sensitivitätsstudien zur Produktion der p-Kerne ^{92,94}Mo und ^{96,98}Ru*. Bachelor's thesis, Goethe University Frankfurt, Germany, 2013.

[95] P. A. Denissenkov, J. W. Truran, M. Pignatari, R. Trappitsch, C. Ritter, F. Herwig, U. Battino, K. Setoodehnia, and B. Paxton. MESA and NuGrid simulations of classical novae: CO and ONe nova nucleosynthesis. *Monthly Notices of the Royal Astronomical Society*, 442:2058–2074, August 2014.

[96] ROOT Data Analysis Framework. `http://root.cern.ch`.

[97] GLE (Graphics Layout Engine). `http://glx.sourceforge.net`.

[98] W. Rapp, J. Görres, M. Wiescher, H. Schatz, and F. Käppeler. Sensitivity of p-Process Nucleosynthesis to Nuclear Reaction Rates in a 25 M_{solar} Supernova Model. *The Astrophysical Journal*, 653:474–489, December 2006.

[99] T. Rauscher. Branchings in the γ process path revisited. *Physical Review C*, 73(1):015804, January 2006.

[100] D. Kasen, F. K. Röpke, and S. E. Woosley. The diversity of type Ia supernovae from broken symmetries. *Nature*, 460:869–872, August 2009.

[101] C. Travaglio, W. Hillebrandt, M. Reinecke, and F.-K. Thielemann. Nucleosynthesis in multi-dimensional SN Ia explosions. *Astronomy & Astrophysics*, 425:1029–1040, October 2004.

[102] The R^3B collaboration. Technical Report for the Design, Construction and Commissioning of NeuLAND: The High-Resolution Neutron Time-of-Flight Spectrometer for R^3B. `http://www.fair-center.de/fileadmin/fair/experiments/NUSTAR/Pdf/TDRs/NeuLAND-TDR-Web.pdf`, 2011.

[103] The R^3B collaboration. Technical Proposal for the Design, Construction, Commissioning and Operation of R^3B - A universal setup for kinematical complete measurements of Reactions with Relativistic Radioactive Beams. `http://www-win.gsi.de/r3b/Documents/R3B-TP-Dec05.pdf`, 2005.

[104] H. Geissel, C. Scheidenberger, P. Malzacher, J. Kunzendorf, and H. Weick. ATIMA - ATomic Interaction with MAtter. `http://web-docs.gsi.de/~weick/atima/atima.html`.

130

List of Figures

List of Tables

136

DANKSAGUNG

Curriculum Vitae

Personal information

Name   Kathrin Göbel

Date of birth   February 11th, 1985

Place of birth   Hanau, Germany

Citizenship   German

Education

Since 2011   PhD student in experimental nuclear astrophysics, Goethe University, Frankfurt

2008 - 2011   Master student in Physics, Goethe University, Frankfurt
                  Minor: Physics Didactics.
                  Master thesis: "Vorbereitung der HADES-Driftkammern auf hohe Spurmultiplizitäten mittels Optimierung des Signal-zu-Untergrund-Verhältnisses" at the GSI Helmholtzzentrum für Schwerionenforschung.
                  Academic degree: Master of Science (1.0).

2005 - 2008   Bachelor student in Physics, Goethe University, Frankfurt
                  Minor: Astronomy.
                  Bachelor thesis: "Messungen zur Überprüfung der Nachweiswahrscheinlichkeit der HADES-Driftkammern" at the GSI Helmholtzzentrum für Schwerionenforschung.
                  Academic degree: Bachelor of Science (1.3).

2004 - 2005   Studies Mechanical Engineering, Frankfurt University of Applied Sciences.

2004   General qualification for university entrance, Kopernikusschule Freigericht.
                  Abitur (1.6).